Microstructural characterisation of GaMnN ferromagnetic semiconductors grown on (001) oriented GaAs substrates by plasma assisted molecular beam epitaxy

Yisong Han, MSc

Thesis submitted to the University of Nottingham
for the degree of Doctor of Philosophy

October 2006

To my mother and my wife……

Abstract

GaMnN layers grown by plasma assisted molecular beam epitaxy (PAMBE) as a function of Ga/N ratio, Mn flux and growth temperature are assessed using a variety of structural characterisation techniques. At 680°C, the Ga/N ratio is found to have a dominant impact on the zinc-blende GaMnN epilayer growth rate and the resultant composition, morphology and microstructure. A maximum growth rate and an optimised microstructure are associated with growth under slightly Ga-rich conditions. A reduced growth rate and enhanced Mn incorporation are associated with growth under slightly N-rich conditions. Increasing Mn flux under N-rich conditions is considered to lead to a build up of a Mn surfactant layer during the early stages of growth and to a transition from zinc-blende single phase growth to zinc-blende/wurtzite mixed phase growth. Further, under Ga-rich conditions at low temperature, GaMnN films adopt a tilted growth mode, with close packed planes for both hexagonal and cubic phases being tilted roughly parallel to the growth surface, and this way of modified growth is also accompanied by improved Mn incorporation which is not commonly found for samples grown under Ga-rich conditions at elevated temperature. In addition, α-MnAs inclusions and voids extending into the GaAs buffer layer were identified in all samples, but are considered not to have a detrimental effect on layer electrical and magnetic properties.

Publications

[1] M.W. Fay, Y. Han, P.D. Brown, K.W. Edmonds, K. Wang, B.L. Gallagher, R.P. Campion, C.T. Foxon, *Characterisation of GaMnAs/(001)GaAs epilayers grown by low temperature molecular beam epitaxy*, Phil. Mag. Lett., **86** (2006) 395-401.

[2] Y. Han, M.W. Fay, P.D. Brown, S.V. Novikov, K.W. Edmonds, B.L. Gallagher, R.P. Campion, C.R. Staddon, C.T. Foxon, *Structural characterisation of zinc-blende $Ga_{1-x}Mn_xN$ epilayers grown by MBE as a function of Ga flux*, J. Cryst. Growth, **284** (2005) 324-34.

[3] M.W. Fay, Y. Han, P.D. Brown, S.V. Novikov, K.W. Edmonds, R.P. Campion, B.L. Gallagher, C.T. Foxon, *Structural characterization of zincblende $Ga_{1-x}Mn_xN$ epilayers grown by molecular beam epitaxy on (001) GaAs substrates*, Appl. Phys. Lett., **87** (2005) 031902.

[4] S.V. Novikov, K.W. Edmonds, L.X. Zhao, A.D. Giddings, K.Y. Wang, R.P. Campion, C.R. Staddon, M.W. Fay, Y. Han, P.D. Brown, M. Savicki, B.L. Gallagher, C.T. Foxon, *Mn doping and p-type conductivity in zinc-blende GaMnN layers grown by molecular beam epitaxy*, J. Vac. Sci. Technol. B, **23** (2005) 1294-8.

[5] C.T. Foxon, S.V. Novikov, L.X. Zhao, K.W. Edmonds, A.D. Giddings, K.Y. Wang, R.P. Campion, C.R. Staddon, M.W. Fay, Y. Han, P.D. Brown, M. Sawicki, B.L. Gallagher, *Molecular beam epitaxy of p-type cubic GaMnN layers*, J. Cryst. Growth, **278** (2005) 685-9.

[6] Y. Han, M.W. Fay, S.V. Novikov, K.W. Edmonds, B.L. Gallagher, R.P. Campion, C.R. Staddon, C.T. Foxon, P.D. Brown, *Microstructural characterisation of zinc-blende $Ga_{1-x}Mn_xN$ grown by MBE as a function of Mn flux*, EMAG-NANO, Leeds (2005), J. of Phys.: Conf. Ser., **26** 179-82.

[7] M.W. Fay, Y. Han, K.W. Edmonds, K. Wang, R.P. Campion, B.L. Gallagher, C.T. Foxon, K.P. Hilton, A. Masterton, D. Wallis, R.S. Balmer, M.J. Uren, T. Martin, P.D. Brown, *Nanoscale characterisation of electronic and spintronic nitrides and arsenides*, EMAG-NANO, Leeds (2005), J. Phys.: Conf. Ser., **26** 175-8.

[8] Y. Han, M.W. Fay, P.D. Brown, S.V. Novikov, K.W. Edmonds, B.L. Gallagher, R.P. Campion, C.T. Foxon, *Structural characterisation of MBE grown zinc-blende $Ga_{1-x}Mn_xN$/GaAs(001) as a function of Ga flux*, Microscopy of Semiconducting Materials IX, Oxford (2005), Springer Proceedings in Physics, **107** 155-8.

[9] M.W. Fay, Y. Han, S.V. Novikov, K.W. Edmonds, K. Wang, B.L. Gallagher, R.P. Campion, C.T. Foxon, P.D. Brown, *Structural characterisation of spintronic GaMnAs and GaMnN heterostructures grown by molecular beam epitaxy*, Microscopy of Semiconducting Materials IX, Oxford (2005), **107** 143-6.

[10] M.W. Fay, Y. Han, P.D. Brown, I. Harrison, K.P. Hilton, A. Munday, D. Wallis, R.S. Balmer, M.J. Uren, T. Martin, *Structural and electrical characterization of AuPtAlTi ohmic contacts to AlGaN/GaN with varying annealing temperature and Al content*, to be Semiconductor Science and Technology, (2006).

[11] Y. Han, M.W. Fay, P.D. Brown, S.V. Novikov, K.W. Edmonds, B.L. Gallagher, R.P. Campion, C.R. Staddon, C.T. Foxon, *Microstructural characterisation of GaMnN grown on GaAs(001) by plasma-assisted MBE as a function of growth temperature*, drafted and to be submitted to Journal of Crystal Growth, (2006).

Acknowledgements

I would like to express my gratitude to Dr Paul D Brown for his continued support, patience and invaluable guidance to my research, education and personal development. I would like to thank Professor Bryan Gallagher and Professor C Thomas Foxon for their guidance and support of my research.

I would like to thank Dr Mike Fay for his assistance throughout, and for training in the technologies of transmission electron microscopy. I would also like to thank Dr Sergei Novikov and Dr Kevin Edmonds for their valuable discussions.

I would like to thank the EPSRC and the IDTC (Interdisciplinary Doctoral Training Centre) at Nottingham for the research grant and the provision of a studentship.

I would like to thank Keith Dinsdale, Martin Roe, Nicola Weston, Julie Thornhill and Nigel Neate for their kind technical support.

I also would like to thank Professor Tony Cullis for providing access to the TEM facilities at University of Sheffield.

Table of contents

CHAPTER ONE

Introduction

The mass, charge and spin of electrons in the solid state lay the foundations for information technology in the modern age. Based on the charge transport of electrons within semiconductors, great success has been achieved in integrated circuits and high-frequency devices, being used for data processing and transformation. Mass information storage, being indispensable for information technology, may now be realised using the spin of electrons within ferromagnetic materials. Recently, a new technology, termed spintronics, i.e. spin transport electronics or spin based electronics, has emerged, exploiting both the charged carriers and the electron spin in semiconductor devices, with the advantages of non-volatility, increased data processing speed, decreased electric power consumption and increased integration densities as compared with conventional semiconductor devices.

For the purpose of practical applications of spintronic devices, many challenges regarding spin injection, transport, manipulation and detection need to be addressed and studied, amongst which finding suitable ferromagnetic semiconductors has become a major issue. In fact, there are two basic criteria for a ferromagnetic semiconductor to be suitable for a practical spintronic device [1,2]. Firstly, the material should exhibit ferromagnetism up to temperatures of at least 500 K for a wide range of applications without temperature restriction, i.e. the magnetic

transformation temperature (Curie temperature, T_C) of this material should be over 500 K. Secondly, there should be an existing technology base that facilitates the development of a wide range of device configurations. To date, a number of candidate materials have been investigated, e.g. Cr spinels, rocksalt Eu and Mn-based chalcogenides, Mn-doped II-VI semiconductors, Mn-doped III-V semiconductors, ferromagnetic oxides and Heusler alloys, all exhibiting interesting magnetic, electric and/or optical properties. However, the growth and functional properties of these materials are far from being understood.

A semiconductor may be made magnetic by introducing transition metal elements into its matrix. Such material is termed a dilute magnetic semiconductor (DMS). In particular, a theoretical prediction of the Curie temperature for various semiconductors [3] suggests, for example, that a T_C value above room temperature is possible for zinc-blende GaMnN containing 5 at% Mn and a hole concentration of 3.5×10^{20} cm^{-3}. This triggered widespread research into the development of p-type GaMnN ferromagnetic semiconductors. In practice, establishing p-type conductivity is found comparatively easier within zinc-blende GaMnN than wurtzite GaMnN, where the transition metal species needs to be responsible for both the ferromagnetic properties and the p-type behaviour. By way of example, high p-type zinc-blende GaMnN layers with carrier concentrations exceeding 10^{18} cm^{-3} and a detected ferromagnetic signal over 400 K have been obtained by plasma-assisted molecular beam epitaxy (PAMBE) [4,5]. Room temperature ferromagnetism and p-type conductivity have also been reported for PAMBE grown zinc-blende GaN following Mn^+ ion implantation and annealing [6].

In order to incorporate Mn at suitable levels within zinc-blende GaN, in view of its limited solid solubility, it becomes necessary to use non-equilibrium growth techniques such as PAMBE. However, in addition to the thermodynamic preference for the formation of wurtzite GaN over zinc-blende GaN, which may result in phase separation reactions, the incorporation of Mn can lead to the formation of Mn-rich second phase clusters or/and precipitates (depending on growth conditions and the Mn concentration), which are considered to have a dominant effect on the material functional properties. Therefore, to underpin the interrelationship between the materials growth (and device processing) and the material functional properties, there is a need for characterisation of the MBE grown GaMnN layers, using appropriate techniques, for the purpose of imaging, and structural and chemical analysis.

In this work, GaMnN samples grown on GaAs(001) substrates using PAMBE, as a function of Ga/N ratio, Mn flux and growth temperature, are characterised using a variety of analytical techniques, including X-ray diffraction (XRD), scanning electron microscopy (SEM), transmission electron microscopy (TEM), reflection high-energy electron diffraction (RHEED), selected area electron diffraction (SAED), convergent beam electron diffraction (CBED), energy dispersive X-ray (EDX) analysis, electron energy loss spectrometry (EELS) and energy filtered TEM (EFTEM). Recent developments of ferromagnetic semiconductors, especially on the growth and characterisation of GaMnN, are covered in Chapter Two. Chapter Three describes the details of the growth of the GaMnN/GaAs(001) using PAMBE, procedures of cross-sectional TEM sample preparation and basic principles of the characterisation techniques employed during this work. The characterisation results of GaMnN as a function of Ga/N ratio, Mn flux and growth temperature are presented in Chapters

Four, Five and Six, respectively. In Chapter Seven, the effect of the incorporation of Mn on the development of the GaMnN microstructure and the interrelationship between the processing, structure and functional properties of these GaMnN/GaAs(001) thin films are then discussed. Prospects for the future development of this research activity are presented in Chapter Eight.

CHAPTER TWO

Literature Review

2.1 Introduction

In order to use both the charge and spin of electrons in semiconductors, a high concentration of magnetic elements may be introduced into nonmagnetic semiconductors to make them ferromagnetic. Mn-doped GaN was predicated to be able to exhibit Curie temperatures over room temperature if appropriate doping conditions are achieved [3], which triggered the widespread investigation on this material system, leading to reports of a wide range of Curie temperatures. Even though the low solid solubility of Mn within GaN may be overcome using the non-equilibrium growth technique, i.e. molecular beam epitaxy, a variety of phase separation reactions have been reported. In this chapter, much attention is particularly given the preparation and characterisation of GaMnN with basic issues of GaN, e.g. growth, microstructure and fundamental properties, also introduced initially in section 2.3.

2.2 Introduction to ferromagnetic semiconductors

The Si integrated circuit (IC) industry and the data storage industry have developed very quickly over the last half-century. High-speed signal processing and data storage in ICs are implemented by controlling the flow of carriers, e.g. electrons and holes, using applied electric fields. However, the stored information within ICs cannot be

maintained when the power is switched off. In comparison, a key advantage of magnetic memory technologies is that they are non-volatile because the mass storage of information is achieved using the electron spin within magnetic materials. Recently, a technology, termed spintronics (i.e. spin transport electronics or spin based electronics), exploiting the spin of charged carriers within semiconductors, has emerged [7,8]. This technology, aiming to control the injection, transfer and detection of carrier spin above room temperature, offers new functionalities in electronic and photonic devices with the advantages of non-volatility, increased data processing speed, decreased electric power consumption and increased integration densities as compared with conventional semiconductor devices [7]. By way of example, semiconductor lasers fed by spin-polarised current offer better mode stability and lower critical currents [9]. Similarly, a spin transistor is expected to be faster and more efficient than a standard field-effect transistor [9]. In addition, there are many other applications, such as spin light-emitting diodes (spin-LEDs), spin resonant tunneling device (spin-RTD), optical switches operating at terahertz frequencies, modulators, encoders, decoders and quantum dots for quantum computation and communication [7,8].

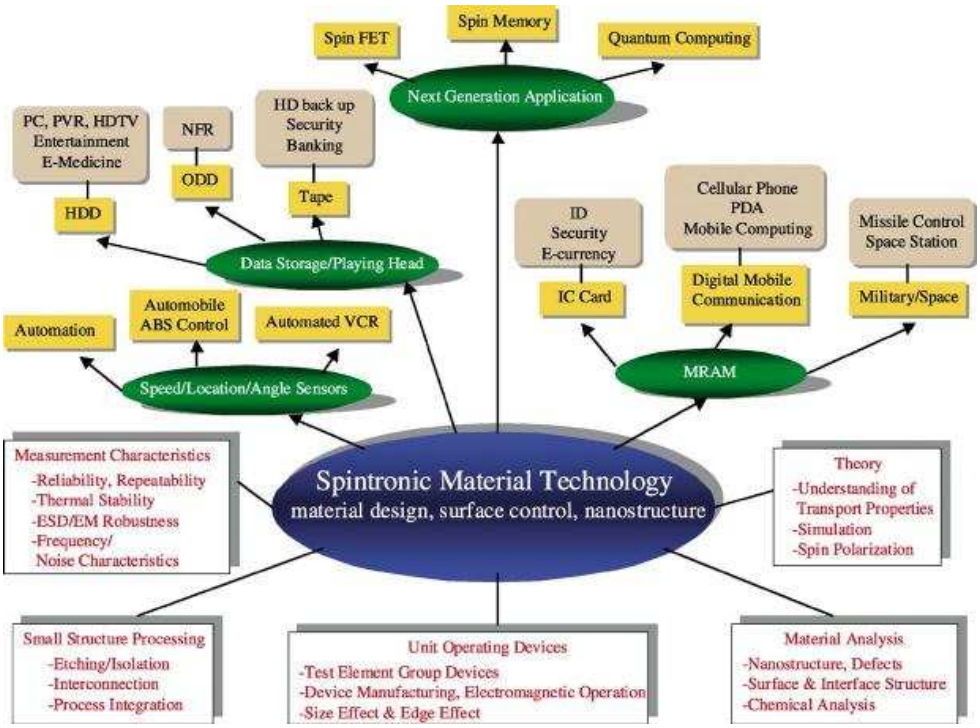

Figure 2.1 Technology tree for spin-based devices and their potential applications [1]

In fact, many challenges regarding the practical application of spintronic devices still need to be addressed and studied, such as the improvement of the electron spin lifetimes, the detection of spin on the nano scale and the effective transport of spin-polarised carriers within the host ferromagnetic material and across the interface of heterostructures, etc. One aim is to find suitable ferromagnetic semiconductors that allow spin-polarised carriers to be injected, but carrier transport and manipulation remain major issues.

2.2.1 Candidate materials for semiconductor spintronic applications

There are a number of essential requirements for a ferromagnetic semiconductor to be suitable for a practical spintronic device [1,2]. Firstly, the material should exhibit ferromagnetism up to practical temperatures of at least 500 K for a wide range of applications without temperature restriction, i.e. the magnetic transformation

temperature (Curie temperature, T_C) of this material should be over 500 K. Secondly, there should be an existing technology base that facilitates the development of a wide range of device configurations. Thirdly, the ferromagnetism should originate from a low density of carriers which allows the ferromagnetic properties to be tunable by doping or by gating. Fourthly, the material should exhibit magneto-optical effects that allow the optical readout of magnetically stored information. Based on these criteria, the advantages and disadvantages of each candidate material to date can be briefly appraised.

Early studies in the late 1960s to early 1970s showed that Cr spinels, rocksalt Eu and Mn-based chalcogenides exhibit a number of interesting properties due to the exchange interactions between the electrons in the semiconducting bands and the localised electrons in the magnetic ions [10,11]. However, the big difference in lattice structure between these materials and Si and GaAs, and the significant difficulty in growing these materials greatly inhibited further research work.

As illustrated by Figure 2.2, a semiconductor can be made magnetic by introducing transition metal elements into the semiconductor matrix. This type of ferromagnetic semiconductor is termed a dilute magnetic semiconductor (DMS), in which a sizable portion of the non-magnetic cations are replaced by magnetic elements (transition metals or rare earths). In the late 1980s, the $In_{1-x}Mn_xAs$ alloys was successfully demonstrated by researchers at IBM using molecular beam epitaxy (MBE) [12,13]. The subsequent discovery of a T_C as high as 110 K in GaMnAs generated much attention [14] and initiated the widespread search for room temperature DMS materials.

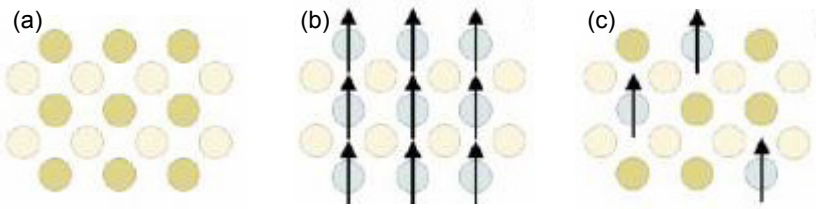

Figure 2.2 Three types of semiconductor: (a) a non-magnetic semiconductor, which contains no magnetic ions; (b) a magnetic semiconductor, containing a periodic array of a magnetic element and (c) a dilute magnetic semiconductor, an alloy of a non-magnetic semiconductor with a loose dispersion of a magnetic element [10].

The preparation process of DMS meterials becomes relatively easier for II-VI based semiconductors, such as CdTe and ZnSe due to the same cation valence as magnetic ions such as Mn. Unfortunately, this creates a difficulty in establishing p- or n-type doping. Further, the interaction between the localised magnetic moments becomes dominated by antiferromagnetic exchange even at the lowest achievable temperatures, which makes II-VI materials less attractive [10,15].

III-V semiconductors have already been used extensively in a variety of electronic and optoelectronic devices. Based on a well established technology for this material system, the replacement of a proportion of cations with magnetic elements for the purpose of carrier induced ferromagnetism should provide for new possible applications. In practice, however, magnetic elements, such as Mn, cannot be easily incorporated into the matrix, due to their limited solid solubility within these materials, without forming precipitates. The clear need for a way of producing uniform III-V based DMS alloys under non-equilibrium conditions inspired the introduction of MBE into the area of research. The successful demonstration of GaMnAs [16] and InMnAs [12,13] with varying Mn concentration (1~10 at%) using MBE has led to reports of ferromagnetism for several Mn-doped III-V

semiconductors, e.g. GaMnP [17], GaMnN [8] and GaMnSb [18]. Amongst them, GaN alloyed with Mn has been widely investigated because of the theoretical prediction suggesting that a Curie temperature over room temperature is possible for GaMnN containing 5 at% of Mn and with a hole concentration of 3.5×10^{20} cm^{-3} [3].

In parallel, the search for alternative materials exhibiting large carrier spin polarisations has continued. Despite the performance of ferromagnetic oxides in offering quite high Curie temperatures (CrO_2 387 K, Sr_2FeMnO_6 420 K, $La_{0.7}Sr_{0.}3MnO_3$ 280-380 K and Fe_3O_4 860 K, respectively), the long-term prospects for half-metallic ferromagnetic oxides are still not clear due to the underpinning challenges at the interface between the oxide and the material into which the spin carriers are to be injected and the trend of magnetic disorder at the terminal layer [19]. Other candidates are the Heusler alloys (e.g. Co_2MnSi, Co_2MnGe, Co_2MnSN, Fe_2MnSi, NiMnSb and PtMnSb, etc). They exhibit more complicated structures, with four interpenetrating fcc sublattices with atoms at $X_1(0,0,0)$, $X_2(1/2,1/2,1/2)$, Y(1/4,1/4,1/4) and Z(3/4,3/4,3/4). For the full Heusler alloys (X_2YZ), the X (X_1 and X_2) and Y positions are normally occupied by two different transition elements, such as Ni, Co, Fe, Pd or Pt, etc, whilst the Z positions are occupied by a group III, IV or V element, such as Al, Ga, In, Si, As or Sb, etc. For half Heusler alloys (XYZ), the X_1 positions are empty. Therefore, III-V compound semiconductors may be treated as a special case, where both X_2 and Y positions are not occupied. Even though this large class of materials demonstrate very high Curie temperatures and their crystal structures and lattice parameters are similar to many compound semiconductors, the control of composition, atomic ordering and defects both in the film and at the interface again remains a big challenge [20]. Co-doped ZnO grown on sapphire and

Co-doped TiO_2 (anatase) grown on $LaAlO_3$ and $SrTiO_3$(001) are also candidate DMS semiconductors, offering both room temperature ferromagnetism (T_Cs of at least 350 K for Co-doped ZnO and 700 K for Co-doped TiO_2) and optical transparency [21]. However, the growth and functional properties of these materials are far from being understood.

2.2.2 The Zener Model

A key breakthrough was made by Dietl et al [3] who calculated theoretical Curie temperatures for a number of wide bandgap semiconductors based on the mean-field Zener Model. Accordingly, for III-V semiconductors, the ultimate Mn moment alignment originates from the hybridization between d-orbitals on cation sites and orbitals in the partially filled valence band that are centred on neighbouring anion sites. For example, Mn dopants occupying the Ga sites of GaMn (N, P, As or Sb) provide both the local magnetic moments on the d-orbitals and holes (acceptor sites) in the valence band. It is possible for the alloy system to achieve an alignment of the Mn moments through spin-dependent coupling of the localised states in the Mn d-orbitals and the valence band holes.

The T_C values computed for various semiconductors containing 5 at% of Mn with a hole concentration of 3.5×10^{20} cm^{-3} are presented in Figure 2.3. It was suggested that Mn-doped zinc-blende GaN and ZnO are the two most promising materials for practical room temperature ferromagnetism (the predicted T_C value for cubic GaMnN is 6% higher than that for hexagonal GaMnN in this case). This prediction triggered widespread research into magnetically doped nitrides and oxides, as promising candidates for practical semiconductor spintronic applications.

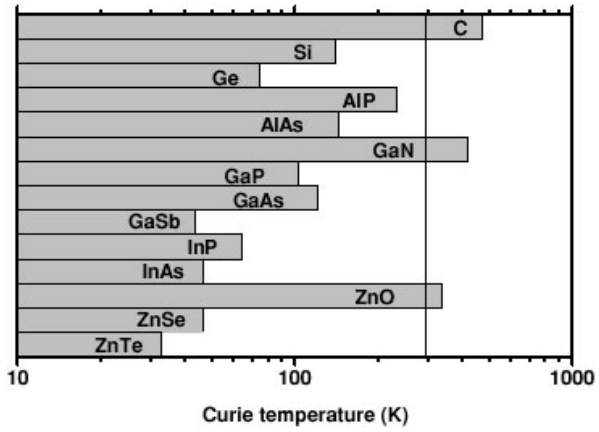

Figure 2.3 Calculated Curie temperatures for various semiconductors containing 5 at% of Mn, with a hole concentration of 3.5×10^{20} cm^{-3} [11]

In particular, the mean-field theory has been very successful in explaining many magnetic and transport properties of GaMnAs, showing good agreement with experimentally determined values for T_C and the development of magnetic anisotropy. Since T_C is proportional to both the Mn ion concentration and the density of holes, this model also suggests that T_C values above 300 K may be achievable in uniform GaMnAs alloys with 10 at% Mn, even though such a concentration is far beyond the solid solubility of Mn within GaAs.

2.2.3 GaMnAs as a model material

Despite the steady progress achieved using low temperature MBE, the record Curie temperature for GaMnAs to date remains quite low (to date, the highest T_C of 173 K for single crystal GaMnAs grown using MBE following annealing was obtained by the Nottingham group [22], with high value of ~172 K obtained in carefully engineered heterostructures [23]). Even for quaternary alloys such as $(In_{0.5}Ga_{0.5})_{0.93}Mn_{0.07}As$, the Curie temperature only reaches a value of 110 K [1]. At this stage, it is still not certain if room temperature ferromagnetism is achievable for

the GaMnAs. However, due to its compatibility with the well-established GaAs system, GaMnAs provides a valuable testing ground for DMS properties and also provides opportunities to improve the understanding of carrier-induced ferromagnetism.

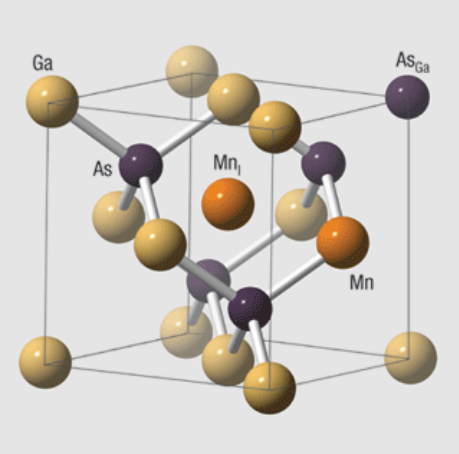

Figure 2.4 Illustration of the lattice structure of GaMnAs showing Mn occupying Ga sites and two possible Mn interstitial and As antisite point defects [2]

GaMnAs is a zinc-blende GaAs crystal containing a small fraction of Mn atom which substitute for Ga atoms providing holes that mediate a spin-dependent coupling between the localized magnetic moments of the Mn atom d shells. It is evident from Figure 2.5 that there is a strong relationship between the T_C and hole concentration. In order incorporate so large an amount of Mn without the formation of Mn-rich precipitates, p-type GaMnAs needs to be grown on (001) orientated GaAs substrates using MBE at low temperatures. Briefly, GaMnAs layers are normally grown on semi-insulating GaAs substrates by low-temperature MBE at 200~250 °C in order to achieve above equilibrium concentrations of Mn [16,24,25]. Prior to the low-temperature growth of the active GaMnAs layer, two buffer layers of high-temperature GaAs and low-temperature GaAs, are initially deposited sequentially. In-

situ reflection high-energy electron diffraction (RHEED) may be used to monitor the surface reconstructions during growth [24]. The GaMnAs growth is initiated by simply opening the Mn shutter without the need for special precaution.

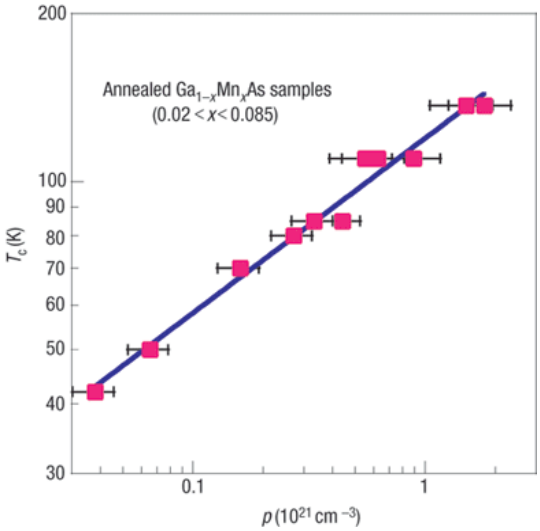

Figure 2.5 Curie temperature of a range of GaMnAs samples obtained after annealing as a function of hole concentration, obtained from Raman scattering measurements [2]

2.2.3.1 Point defects within GaMnAs

In fact, the low-temperature epitaxy process inevitably leads to a high concentration of point defects, namely As antisites (As_{Ga}) and Mn interstitials (Mn_I), both being believed to be double donors that compensate holes provided by substitutional Mn_{Ga} (with possible corresponding locations illustrated in Figure 2.4) [2,26]. In particular, the Mn interstitials are thought to be detrimental because they also have strong local direct antiferromagnetic coupling to any neighboring substitutional Mn atoms. It has been demonstrated that post-growth annealing at relatively low temperatures is an effective way of modifying sample key parameters, such as the lattice constant, the hole density and the ferromagnetic transition temperature [27-29]. By way of

example, combined channeling Rutherford backscattering (CBS) and particle-induced X-ray emission measurements (PIXE) suggested that the concentration of the unstable and highly mobile Mn interstitials were reduced by the annealing process, leading to a large variation in T_C depending on the annealing temperature [28]. In addition, Edmonds et al [29] found that careful control of the annealing conditions induces the Mn interstitials to diffuse towards the growth surface, accompanied by an increase in ferromagnetic transition temperature.

2.2.3.2 α-MnAs precipitates

Another partitioning method for the excess Mn within GaMnAs is to form more thermodynamically stable Mn-rich precipitates. Amongst them, α-MnAs is widely recognized and this compound has even been investigated separately as a promising candidate for semiconductor spintronic applications. The α-MnAs is a ferromagnetic material with a NiAs-type hexagonal structure (a=0.3724 nm, c=0.5706 nm) and a T_C of 313 K in the bulk [13,30]. The lattice structure is illustrated in Figure 2.6.

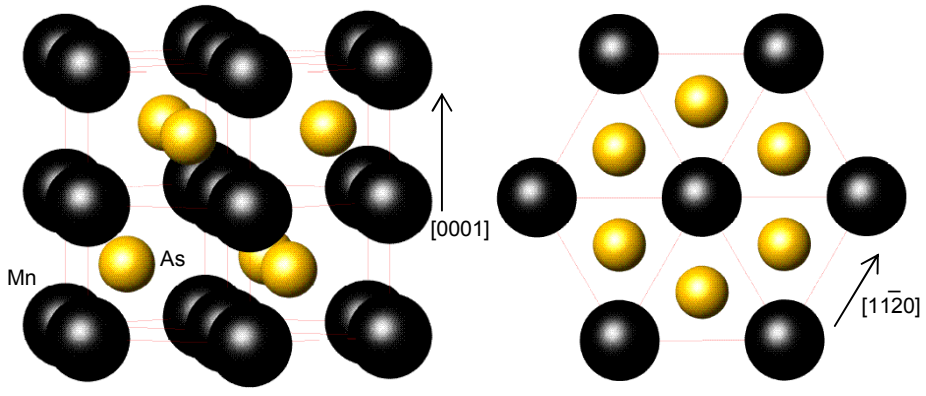

Figure 2.6 Perspective views of the α-MnAs lattice structure.

The first identification of MnAs precipitates was made within InMnAs according to a detectable ferromagnetic signal up to 310 K [13] and extra peaks in the XRD spectra

[12], both being attributed to the formation of MnAs-like cluster as distinct from the alloy phase. Concerning case of GaMnAs, when the Mn flux and/or the growth temperature are too high, diffraction spots within RHEED patterns were attributed to the formation of a MnAs second phase, being confirmed later by XRD [25].

Independently, attempts have been made to study MnAs as a promising ferromagnetic semiconductor. MnAs nanocrystals (e.g. Figure 2.7) embedded within GaAs were prepared using MBE grown GaMnAs, followed by rapid high temperature annealing for 20~30 s at 600~700 °C [31-33]. The MnAs maintained a well defined orientation relationship with respect to the GaAs matrix, being $(0001)_{MnAs}$ // $\{111\}_{GaAs}$ and $<2\bar{1}10>_{MnAs}$ // $<011>_{GaAs}$ or $<0\bar{1}1>_{GaAs}$, or most frequently being $[2\bar{1}\bar{1}0]_{MnAs}$ // $[110]_{GaAs}$ and $(0001)_{MnAs}$ // $(1\bar{1}\bar{1})_{GaAs}$. Even though there exited anisotropic lattice distortions, the MnAs within GaAs exhibited robust ferromagnetism with an enhanced magnetic transition temperature of ~330 K, being 17 K higher than that of bulk MnAs.

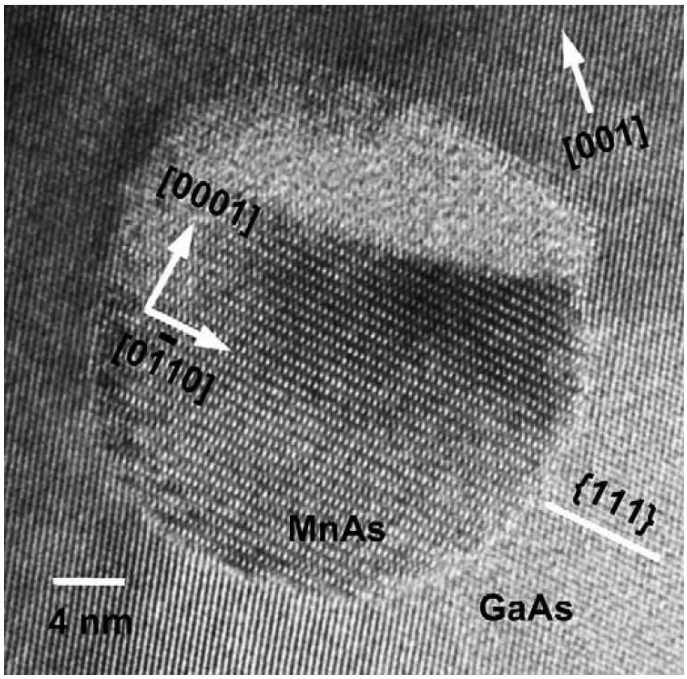

Figure 2.7 HREM image of a sample with an overall Mn concentration of 8 at%, obtained along the [110] projection, showing a MnAs precipitate embedded within the GaAs matrix [33].

Despite the dissimilarity between α-MnAs and GaAs in crystal structure, lattice constant and nature of chemical bonding, the direct growth of MnAs thin films on GaAs substrates has been successfully performed using MBE [34-37]. Two sets of distinct orientation relationships have been reported by Schippan et al [34] and Tanaka et al [35-37], respectively. By analyzing RHEED patterns recorded along the orthogonal $<110>_{GaAs}$ projections during MnAs growth on GaAs(001) substrates, Schippan el al [34] found that the principal epitaxial orientation relationship for MnAs on very As-rich GaAs surfaces are $(\bar{1}100)_{MnAs}$ // $(001)_{GaAs}$ and $[0001]_{MnAs}$ // $[\bar{1}10]_{GaAs}$. However, depending on the GaAs substrate surface stoichiometry, MnAs growth conditions and layer thickness, a less important orientation relationship of $(\bar{1}100)_{MnAs}$ // $(001)_{GaAs}$ and $[0001]_{MnAs}$ // $[110]_{GaAs}$ was also identified. In parallel, based on RHEED patterns and confirmed by subsequent XRD and TEM analysis, Tanaka et al [35-37] suggested two epitaxial relationships between MnAs and GaAs, with type A

being $[\bar{1}\bar{1}20]_{MnAs}$ // $[110]_{GaAs}$ and $[0001]_{MnAs}$ // $[\bar{1}10]_{GaAs}$ and type B being $[\bar{1}\bar{1}20]_{MnAs}$ // $[\bar{1}10]_{GaAs}$ and $[1\bar{1}02]_{MnAs}$ // $[110]_{GaAs}$.

2.3 Introduction to GaN

As previously mentioned, because of the theoretical prediction suggesting that a Curie temperature well above room temperature is possible for GaN containing 5 at% Mn and a hole concentration of $3.5\times10^{20}cm^{-3}$ [3], attention is presently being given to the development of p-type GaMnN ferromagnetic semiconductors. In order to incorporate Mn at suitable levels within GaN, in view of its limited solid solubility, it becomes necessary to use non equilibrium growth techniques such as plasma-assisted molecular beam epitaxy (PAMBE). In the first instance, to assist with the investigation of the effect of Mn incorporation on the development of the GaMnN microstructure, it is appropriate to briefly review the associated literature for the epitaxial growth of GaN, in particular, for zinc-blende GaN, using MBE.

2.3.1 GaN lattice structure and polarity definition

In contrast to cubic III-V semiconductors like GaAs and InAs which naturally exhibit the zinc-blende lattice structure, the thermodynamically stable phase for GaN at ambient conditions is the hexagonal wurtzite structure (α-phase) (lattice parameters, a=3.189 Å and c=5.186 Å), although the cubic GaN zinc-blende structure (β) (lattice parameter, a=4.52 Å) may be stablised by epitaxial growth on the (001) crystal plane of certain cubic substrates. Because the α-phase and β-phase only differ in the stacking sequence on close packed planes, i.e. {0001} planes for α-GaN and {111}

planes for β-GaN, it is quite possible for the epitaxial layer to contain both phases, e.g. due to planar defects such as stacking faults.

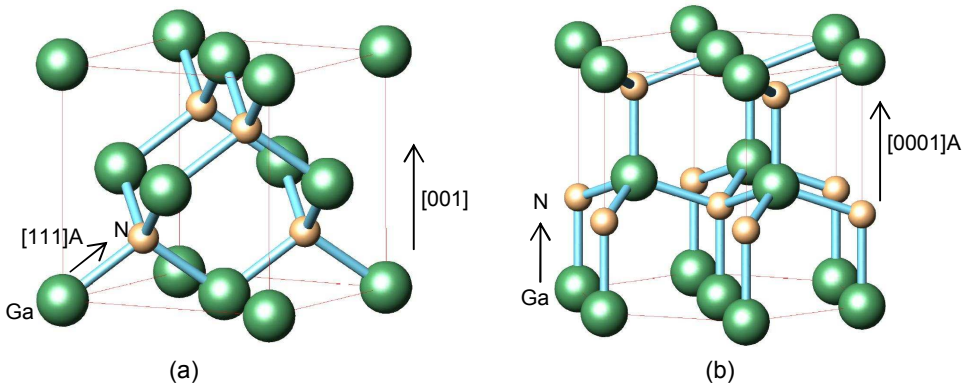

Figure 2.8 Lattice structures of (a) zinc-blende GaN and (b) wurtzite GaN with principal directions labelled according to the polarity definition.

For zinc-blende GaAs or GaN, the covalent bonds are polar and the [111]a direction is conventionally defined as the bonding direction from the Ga atom to the As or N atom [38]. Considering the symmetry of the zinc-blende structure, the definition of another direction is also required for the complete indexing of each set of planes and directions within the unit cell. Conventionally, if the growth plane for GaAs or GaN is (001) oriented, the growth direction is defined as the [001] direction. Therefore, the family of A planes are labelled as (111)A, $(\bar{1}\bar{1}1)A$, $(\bar{1}1\bar{1})A$ and $(1\bar{1}\bar{1})A$, with even number of negative indices. Similarly, the family of B planes are labelled as $(\bar{1}\bar{1}\bar{1})B$, $(\bar{1}11)B$, $(1\bar{1}1)B$ and $(11\bar{1})B$, with an odd number of negative indices. For wurtzite GaN, the same rule for defining the bonding direction is applicable, leading to the definition of the absolute [0001] and $[000\bar{1}]$ polar directions.

2.3.2 Properties and applications of GaN

A brief summary of the physical properties of both wurtzite and zinc-blende GaN is given in Table 2.1. Based on these properties, GaN has become an attractive semiconductor for many electronic and optoelectronic devices [39,40]. By way of example, the direct bandgap of GaN and its In and Al alloys span most of the visible spectrum and extends well into the ultraviolet region. This makes GaN suitable for optoelectronic devices, such as LEDs, laser diodes (LDs) and short wave length detectors, being active at green, blue or UV wavelengths. Due to its wide band gap nature, good thermal stability and high breakdown fields, GaN is also advantageous for high temperature / high power electronics, including microwave radio-frequency power amplifiers and high-voltage switching devices for power grids.

Table 2.1 Basic properties of wurtzite and zinc-blende GaN at 300 K

Property	GaN (α)	GaN (β)
Crystal structure	Hexagonal	Cubic
Space group	C_{6V}^4 (=P6$_3$mc) [41]	$F\bar{4}3m$ [41]
Lattice constant (a) Å	a=3.189, c=5.189 [41]	a=4.52 [41]
Density (g cm^{-3})	6.10 [42]	6.11 [43]
Energy gap (eV)	3.34 (room temperature) [42]	3.2 (300K) [43]
Mobility of electrons (cm^{2}V^{-1}s^{-1})	≤1000 [41]	≤350 [41]
Mobility of holes (cm^{2}V^{-1}s^{-1})	≤200 [41]	350 [41]
Infrared refractive index	2.3 [41]	2.3 [41]
Bulk modulus (dyn cm^{-2})	20.4×10^{11} [41]	20.4×10^{11} [41]
Melting temperature (°C)	2500 [41]	2500 [41]
Thermal conductivity [W cm^{-1} °C^{-1}]	1.3 [41]	1.3 [41]
Thermal expansion coefficient [10^{-6} K^{-1}]	Δa/a=5.59×10^{-6}, Δc/c=3.17×10^{-6} [43]	N/A

2.3.3 Epitaxial growth of GaN

Generally, the crystal structure of GaN adopted during heteroepitaxial deposition depends strongly on the growth condition, substrate material and orientation of the substrate (see the reviews by Strite and Horkoç [44], Liu and Edgar [45] and Orton and Foxon [46] and references therein). Wurtzite GaN may be grown on a wide

variety of substrates, including Al_2O_3, SiC, Si, $LiGaO_2$, GaAs and GaP, by a variety of epitaxial growth techniques, such as halide vapour phase epitaxy (HVPE), metal organic chemical vapor deposition (MOCVD) and MBE. In fact, sapphire has become the primary substrate due to its wide availability, hexagonal symmetry and ease of handling and cleaning. Since the zinc-blende phase of GaN is considered to be less stable than the wurtzite phase, the growth conditions need to be carefully controlled on appropriately selected substrates for the purpose of obtaining a single crystal material. To date, the growth of zinc-blende GaN has been demonstrated on a variety of differently oriented substrates, e.g. GaAs, GaP, Si, MgO and SiC, using a number of epitaxial growth techniques, e.g. MOCVD, HVPE and MBE. Amongst these growth techniques, MBE is mainly employed, where the growth process can be operated under non-equilibrium conditions, being beneficial for the formation of the zinc-blende GaN.

MBE growth of zinc-blende GaN on GaAs(001)

In order to grow high-quality cubic GaN without the presence of the hexagonal phase, the initial nucleation stage needs to be carefully controlled. Nitridation of the substrate prior to growth, i.e. exposing the substrate to an active N beam, appears to be essential for the subsequent formation of the zinc-blende phase [47-49]. In addition, it was found by Cheng et al [50] that the introduction of an As beam together with the Ga and N beams at the earliest stage of the growth, allows pure cubic GaN to be obtained, depending on the growth temperature used.

Following the nucleation process, an optimum growth condition, mainly a combination of the substrate temperature and the surface stoichiometry, needs to be

well maintained [49,51,52]. In particular, surface stoichiometry is found to have a dominant effect on the development of the cubic GaN phase. Indeed, SEM observations showed that N-rich conditions are associated with a severe roughening of the surface morphology. In comparison, under Ga-rich conditions, a dramatic reduction in surface roughness and improvement in the epilayer microstructure were observed. Further, exact control of the III:V ratio close to the stoichiometric condition during MBE growth allows the production of single phase zinc-blende epitaxial layers, whilst deviation to Ga or N-rich conditions reportedly produces mixed phase zinc-blende and wurtzite materials [49,51,52].

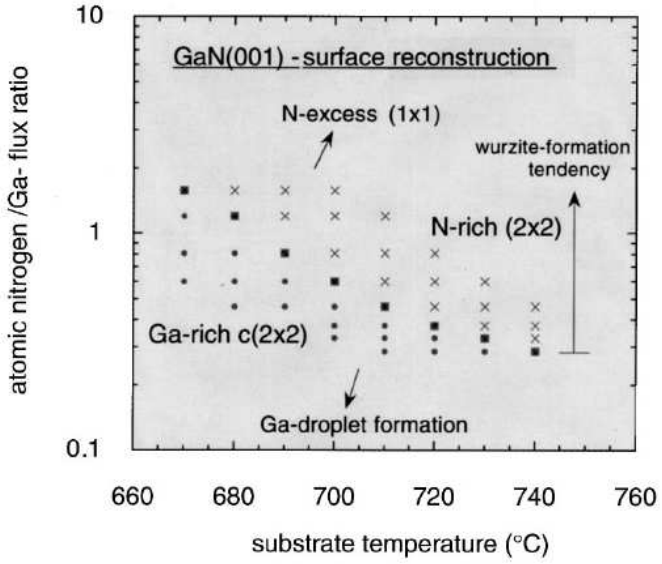

Figure 2.9 Surface reconstruction diagram of zinc-blende GaN as a function of growth temperature and the N:Ga ratio [53]

In order to understand the fundamental growth mechanisms, the surface reconstructions of zinc-blende GaN grown on (001) oriented GaAs by MBE have been investigated combining RHEED, scanning tunneling microscopy (STM) and first-principle calculations [49,53-56]. Based on the analysis of in situ RHEED patterns in exposure to a trace level of As, Brandt et al [49,54] concluded that the

(1×1) pattern corresponds to a N-terminated surface under N-rich conditions, whereas (2×2) and c(2×2) patterns were established on Ga stablised surfaces covered with an 0.5 or 1.0 monolayer of Ga, respectively, with the latter considered to be a stable growth mode resulting in the pure cubic GaN phase. Identical surface reconstruction observations have also been reported by Schikora et al [53] and Feuillet et al [55]. First principle total-energy calculations have been carried out suggesting that for both clean and As-mediated zinc-blende GaN, in a similar fashion to wurtzite GaN, the surface energy always becomes lower if the growth is transferred from N-rich to Ga-rich conditions [56]. This means, independent of the growth conditions, that the growth surface of GaN is always terminated by Ga adatoms, whose free mobility [57,58] and surface lifetimes [59] determine the resultant crystal microstructure.

Generally, the growth of thin epitaxial films occurs in one of the three modes [60]: (i) 2D layer-by-layer growth, (ii) 3D island growth and (iii) 2D layer growth followed by 3D island growth, proposed first by Stranski and Krastanow (SK). The 2D layer-by-layer growth mode can be adopted only in systems with either zero or small lattice mismatch of less than 2 %, while the SK mode is more representative of systems with similar materials and a higher lattice mismatch, i.e. larger than 2 %. In view of the large lattice mismatch between GaAs(001) and GaN(001), which is ~20 % with regard to the GaAs, the 3D island growth mode should take priority at the start of the heteroepitaxy. TEM studies of GaN thin films provide valuable information concerning the resultant defect microstructure, being particularly important for the appraisal of the integrity of the epilayer substrate interface [61-65]. As a direct consequence of the large lattice mismatch, at every fifth GaN {111} plane, a regular pure edge-type misfit dislocation located at the interface was observed by Trampert et

al [61] (Figure 2.10a). They also suggested that nucleation occurs by the formation of nanoscale 3D islands with a well-defined epitaxial relationship, each of which contains two edge-type misfit dislocations, one in the centre and the other at the edge of the island. In addition, pits of size less than 200 nm, formed into the GaAs(001) substrate were identified by Tricker et al [63]. These feature were attributed a sourcing of Ga from the substrate during the first stages of epitaxy. As to the bulk of the epilayer, a high density of stacking faults and microtwins propagating on {111} planes are common growth defects for cubic GaN grown on (001) oriented GaAs substrates (Figure 2.10b) [61].

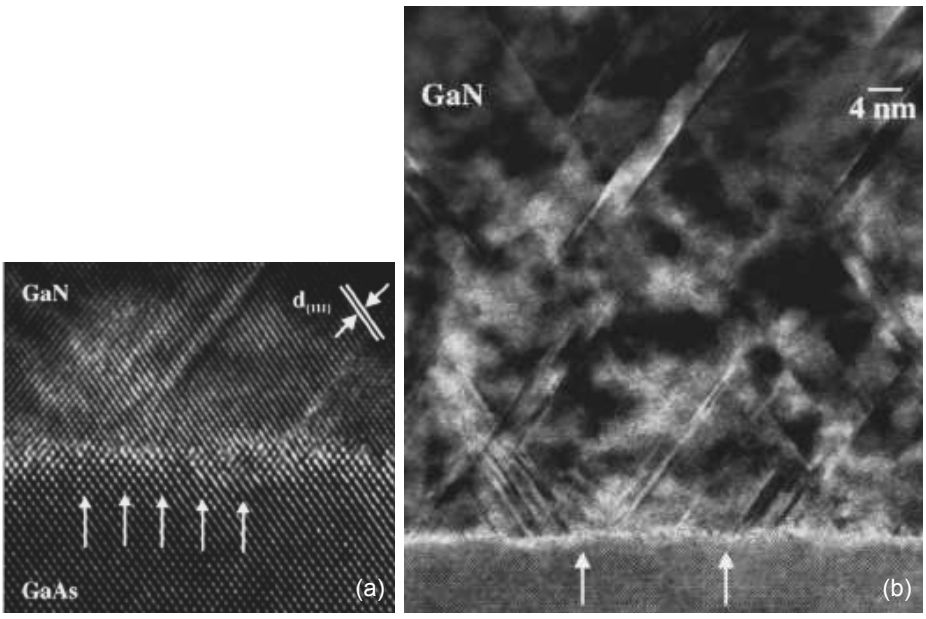

Figure 2.10 Cross sectional HREM images of the interface of a GaN sample grown on GaAs(001) showing (a) regular edge-type misfit dislocations and (b) planar defects propagating on {111} planes [61].

In cubic GaN grown on GaAs(001) substrates, regions of hexagonal phase might also exist, normally maintaining a well defined orientation relationship with respect to the cubic GaN matrix, i.e. $\{111\}_\beta$ // $\{0001\}_\alpha$ and $<110>_\beta$ // $<11\bar{2}0>_\alpha$ [61,63]. In most of studies using XRD, a θ-2θ scan is performed without sample tilting. In fact, this kind

of simple scan mode provides diffraction information only from crystallographic planes roughly parallel to the surface of the epilayer, e.g. $(001)_\beta$ planes. Therefore, spectra obtained using the θ-2θ scan mode may be used to confirm the cubic epitaxy, but are not well suited to appraise the presence of the hexagonal phase. XRD pole figures and reciprocal lattice maps based on 3D sample tilting should be employed to give a more complete picture of the phase composition [66-68].

2.4 Growth and properties of GaMnN

2.4.1 Introduction

Already, there have been many experimental reports regarding the preparation, and magnetic and transport properties of GaMnN. A summary regarding the preparation techniques, substrates, second phases identified and the two key functional properties, i.e. the type of carrier and the Curie temperature, is presented in Table 2.2. It is apparent that the preparation techniques employed for the incorporation of Mn into GaN are dominated by the direct growth technique of MBE, including rf-plasma-assisted MBE [69-73], ECR-plasma-assisted MBE[74], reactive-MBE [75,76], and MBE without additional activation sources, using compound precursors instead [77-79]. There are also other techniques which have been used for the purpose of generating ferromagnetic GaMnN, such as MOCVD or MBE grown GaN followed by Mn ion implantation and annealing [6,80,81], MOCVD grown GaN followed by laser deposition of Mn [82,83], nebulised spray pyrolysis [84] and ammonothermal method (AMMONO)[1] [85,86].

[1] The ammonothermal method (also known as 'AMMONO') utilizes a solution / reaction mechanism which allows well defined and high purity microcrystalline grains of GaMnN to be formed.

As mentioned previously, theoretical work by Dietl et al [3] suggests that Curie temperatures over room temperature for both cubic and hexagonal GaMnN are possible, with that of the latter being 6% lower under the same doping conditions, i.e. 5 at% of Mn and a hole concentration of 3.5×10^{20} cm^{-3}. In parallel, even though the growth process of cubic GaN has been well established, it is still quite difficult to avoid the presence of hexagonal domains due to the nature of the highly faulted structure of cubic GaN. Therefore, initial attention has mainly been given to the growth of hexagonal GaMnN, with a view to making the preparation process more straightforward. Experimentally, however, most authors reported that, no matter what the growth technique, the hexagonal GaMnN phase is n-type, with only two exceptions reported by Kim et al [78,79] and Baik et al [81]. In comparison, p-type cubic GaMnN has been routinely demonstrated using MBE growth on GaAs(001) substrates [78,79] and by Mn ion implantation of GaN followed by high temperature annealing [6].

Further, in view of the limited solid solubility of Mn within GaN, a variety of Mn-rich precipitates have been observed and / or identified using XRD and TEM. These types of Mn-rich second phases have become one of the major issues for the continued development of this materials system, because they are considered to be closely connected with the wide range of magnetic properties observed, with reports of T_C values, varying from ~200 to even 940 K [87], strongly depending on the growth technique and corresponding growth parameters. However, very limited information on these phases, such as their crystal structure and composition, was experimentally provided.

Since MBE has played a key role in the realization of GaMnN based ferromagnetic semiconductors, a review regarding their growth and corresponding functional properties is given in Section 2.4.2, with other preparation methods, being briefly described within the next section.

Table 2.2 Survey of growth techniques and functional properties of GaMnN

Growth technique	**Substrate / buffer layers**	**Mn at%**	**α/ β**	**Tg (MBE) (°C)**	**Annealing (°C)**	**Second phase precipitates (identification tech)**	**type of carrier**	**T_C (K)**	**Ref(s)**
laser deposition + MOCVD	HT-GaN / LT-GaN + annealing / Sapphire(0001)	1 - 2	α		250 - 800 °C	Mn_3GaN (XRD)		220-370	[82,83]
ion-implantation + MOCVD	p-type, n-type and intrinsic MOCVD GaN / sapphire(0001)	< 3	α		700 - 900 °C after implantation	$Mn_{4-x}Ga_xN_{2-y}$ or Mn_8Ga_5; $Mn_6N_{2.58}$ and Mn_3N_2 (XRD)		RT	[80]
Ion implantation + MOCVD	MOCVD Mg-doped GaN / sapphire(0001)	5	α		700 - 900 °C after implantation	Mn_3Ga at 700 °C, disappears later at 900 °C, $Mn_6N_{2.58}$ at 700 °C, Mn_3N_2 at 900 °C (XRD and TEM)	p		[81]
Ion implantation + PAMBE	PAMBE GaN on GaAs(001)	0 - 2.8	β		950 °C after implantation		p	RT	[6]
nebulized spray pyrolysis	-	3						250	[84]
AMMONO	-	< 5	α			Mn_3N_2 (XRD)		paramagnetic	[85]
MOCVD	MOCVD GaN buffer/sapphire(0001)	1, 1.2 & 1.5	α	900 - 1050			semi-insulating	RT	[88]
MOCVD	sapphire(0001) (GaMnN epilayer grown with Mg codoping)	~10^{20} atoms/cm^3	α					ferromagnetic	[89]
reactive-MBE	LT-GaN / sapphire(0001)	0.45 - 12	α	750 - 850		Extra peaks from XRD (12 at% Mn)		400	[75]
reactive-MBE	semi-insulating Si-face SiC(0001)	7.6 - 13.7	α	710		Second phase precipitates (TEM)		750 (13.7 at% Mn)	[76,90]
MBE	MOCVD GaN / sapphire(0001)	9 & 6	α	720			n	300-750 and 940	[87]
RF-PAMBE	GaN / MOCVD GaN buffer / sapphire(0001) or GaN / GaN buffer / AlN /sapphire (0001)	≤ 43	α	700 - 925		MnGa (43 at% Mn); tetragonal $Mn_{0.6}Ga_{0.4}$ (43 at% Mn) (XRD)	n	RT (3 at% Mn)	[17]
MBE	MOCVD GaN / sapphire(0001) or sapphire	< 6	α	600, 700, 925				350	[71]
RF-PAMBE	MOCVD Ga-polar GaN(0001) / sapphire (Si-doped n-type or unintentionally doped n-type)		α	550		GaMn and Mn_4N suggested by magnetic measurements		< 300 depending on growth conditions	[69,91]
RF-PAMBE	MOCVD GaN(0001)/sapphire(0001)		α	700				RT	[92]
RF-PAMBE	MOCVD GaN(0001)/sapphire(0001)	0.16 - 0.5	α	350 - 700			n	500 - 700	[93]

RF-PAMBE	MOCVD GaN(0001)/sapphire(0001)	0.2	α	700			n		[70]
RF-PAMBE	MOCVD GaN / sapphire(0001)	0.06-0.5	α	700			n	550 - 700	[94]
RF-PAMBE	MOCVD GaN/sapphire(0001)		α	710 - 730		$GaMn_3N$ or Mn_4N		400 (0.3 at% Mn)	[72,95]
RF-PAMBE	AlN /sapphire(0001) or MBE GaN / n-type GaN (MOVPE) / sapphire		α	500 - 800		considered to be due to second phase Ga-Mn and Mn-N	n	paramagnetic	[73]
RF-MBE	sapphire(0001)		α	400 & 650	400 °C growth + 650 °C annealing	formation of Mn-rich clusters (suggested by EXAFS)		paramagnetic	[96]
PAMBE	700 C GaN buffer/ 900 C annealing/ 500 C buffer/ sapphire	1, 4	α	500-800		Mn_3N_2 or Ga_xMn_y (XRD)	n	300 (1 at% Mn); 200 (4 at% Mn)	[97]
MBE	sapphire(0001)		α	700		Mn_3GaN (XRD)	p	RT	[78,79]
MBE	sapphire(0001)		α	650		Mn_3Ga, Mn and Mn_3GaN (XRD)		RT	[77]
ECR-PAMBE	GaN buffer/6H-SiC(0001) nitrogen doped with a dopant concentration of 10^{18} cm^{-3}	> 6	α	500		Mn_3N_2 (XRD) in the absence of H			[74]
MBE	GaAs(001)	< 6	β	550		Mn_3GaN (XRD)	p	RT	[78,79]

2.4.1.1 Mn ion deposition and implantation

Instead of the direct growth of GaMnN thin films using MBE or MOCVD, Mn ions may be incorporated into GaN films using laser deposition [82,83] or ion implantation [6,80,81]. These kind of indirect methods normally involve three steps, i.e. the GaN epitaxial growth, the Mn ion incorporation and the sample annealing at an appropriate temperature. Reed et al [82,83] confirmed using SIMS that Mn atoms were indeed introduced into the MOCVD grown hexagonal GaN lattice by the laser deposition technique, with a Mn concentration of ~1 at%. These films demonstrated a wide range of Curie temperatures from 228 to 370 K, depending on the growth and annealing conditions. Kane et al [80] compared GaMnN layers prepared by Mn ion implantation and MOCVD using bis-cyclopentadienyl manganese (Cp_2Mn) as the Mn precursor. Second phases, e.g. Mn_xN_y, Ga_xMn_y and $Mn_{4-x}Ga_xN_{1-y}$, were detected using XRD within the Mn ion implanted samples after subsequent annealing, whilst GaMnN thin films fabricated by MOCVD were uniform alloys with almost identical lattice parameters as that of un-doped GaN. All samples exhibited ferromagnetism well above room temperature, being considered to originate from the GaMnN alloys, or unobserved second phases such as Mn-rich clusters.

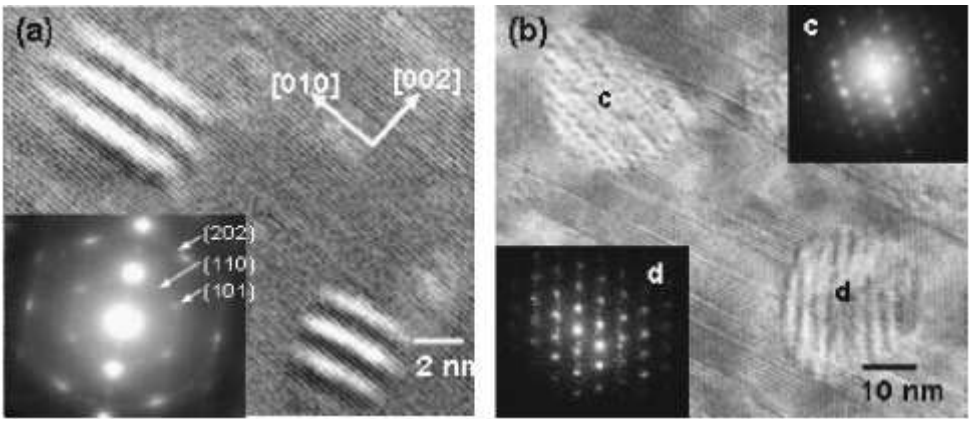

Figure 2.11 High resolution TEM micrographs and associated SAED patterns for Mn-implanted hexagonal GaN samples annealed at (a) 700°C and (b) 900°C, respectively. The SAED inset confirm the formation of additional phases of (a) Mn_3Ga, (c) $Mn_6N_{2.58}$ and (d) Mn_3N_2 [81]

In parallel, p-type conductivity within either hexagonal or cubic GaMnN, with Mn incorporated by ion implantation, has been demonstrated by Baik et al [81] and Chitta et al [6], respectively. Baik el al [81] reported on an investigation of Mn-implanted p-type GaN grown by MOCVD on sapphire using cross-sectional TEM, providing evidence that the ferromagnetic properties of these GaMnN films was connected with Mn-rich nanoclusters produced by annealing at different temperatures. Figure 2.11 shows cross-sectional TEM images of GaMnN samples annealed at 700 and 900°C, respectively. It was concluded that higher annealing temperatures promoted the formation of Mn_3N_2 and $Mn_6N_{2.58}$ rather than Mn_3Ga [81]. The weak ferromagnetic signal (sample annealing temperature ≤ 700°C) was attributed to the Mn_3Ga, whilst a reduced ferromagnetic signal (sample annealing temperature ≥ 900°C) was associated with the anti-ferromagnetic manganese nitrides, such as $Mn_6N_{2.58}$ and Mn_3N_2. In parallel, Mn ion implantation was performed in PAMBE grown cubic GaN on GaAs(001) substrates in order to generate p-type conductivity and room temperature ferromagnetism [6]. Four samples with different Mn doping levels ranging from 0.7 to 2.8 at% were annealed at 950°C. An assessment using high resolution XRD and

Raman spectrometry suggested that the annealing process led to a significant improvement in crystal structure and room temperature ferromagnetism was detected in these samples using superconducting quantum interference device.

2.4.1.2 MOCVD

Even though MOCVD is generally regarded as being the optimal technique for the growth of high quality III-nitrides, there are limited reports on the incorporation of Mn using MOCVD. By way of example, the magnetic and optical properties of MOCVD grown GaMnN films on sapphire(0001) with Mn concentrations of up to 1.5 at% were investigated by Kane et al [88]. The deposition was carried out on an MOCVD grown GaN buffer layer using compound precursors, including trimethyl gallium and ammonia and biscyclopentyldienyl manganese (Cp_2Mn) as the Ga, N and Mn sources, respectively. SIMS and high-resolution XRD indicated that the Mn was uniformly distributed throughout the epilayers and no extra peaks were detected. This sample, exhibiting Mn-related blue band luminescence, also exhibited stronger ferromagnetic behaviour which was maintained up to room temperature. Interestingly, Reed et al [89] found that the addition of Mg into GaMnN prepared by MOCVD transferred the material from being normally non-ferromagnetic to strongly ferromagnetic. Similarly, the ferromagnetic properties of some samples were further strengthened by the addition of Mg.

2.4.2 Growth of wurtzite GaMnN using MBE

The refined control of growth parameters and in-situ monitoring capability make MBE an ideal technology for the fabrication of GaMnN beyond the Mn thermodynamic limit under non-equilibrium conditions. However, nearly all the

reports concerning the growth and properties of GaMnN ferromagnetic semiconductors have been based on hexagonal materials. Given the metastable nature of cubic GaN, this may avoid the complexities due to α/β mixed phase growth within these epitaxial GaMnN films. To the best of this author's knowledge, in addition to the work reported by the group at Nottingham, only one group from Korea [78,79] has reported on the successful growth of p-type cubic GaMnN on (001) oriented GaAs substrates, using a single molecular precursor of $Et_2Ga(N_3)NH_2C(CH_3)_3$ for GaN and a solid Mn source, even though AFM and TEM examinations revealed these films to be polycrystalline.

Based on the well established growth processes for GaN using MBE, hexagonal GaMnN epilayers layers have been demonstrated by simply adding a solid or compound source of Mn [78,79] onto a number of substrates, including sapphire(0001) [96], semi-insulating SiC (0001) [76], MOCVD grown GaN buffer layers on sapphire(0001) [69,72,98], GaN buffer layers on 6H-SiC(0001) [74] and AlN buffer layers on sapphire(0001) [73]. In some cases, a capping layer was deposited at the end, preventing the oxidation of the sample surface [69,87]. A wide range of Mn content was used in order to investigate the effect of Mn incorporation on the epilayer microstructure and functional properties, with higher Mn concentrations normally leading to the development of a variety of second phase Mn-rich precipitates, confirmed by XRD and/or TEM or suggested by the measurement of magnetic properties. Other growth conditions, such as the Ga/N ratio [69,72,91,95], growth temperature [73,97], or co-doping using H [74], with reference to the magnetic and electrical properties and epilayer defect, have also been investigated.

2.4.2.1 Effect of nucleation layer

Thaler et al [71] investigated the effect of the nucleation layer on the magnetic properties of GaMnN. GaMnN layers were grown by gas source MBE (GSMBE) on three different hybrid substrates, i.e. sapphire(0001), an MOCVD grown GaN buffer layer and a GSMBE grown GaN buffer layer. It was found that films on the MOCVD grown GaN buffer layer exhibited the largest magnetic moment. Extended X-ray absorption find structure (EXAFS) experiments suggested that the positions of Mn within the GaN matrix were not affected by these starting layers, with the improvement in the magnetic properties being attributed to a reduction in the defect density.

2.4.2.2 Effect of the Ga/N ratio on the incorporation of Mn

As mentioned earlier, the growth mechanisms of both cubic and hexagonal GaN using MBE have been studied in detail [99]. The incorporation of Mn into the growth undoubtedly changes the growth regime, as recognized and investigated by Haider et al [69,91] and Kuroda et al [72,95]. Based on the experimental results for hexagonal GaMnN, both groups stated that Mn may only be incorporated into the GaN lattice under N-rich or nearly 1:1 stoichiometric growth conditions.

Haider et al [69,91] identified a metal-rich regime, lying between that of the Ga-rich and N-rich conditions, representing a situation where the number of metal atoms exceeded that of N atoms on the growth surface. RHEED patterns during the GaMnN growth, as a function of the Ga/N ratio, recorded along the $[11\bar{2}0]$ projection are shown in Figure 2.12. In a similar fashion to the growth of pure GaN, under Ga-rich conditions, streaks perpendicular to the shadow edge were observed, whilst N-rich

conditions were associated with distinct diffraction spots. Under metal-rich conditions, however, the diffraction spots became distinctly sharper, suggesting a rougher growth surface due to the predominant effect of a high-density Mn atom on the growth surface. EDX assessment of these samples clarified that Mn incorporation occurred only under N-rich or metal-rich conditions. In particular, it was found that the polarity of the films grown under highly metal-rich conditions was transformed from the Ga-polar to N-polar, according to the RHEED observation.

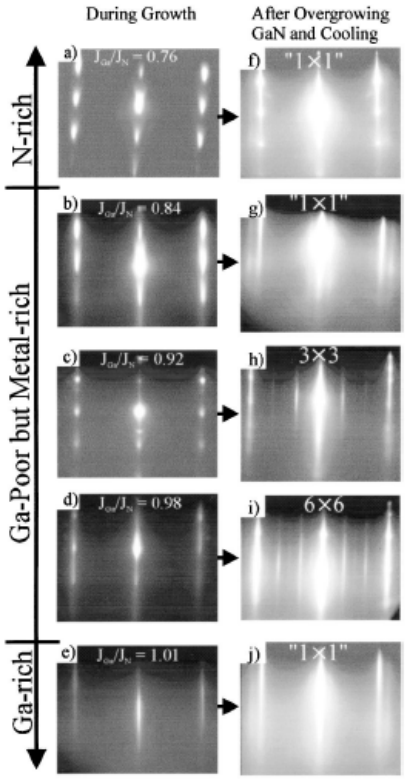

Figure 2.12 (a-e) In-situ RHEED patterns recorded along the $[1\bar{1}20]$ projection obtained during GaMnN/sapphire(0001) growth under different Ga/N ratios. (f-j) In-situ RHEED patterns for each sample obtained after the deposition of a GaN capping layer under Ga-rich conditions [69]

A simple model was given by Haider et al [69,91] regarding Mn incorporation under different growth conditions, with reference to the schematic diagram of Figure 2.13. Briefly, under all conditions, the surface tends to be covered by fast moving Ga atoms, the amount of which is highly dependent on the arrival rate of the incident

species. Under N-rich and metal-rich conditions, Mn atoms have chance to interact with the underlying N atoms, leading to possible Mn occupation of lattice positions. However, under Ga-rich conditions, the Mn atoms are unable to penetrate the Ga surface layers leaving the underlying matrix nearly un-doped.

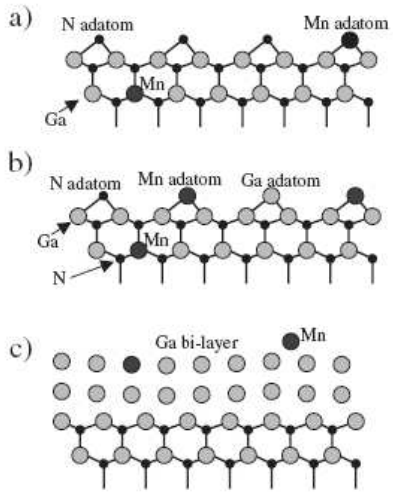

Figure 2.13 Schematic diagram showing possible GaMnN growth mechanisms under (a) N-rich, (b) metal-rich and (c) Ga-rich conditions [100]

Kuroda et al [72,95] reported that the Ga desorption time is significantly decreased by the presence of Mn under slightly Ga-rich conditions. In Figure 2.14, the four regions denoted N, Ga_1, Ga_2 and Ga_D correspond to conditions of N-rich, Ga monolayer coverage, Ga bilayer coverage and the formation of Ga droplets, respectively. It can be seen that the Ga desorption time decreases with increasing Mn flux, indicating that the Ga monolayer and bilayer become less stable due to the presence of Mn. It was also found that Ga bilayers act as a complete barrier hindering Mn incorporation, with the detected Mn concentration being nearly two orders of magnitude lower.

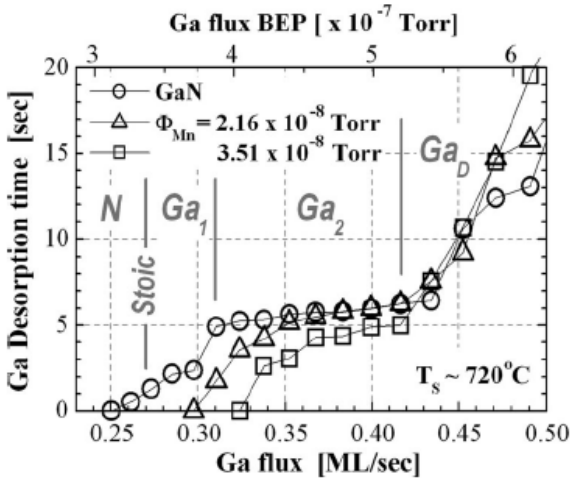

Figure 2.14 Ga desorption time as a function of Ga flux. According to the Ga/N ratio, the growth is divided into four regions, i.e. N, Ga_1, Ga_2 and Ga_D corresponding to conditions of N-rich, Ga monolayer coverage, Ga bilayer coverage and the formation of Ga droplets, respectively [72]

2.4.2.3 Effect of Mn content and growth temperature

During the epitaxy of the GaMnN, a reduced temperature is used to facilitate incorporation of the necessary levels of Mn and to avoid the formation of Mn-rich second phase precipitates. By way of example, epitaxial GaN is normally grown at 700~800 °C [101], whilst GaMnN is typically grown ~100 degrees lower. Ham et al [93] and Soo et al [96] tried very low temperature growth at 350 and 400°C, respectively. Ham et al [93] reported that the saturation magnetization of samples grown at 350°C was the lowest. According to the EXAFS assessment, Soo et al [96] suggested that low temperature growth resulted in the development of more Mn-rich clusters. Based on XRD characterisation, a primitive phase diagram was plotted by Kondo et al [73], as a function of growth temperature and Mn concentration. It was found that high growth temperatures and high Mn concentrations tend to result in phase separation reactions, whilst a limit for single phase growth may be extended to low growth temperatures. A similar consideration was also presented by Chen et al [97].

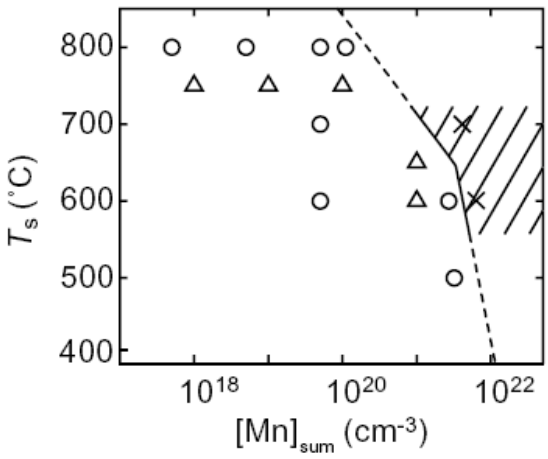

Figure 2.15 Schematic phase diagram under different conditions of substrate temperature (T_s) and Mn concentration ($[Mn]_{sum}$) for GaMnN layers grown by MBE, with circles and triangles representing growth on MOVPE template layers and AlN buffer layers without phase separations, respectively [73]

2.4.2.4 Co-doping of GaMnN using H

Recently, it has been reported that the formation of secondary phases during the growth of GaMnN by MBE is inhibited by the presence of hydrogen [74]. The substrates used for the epitaxial growth of GaMnN using ECR-PAMBE were nitrogen-doped 6H-SiC(0001). A flow of H_2 was added into the plasma to generate active hydrogen species. Samples grown in the presence of H were found to be single phase GaMnN, using XRD and EDX, with Mn concentrations of as high as 6 at%. In parallel, homogeneous GaMnN alloys with Mn concentrations of up to 10 at% have been obtained using reactive MBE [90]. It considered that the growth process is automatically benefited from the decomposition of NH_3 in this case.

2.4.3 Characterisation of GaMnN

The data plotted in Figure 2.3 indicates that there is much room for a further increase in the Curie temperature of p-type magnetic semiconductors. This theoretical report triggered a considerable research effort, leading to experimental reports of a wide

range of Curie temperatures near to or above 300 K, as listed in Table 2.2. However, nearly all the reports to date are based on hexagonal GaMnN exhibiting n-type rather than p-type conductivity. In addition, further experimental work is needed to clarify the role of various Mn-rich precipitates, as evidenced by XRD and TEM and/or suggested by EXAFS or magnetic measurements.

Structural characterisation of GaMnN

In most cases, XRD has been simply used to identify additional phases, noting that the shape and the position of peaks in an XRD spectrum may be changed by defects and strain within the GaMnN layers. A summary of the various Mn-rich precipitates reported (or potential Mn-rich second phases) with corresponding lattice structures and Curie temperatures is presented in Table 2.3. In particular, high resolution triple-axis ω-2θ scans were performed by Dhar et al [76] to investigate the variation in lattice parameter due to the incorporation of increasing levels of Mn for samples grown on 6H-SiC(0001). As plotted in Figure 2.16, the lattice parameter c decreases linearly with increasing Mn content, being considered to be an indication of the substitutional incorporation of Mn. Interestingly, and contrary, Chang et al [70] reported an expansion along the a axis (a=3.1865 Å) for a GaMnN sample with 0.2 at% Mn, obtained from high-order Laue zone (HOLZ) measurements using convergent beam electron diffraction (CBED).

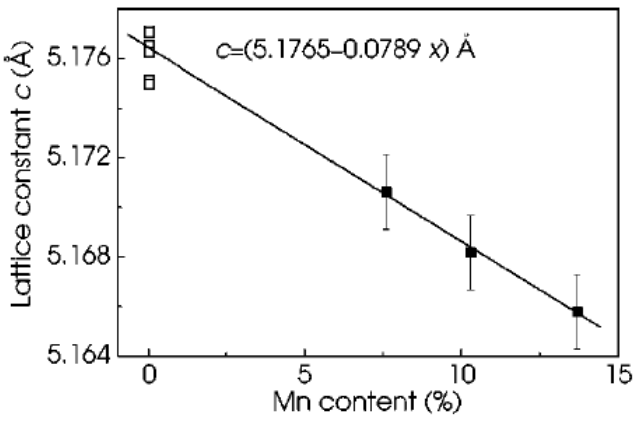

Figure 2.16 Lattice constant c obtained from triple-axis ω-2θ scans versus Mn content, with solid squares representing GaMnN layers and open squares representing pure GaN samples grown on 4H-SiC [76]

Table 2.3 Summary of Mn-rich precipitates (or potential Mn-rich phases) identified within GaMnN and corresponding lattice structures, lattice parameters and Curie temperatures.

Phase	Lattice structure	Lattice parameter (Å)	T_C (K)	Nature of Magnetism	Reference
ς-Mn_5Ga_8 ($Mn_{0.6}Ga_{0.4}$)				ferromagnetic	[17]
$MnGa_{5.2}$	orthorhombic	a=52.99, b=53.81, c=9.94			[102]
MnGa			>740	ferromagnetic	[75]
MnGa				antiferromagnetic	[87]
Mn_8Ga_5	cubic system	a=8.992			[102]
Mn_xGa_{1-x} (x=0.55-0.6)	tetragonal CuAu type	a=2.74, c=3.65 (56 at%) or c=3.69 (59 at%)	400~646	ferromagnetic	[103]
Mn_2Ga				antiferromagnetic	[17]
Mn_3Ga	hexagonal	a=5.404, c=4.357			[102]
ε-Mn_3Ga				ferromagnetic	[17]
Mn_xN_y	tetragonal	a=2.876, c=5.752			[104]
η-Mn_3N_2	face centred tetragonal	a=4.2046, b=12.131		antiferromagnetic	[105]
MnN	distorted NaCl	a=4.16, c=4.24 or a=4.25, b=4.18		antiferromagnetic	[106,107]
Mn_4N				antiferromagnetic	[87]
Mn_4N	cubic	a=3.844			Card no. 3-1193, XRD database
Mn_4N			738	ferrimagnetic	[108]
Mn_4N	perovskite cubic			ferromagnetic	[109]
Mn_3N_2				antiferromagnetic	[80]
θ-Mn_6N_5	hexagonal	a=4.211, c=4.145			[104]
$Mn_6N_{2.58}$				antiferromagnetic	[80]
θ-$Mn_6N_{5.26}$	face centred tetragonal	a=4.2193, c=4.1287		antiferromagnetic	[105]
$GaMn_3N$	prosvkite cubic			antiferromagnetic	[109]

Since Mn-rich compounds are more thermodynamically stable as compared with Mn saturated GaMnN alloys, their nano sized clusters may exist within the GaMnN matrix even under conditions of very low Mn content. This makes for routine identification, using XRD or TEM rather difficult. Alternatively, the local structure around Mn within GaMnN has been studied using the extended X-ray absorption fine structure (EXAFS) [71,96,110] and X-ray absorption near-edge structure (XANES) techniques [111]. Details of these experimental procedures can be found in many review articles, e.g. reference [112]. Soo et al [96] reported that the majority of Mn within their MBE grown GaMnN (Mn concentration ≤ 2at%) are substitutional, occupying Ga sites with an effective valence close to Mn(II), whilst for GaMnN samples prepared by Mn ion implantation, the valence state of Mn is slightly higher at 3^+ [110]. It was reported by Martinez-Criado et al [111] that for low Mn concentrations, the GaMnN films are an homogeneous mixture of Mn^{2+} and Mn^{3+} centres, whilst high Mn concentrations were associated with a strong spatial-dependence of Mn^0 and Mn^{2+} centres, suggesting the possible formation of Mn-rich clusters.

2.4.4 Magnetotransport properties of GaMnN

There has been relatively little investigation of the electrical properties of GaMnN to date with almost all the electrical measurements suggesting n-type conductivity for hexagonal GaMnN. However, the discrepancy in magnetic behaviour of GaMnN prepared using a variety of growth techniques is now recognized [1,2]. Kondo et al [73] and Soo et al [96] stated that hexagonal GaMnN layers grown using MBE exhibited paramagnetic behaviour. In comparison, it was found by Reed et al [82,83] that Curie temperatures for GaMnN samples grown on sapphire, following laser

deposition, are in the range of 220 ~ 370 K, depending on the diffusion conditions. Interestingly, in samples grown on sapphire(0001) using MBE at 720°C, with Mn contents of 6~9 at%, ferromagnetism was reportedly maintained up to 750 K, and even to 940 K, according to an estimation using mean field approximation [87].

A key question is whether these materials are indeed GaMnN alloys or they are a mixture of GaMnN (GaN) and nano-size Mn containing second phases, which are responsible for the detected magnetic properties. Hashimoto et al [75] investigated the relationship between magnetic properties and phase separation within two samples grown by ammonia-source MBE, with Mn concentrations of 12 at% (sample A) and 1.4 at% (sample B), respectively. XRD assessment suggested that sample A was a mixed phase material, whilst sample B was a uniform GaMnN alloy. Figure 2.17 shows the temperature dependence of magnetization for both samples from 7 to 300 K, with the magnetization decreasing rapidly with increasing temperature from 7 to 50 K, and thereafter decreasing very slowly up to 400 K. This is evidence of the existence of two magnetic phases, with Mn-rich compounds being considered to be ferromagnetic and an alloy phase of well defined GaMnN being considered to be paramagnetic, even though XRD examination suggested that sample B contained no second phases.

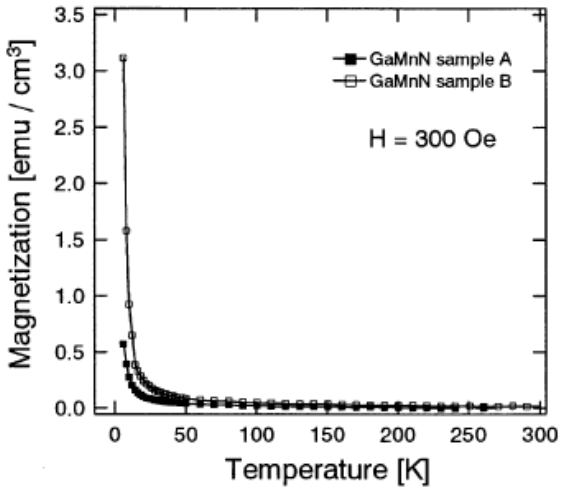

Figure 2.17 Temperature dependence of magnetisation for samples A and B [75]

Indeed, it is considered possible for Mn to form Mn-rich nanoclusters within the GaMnN lattice, even at low concentrations. From a microstructural point of view, such precipitates may be highly commensurate with regard to the GaN matrix, making their identification extremely difficult. From the functional property point of view, they may exhibit a different magnetic behaviour from that of the bulk. Based on first-principle linear combinations of atomic orbitals and molecular orbital theory, Nayak and Jena [113] found that Mn clusters containing up to 5 atoms are still magnetic. Based on density-functional theory, Rao and Jena [114] stated that the stability and magnetic properties of small Mn clusters can be fundamentally altered by the presence of nitrogen and that the wide range of Curie temperatures reported may be closely connected with the development of Mn_xN clusters.

In addition to the initial prediction reported by Dietl et al [3], further theoretical work has been carried out for the purpose of interpreting the various ferromagnetic behaviours of GaMnN observed [115-118]. It is considered that a GaMnN sample may cover all the possibilities, from single phase GaMnN alloy to Mn-containing

nanoclusters and precipitates. Therefore, a single model may not be sufficient and it may be necessary to decide on a case-by-case basis which mechanism is most suitable [1].

2.5 Summary

The growth of GaMnN using MBE over MOCVD, has the advantage that this technology can provide non-equilibrium growth conditions which are considered beneficial for the incorporation of high concentrations of Mn into the GaN. However, a number of Mn-rich second phase precipitates have been identified using XRD and/or TEM. The wide range of observed Curie temperatures is considered to be associated with such precipitates, even though in some cases, they are not even detectable. This requires further experimental and theoretical work in order to obtain the fundamental understanding of the origin of ferromagnetism within DMS materials.

Appendix to Chapter Two

It is worth emphasizing that a novel method using conventional TEM two-beam dark-field imaging for the direct determination of the local concentrations of interstitial and substitutional Mn atoms and As antisites has been developed by Glas et al [119]. Accordingly, within the GaAs lattice, besides the As antisites, there are two types of interstitial sites for Mn, as illustrated in Figure 2.18a. The structure factor F_g for a reflection is given by

$$F_g = 4\{c^V_{As} f_{As} + e^{i\varphi}[c^{III}_{Ga} f_{Ga} + c^{III}_{As} f_{As} + c^S_{Mn} f_{Mn}] + e^{i\varphi} c^1_{Mn} f_{Mn} + c^2_{Mn} f_{Mn}\} \quad \text{Equation 2.1}$$

where f_A is the corresponding atomic scattering amplitude; c^σ_A is the concentration of matrix atoms on matrix sites (III or V); c^S_{Mn}, c^1_{Mn} and c^2_{Mn} are concentrations of Mn atoms occupying substitutional and the two types of interstitial sites; and $\varphi = 2\pi g \cdot \vec{R}$ (where $\vec{R}$ is the atomic position vector). If the small difference in the atomic scattering factor between Ga and As and the contributions of the substitutional Mn and As antisites to the structure factor are eliminated, Equation 2.1 becomes

$$F_{002}(GaMnAs) / F_{002}(GaAs) \approx 1 + 8.38(c^1_{Mn} - c^2_{Mn}) \quad \text{Equation 2.2}$$

Interestingly, with reference to the 002 dark-field intensity of Figure 2.18b, it is inferred that from this equation that type 2 interstitials are the more common type of Mn interstitials within the GaMnAs lattice.

Indeed, TEM is usually unable to detect a concentration of minor non-matrix constituents and this experimental approach provides a novel TEM application.

However, this is not the general case, being restricted by the atomic scattering factors of each individual atom in the sample, also being dependent on the precise setup of the imaging conditions, and significantly affected by the quality of the TEM sample foil.

(a)

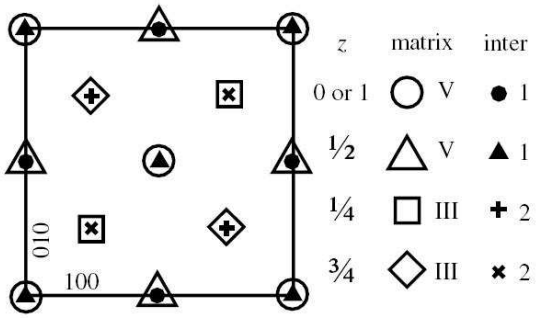

(b)

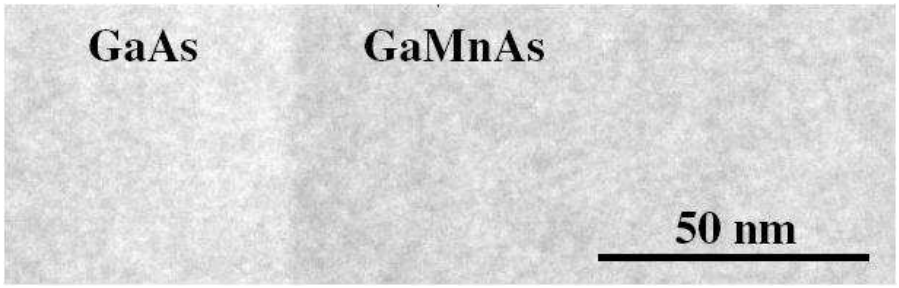

Figure 2.18 (a) The [001] projection of a GaAs unit cell with corresponding lattice positions labelled III, V, 1 and 2, representing the Ga and As matrix sites, and the type 1 and type 2 interstitial sites, respectively. (b) TEM 002 dark-field image of a GaMnAs layer grown on a GaAs substrate, demonstrating contrast due to the incorporation of Mn into the GaAs lattice [119].

CHAPTER THREE

Experimental techniques

3.1 Introduction

The main aim of this chapter is to provide a generalized introduction to the growth and characterisation techniques used in this work. The basic concepts of molecular beam epitaxy (MBE) and growth details of the GaMnN/GaAs(001) samples using plasma-assisted MBE (PAMBE) are presented first. A number of microstructural characterisation techniques, such as X-ray diffraction (XRD), transmission electron microscopy (TEM), selected area electron diffraction (SAED), convergent beam electron diffraction (CBED), energy dispersive X-ray (EDX) analysis and electron energy loss spectrometry (EELS), with associated background knowledge, are then presented. The procedure of preparing cross-sectional and plan-view TEM specimens is briefly described. In addition, the procedure for the absolute polarity determination of GaMnN/GaAs(001) samples is given in section 3.3.2.4.

3.2 Growth of GaMnN/GaAs(001) by molecular beam epitaxy

The epitaxial growth process involves the deposition of a single crystal material on the surface of a single crystal material, with one particular plane of the epitaxial film being parallel to some crystallographic directions in the contact plane of the substrate [60]. If the deposited material is the same as the substrate, the process is termed homoepitaxy, whilst being difference is termed heteroepitaxy. The techniques for

semiconductor epitaxial growth can be divided into three categories according to the medium involved for the transportation of atoms to the growing surface, i.e. vapour-phase epitaxy (VPE), liquid-phase epitaxy (LPE) and solid-phase epitaxy (SPE). Molecular beam epitaxy (MBE) is an ultra-high-vacuum (UHV)-based technique for the growth of high quality epitaxial structures of metals, insulators and semiconductors. Low growth rate and low substrate temperature make it particularly useful for producing abrupt interfaces and doping profiles with atomic precision [60]. In this work, plasma assisted MBE (PAMBE) is employed to provide non-equilibrium growth conditions for the purpose of incorporating high levels of Mn into GaN.

3.2.1 Basis of molecular beam epitaxy

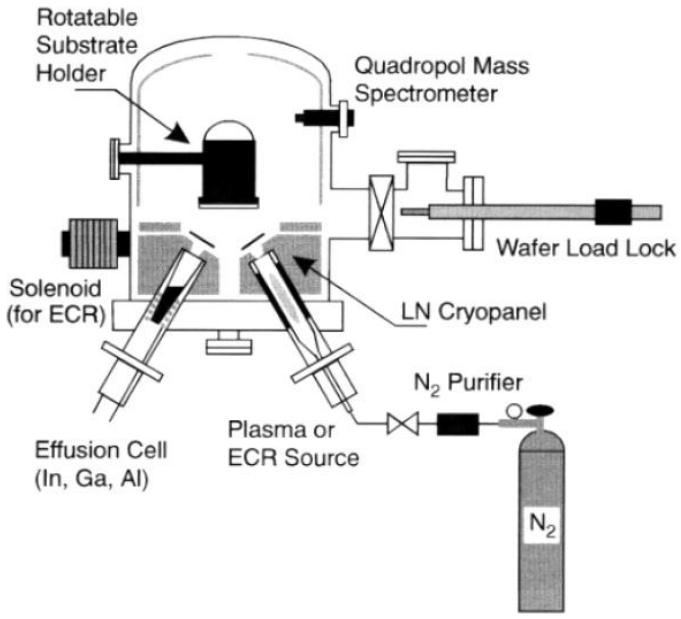

Figure 3.1 Schematic diagram of a molecular beam epitaxy chamber [120]

A schematic diagram of an MBE growth chamber is shown in Figure 3.1. The substrate is mounted on a sample stage capable of azimuthal rotation. The vacuum of the stainless steel growth chamber is at a level of about 1.33×10^{-10} Torr. Liquid

nitrogen cooled surfaces are used to reduce any contamination in the atmospheric environment by absorbing water and other organic substances. Elements within effusion cells are heated and evaporated directly onto the hot substrate surface and become incorporated into the growing thin film. The molecular beam flux is controlled accurately by the effusion cell temperatures and may be monitored by means of a mass spectrometer. For the growth of III-V nitrides, activated nitrogen or nitrogen containing molecules are provided by means of modified MBE techniques, such as plasma-assisted MBE, reactive-ion MBE or reactive MBE. One of the most useful tools for in-situ monitoring of the growth process is RHEED, with an electron beam accelerated to 10~20 kV, being deflected at glancing angles of 0.5 to 2 degrees. This technique can be used to calibrate growth rates, provide information of surface constructions and growth modes and monitor the near surface sample morphology [60,121].

3.2.2 Growth of GaMnN/GaAs(001) by PAMBE

In order to investigate the influence of growth parameters on the development of GaMnN microstructures and associated functional properties, a series of samples were prepared with varying Ga/N ratio, growth temperature and Mn flux. Details of the growth regarding the variation of these parameters are repeated in the experimental sections of Chapters Four, Five and Six, as appropriate.

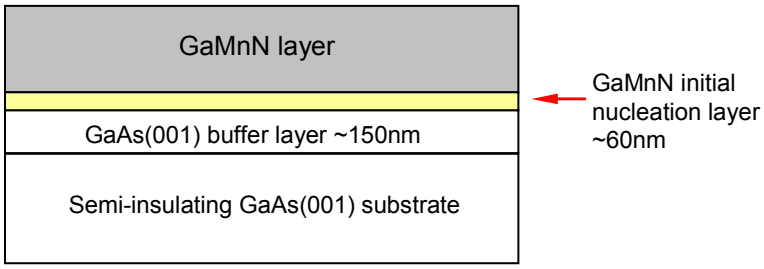

Figure 3.2 Schematic diagram of a GaMnN/GaAs(001) sample viewed in cross section.

Generally, GaMnN epilayers were grown on semi-insulating (001) oriented GaAs substrates at 680°C by PAMBE. In each case, the GaAs substrate was heat treated at ~600°C under As flux for 10 minutes to remove the protective oxide layer and a GaAs buffer layer of thickness ~150 nm was deposited to provide a clean surface for epitaxy. Following initiation of the N plasma, the Mn and N shutters were opened whilst the As shutter was closed. An overall chamber pressure of $2\text{-}3\times10^{-5}$ mbar was maintained by a flow of N_2. Activated nitrogen was supplied using an Oxford Applied Research RF plasma source operated at 450 W and gallium and manganese were produced from single-zone purpose made effusion cells. The substrate temperature was then ramped up to 680°C for the growth of an initial nucleation layer of ~60 nm under slightly N-rich conditions with the beam equivalent pressure (BEP) for Ga being 2×10^{-7} mbar and the BEP for Mn being $8.25\sim10\times10^{-9}$ mbar. The presence of trace levels of As in the chamber [50] and N-rich growth conditions [49,54,64] were found to be beneficial for the nucleation of zinc-blende GaN. The Ga-flux, Mn-flux and growth temperature are then subject to changes for the purpose of the growth of GaMnN layers under a variety of growth conditions.

Table 3.1 Details of the growth of GaMnN layers on GaAs(001) substrates investigated in this work.

Sample	Tg / °C	Ga flux / $\times 10^{-7}$ mbar	Mn flux / $\times 10^{-9}$ mbar	N_2 / $\times 10^{-5}$ mbar	Ga/N ratio	Mn concentration / at% (EDX)
GN1	680	0.75	10	2-3	N-rich	~3.3
GN2	680	1.5	10	2-3	N-rich	-
GN3	680	2.5	10	2-3	N-rich	-
GN4	680	4.6	10	2-3	~1:1 (slightly N-rich)	~4.0
GN5	680	8.0	10	2-3	Ga-rich	0
GN6	680	10	10	2-3	Ga-rich	0
GN7	680	12	10	2-3	Ga-rich	0
M0	680	2	0	2-3	N-rich	0
M1	680	2	0.495	2-3	N-rich	-
M2	680	2	1.65	2-3	N-rich	-
M3	680	2	4.95	2-3	N-rich	-
M4	680	2	25	2-3	N-rich	~5
N680	680	2	10	2-3	N-rich	~1.8 (estimated by MBE)
N597	597	2	10	2-3	N-rich	-
N443	443	2	10	2-3	N-rich	~5.0
N265	265	2	10	2-3	N-rich	-
N186	186	2	10	2-3	N-rich	-
G680	680	6.6	10	2-3	Ga-rich	-
G507	507	6.6	10	2-3	Ga-rich	-
G340	340	6.6	10	2-3	Ga-rich	~0.7-2.0
G265	265	6.6	10	2-3	Ga-rich	~2.5-4.5
G186	186	6.6	10	2-3	Ga-rich	-

3.3 Characterisation of GaMnN/GaAs(001)

The main aim of this section is to provide a generalised introduction to the techniques used in this work for the characterisation of GaMnN/GaAs(001) samples. Thus, it is appropriate to consider these techniques in terms of structural, imaging and chemical analyses, respectively. X-ray diffraction and electron diffraction provide the structural information of a material, whilst TEM and SEM allow direct observation of a sample at high magnification. In parallel, the inelastically scatters waves, such as inelastically scattered high-energy electrons, allow the fine-scale chemical microanalysis of a sample performed in the SEM and/or TEM using techniques of EDX, EELS and EFTEM.

3.3.1 X-ray diffraction

X-ray diffraction is commonly used for the assessment of semiconductor microstructure. The basic principles associated with diffraction are presented here with reference to X-ray scattering and interference.

In XRD, an X-ray wave may be described as an electromagnetic field which induces the electronic cloud in an atom, rather than the nuclei, to oscillate and emit an electromagnetic wave, being coherent with the incident X-ray wave. This process is known as Rayleigh scattering. Laue's approach envisages crystals as a three-dimensional network of atoms leading to a three-dimensional diffraction grating. Alternatively, Bragg's law provides a simpler description of the diffraction process, as shown in Figure 3.3. The condition for constructive interference is satisfied when the difference in path length between the incident and scattered waves is equal to a whole number (n) of wavelengths. That is:

$$n\lambda = 2d\sin\theta \qquad \text{Equation 3.1}$$

where d is the lattice spacing, λ is the X-ray wavelength and θ is the diffraction angle [122-124].

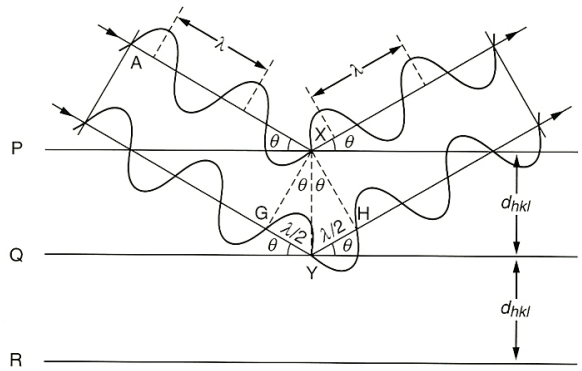

Figure 3.3 Bragg's diffraction condition is satisfied when the difference in path length between the incident and scattered waves is equal to a whole number (n) of wavelengths. P, Q and R are three successive lattice planes (hkl) of spacing d_{hkl} in a crystal. The incoming radiation of wavelength λ incident at a glancing angle θ is diffracted at the same angle. Constructive interference is obtained when the Bragg equation is satisfied. [124]

The reciprocal lattice and the Ewald sphere provide a useful model to understand the formation of diffractions patterns. The magnitude of a reciprocal lattice vector is defined as being equal to the reciprocal of the associated crystal plane spacing in real space, with the direction of this reciprocal lattice vector being parallel to the normal to these crystal planes. Thus, each lattice plane in real space has a corresponding reciprocal lattice point in the reciprocal lattice, allowing the transformation of real lattice planes to a 3D construction of reciprocal lattice points. The Ewald sphere can be constructed on the basis of the reciprocal lattice and Bragg's law. As shown in Figure 3.4, spots intercepted by the Ewald sphere, of radius 1/λ, indicate that the corresponding planes satisfy the Bragg condition with, intensity peaks being detected in XRD or diffraction spots projected onto the TEM phosphor screen.

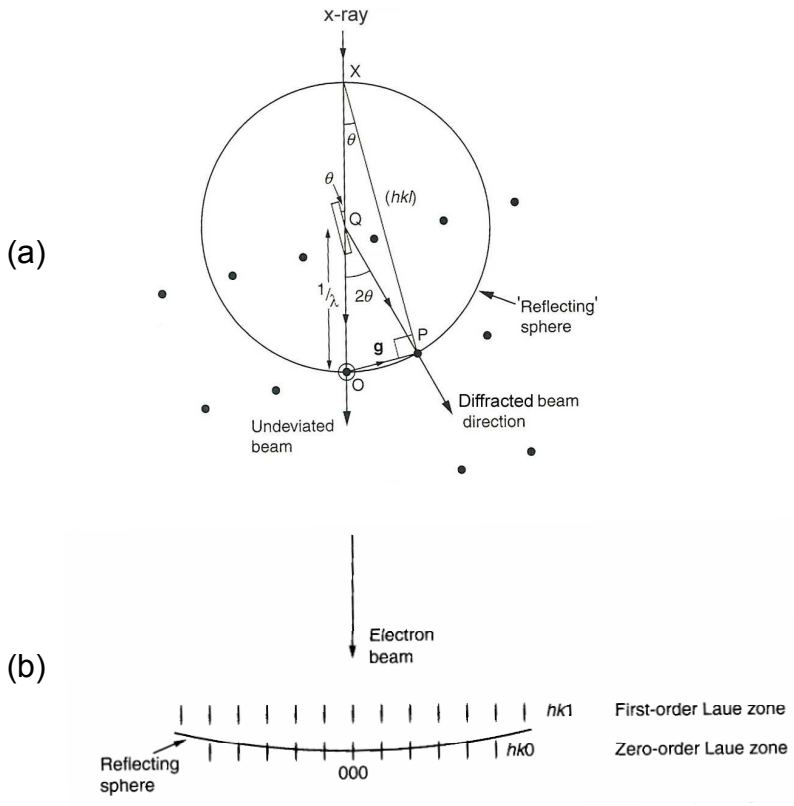

Figure 3.4 (a) Illustration of the construction of the Ewald sphere in XRD. The centre of the Ewald sphere is at a distance of 1/λ from the origin of reciprocal space along the line of the incident X-ray (or electron beam). In this case, reciprocal lattice spot P is intercepted by the sphere where the Bragg condition is satisfied. (b) In electron diffraction, the diameter of the Ewald sphere becomes very large due to the much shorter wavelength of high-energy electrons, allowing more reciprocal lattice spots to be intersected and projected on the TEM screen, after [124].

Since the Laue equations and Bragg's law were derived only on the basis of the diffraction geometry, it is also necessary to consider the scattering ability of every single atom in a crystal to predict the intensity of diffracted beams. The structure factor, F_{hkl}, corresponding to the amplitude of constructive interference is a simple summation of the atomic scattering factors (f_n) of all atoms (N) in a unit cell. Where h, k and l are the indices of a particular lattice plane at the Bragg conditions, while (u_n,v_n,w_n) is the position vector of an atom within the unit cell. [122-124]

$$F_{hkl} = \sum_{1}^{N} f_n \exp 2\pi i(hu_n + kv_n + lw_n) \qquad \text{Equation 3.2}$$

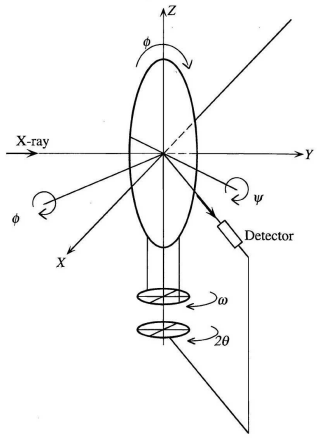

Figure 3.5 Schematic representation of a four-circle X-ray diffractometer [68]

For single crystal materials or materials with preferred grain orientation, simple powder X-ray diffraction techniques are not sufficient to fully profile the characteristic diffraction conditions. Instead, a four-circle X-ray diffractometer with independent sample rotation axes is required (Figure 3.5). By using such an X-ray diffractometer, pole figures and reciprocal lattice maps giving a complete picture of different structural phases and orientation relationships can be generated. [122]

3.3.2 Electron microscopy

Electron microscopy uses a beam of highly energetic electrons to examine objects on a very fine scale, generating a variety of information on surface morphology, elemental composition, sample crystallography and material functional properties, etc. This section starts with the basic properties of high-energy electrons and the interactions between electrons and matter, and then focuses on transmission electron microscopy (TEM) based characterisation techniques such as diffraction contrast imaging, RHEED, selected area electron diffraction (SAED), EDX, EELS, EFTEM, etc.

3.3.2.1 Interaction of high-energy electrons with matters

According to wave-particle duality, a beam of electrons can be treated as both particles and a wave. According to De Broglie's theory, the wavelength of an electron is given by:

$$\lambda = \frac{h}{(2m_0 eV)^{1/2}} \qquad \text{Equation 3.3}$$

where h is the Planck's constant, e is the electron charge, V is the potential difference though which the electron is accelerated and m_0 is the mass of the electron. In transmission electron microscopy, electrons are normally accelerated to 100~400 keV and the associated relativistic effects cannot be ignored. The wavelength of the electrons is modified by substituting V with $V\left(1+\frac{eV}{2m_0c^2}\right)$ and a more accurate equation is given by:

$$\lambda = \frac{h}{\left\{2m_0 eV\left(1+\frac{eV}{2m_0c^2}\right)\right\}^{1/2}} \qquad \text{Equation 3.4}$$

where c is the velocity of light [125].

As distinct from X-rays, electrons are negatively charged and scattered by both electrons and the nuclei in an atom. Therefore, the interaction between electrons and matter is much stronger than for X-rays and a beam of electrons is easily deflected by an electrostatic or an electromagnetic field. Electrons are considered as waves, e.g. when describing the optics of a TEM experiment and the processes of diffraction, whilst they are considered as particles, e.g. when behave mainly as particles during the course of interaction with a specimen leading to various signals which may be detected and analyzed to obtain sample characteristic information. The signals created

as a consequence of the interaction between a high-energy electron beam and a solid specimen is illustrated in Figure 3.6, with the signal generation mechanisms and corresponding analytical techniques listed in Table 3.2 [125-127]. Briefly, elastically scattered electrons maintain the energy but with a change in direction with respect to the primary electron beam, being mainly used in TEM for the construction of diffraction patterns and diffraction contrast images. Inelastically scattered electrons which lost a certain amount of energy, being characteristic of the sample elemental composition, can be analyzed using the technique of electron energy loss spectroscopy (EELS). In parallel, a variety of second effects may also occur as a result of the scattering of the incident electron beam and can be used as separate characterisation techniques, e.g. secondary electrons (secondary electron imaging), backscattered electrons (backscattered electron imaging), X-rays (energy dispersive X-ray (EDX) spectroscopy and wavelength dispersive X-ray (WDX) spectroscopy), Auger electrons (Auger electron spectroscopy (AES)) and light (Cathodo-luminescence (CL)).

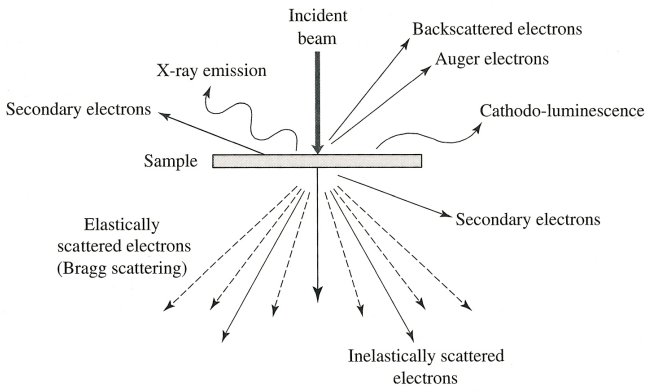

Figure 3.6 Signals generated when a beam of high-energy electrons interacts with a thin specimen [126].

Table 3.2 Signals generated by electron beam - specimen interaction and associated characterisation techniques [125-127]

Signal generated	Production mechanism	Analytical technique
Elastically scattered electrons	Electrons are scattered by outer shell electrons with no energy loss.	Electron diffraction and diffraction contrast imaging
Inelastically scattered electrons	Incident electrons experience energy loss after being scattered by phonons, plasmons and valence and core shell electrons.	Electron energy loss spectrometry (EELS)
Secondary electrons	Electrons within the sample are emitted follwing a variety of mechanisms (low energy of ~50eV)	Secondary electron imaging
Back-scattered electrons	Incident electrons interact strongly with atomic nuclei and undergo large deflections	Back-scattered electron imaging
X-rays	A relaxation process happens due to the displacement of an inner shell electron by an incident high energy electron: an outer shell electron fills the vacancy and an X-ray photon with characteristic energy is emitted.	Energy dispersive X-ray (EDX) spectroscopy and wavelength dispersive X-ray (WDX) spectroscopy
Auger electrons	An alternative relaxation process happens due to the displacement of an inner shell electron by an incident high energy electron: an outer shell electron with characteristic energy is emitted.	Auger electron spectroscopy (AES)
Light (UV, visible, IR)	The place of an ejected valence band electron is filled by a conduction band electron leading to the emission of a photon of light with characteristic energy of the local band gap.	Cathodo-luminescence (CL)

3.3.2.2 Transmission electron microscopy

A microscope allows objects to be images at high magnification with high resolution. The theoretical resolution of a microscope is given by the classical Rayleigh criterion:

$$\delta = \frac{0.61\lambda}{\mu \sin \beta} \qquad \text{Equation 3.5}$$

Where β is the semi-angle of collection of the magnifying lens, μ is the lens refractive index and δ, the resolution represents the smallest separation of points within an object that can be resolved. If there are no aberrations at all for any lens, the resolution of the microscope is only limited by the wavelength (λ) of the incident electromagnetic wave. Since electrons have much smaller wavelength after being accelerated to over 100 keV (λ=0.00375 nm, with relativistic correction) than visible lights (e.g. λ=550 nm for green light), in principle, a TEM offers significant better resolution than an optical microscope. In practice, the ultimate resolution of a TEM is

limited by the aberrations associated with the electron optics. Nowadays, transmission electron microscopy techniques are powerful tools for the study of the microstructure of materials at the atomic level [125,127].

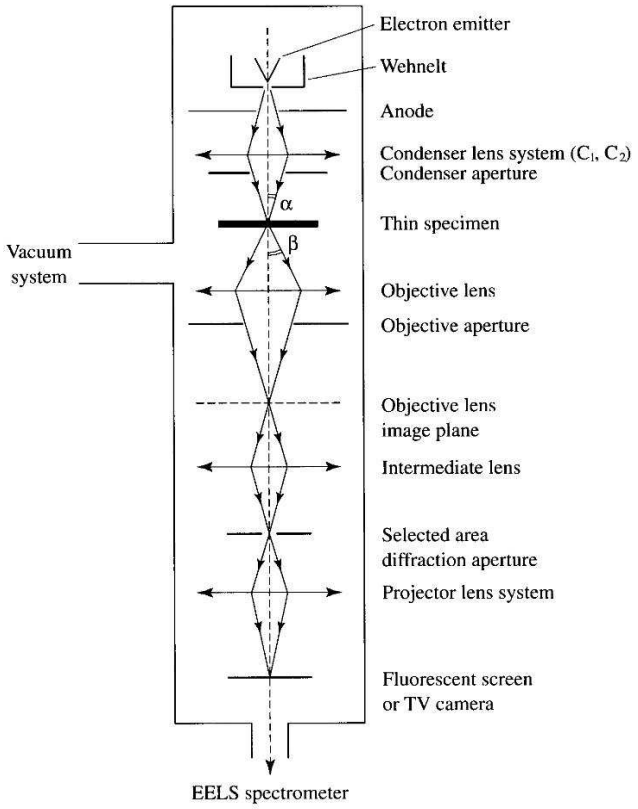

Figure 3.7 Schematic diagram of the basic components of a TEM [126]

A conventional TEM consists of a number of electron-optical components, e.g. as illustrated in Figure 3.7. A stream of electrons may be produced by thermionic emission (W or LaB_6 source) or by field emission (single crystal W) from the filament gun. The electron beam is accelerated towards the anode to achieve the final beam energy, typically between 100 to 400 keV. Generally, the first condenser lens (C1) determines the electron beam spot size and the second condenser lens (C2) is responsible for focusing or spreading the beam across the specimen to provide appropriate illumination conditions. The condenser aperture filters out electrons far

from the optic axis and controls the number of electrons incident at the sample. The sample (thickness<100 nm) is placed close to the front focal plane of the objective lens. Transmitted electrons with large diffraction angle are restricted by the objective aperture located in the back focal plane of the objective lens, thereby enhancing the contrast of the TEM image. In the diffraction mode, the objective aperture is removed and a selected area aperture is inserted into the intermediate image plane, allowing the selection of a much smaller area on the specimen in order to form an electron diffraction pattern. The optics for the formation of images and electron diffraction patterns within a TEM are illustrated in Figure 3.8 [124-126].

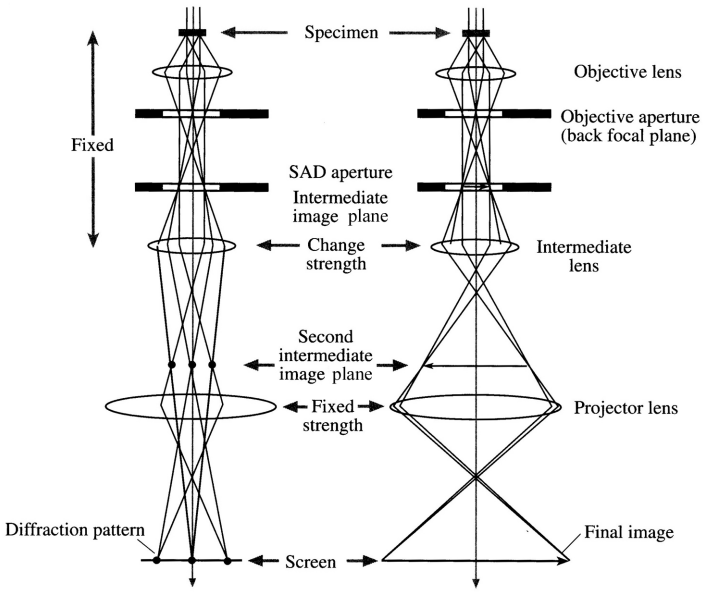

Figure 3.8 Schematic diagram showing the optics for the formation of electron diffraction patterns and images within a TEM, after [125]

As previously mentioned, both XRD and electron diffraction result from the interference of scattered waves and can be interpreted with reference to the same geometrical model of Braggs law. The wavelength of high-energy electrons (e.g. 1.97×10^{-12} m for 300 keV electrons) is much shorter than that of X-rays (about

1×10^{-10} m) and also much smaller than the lattice parameter of crystals (normally in the region of 3×10^{-10} m upwards). In fact, the diffraction pattern projected onto the TEM screen consists of a large number of reflections because (a) the radius of the Ewald sphere ($1/\lambda$) is large in comparison to the reciprocal lattice spacings and (b) the reciprocal lattice nodes are extended perpendicular to the sample surface, due to the thin 2D nature of the sample foil, allowing a large number of reciprocal lattice points close to the surface of the reflecting sphere to be intersected by the Ewald sphere (Figure 3.4b). The manipulation of the sample orientation can be easily achieved by tilting the sample while observing changes of the electron diffraction pattern. Also, diffraction patterns can be obtained from very small sample regions selected either with a diffraction aperture (selected area electron diffraction) or by a focused electron beam of nm-size (convergent beam electron diffraction) [123,124].

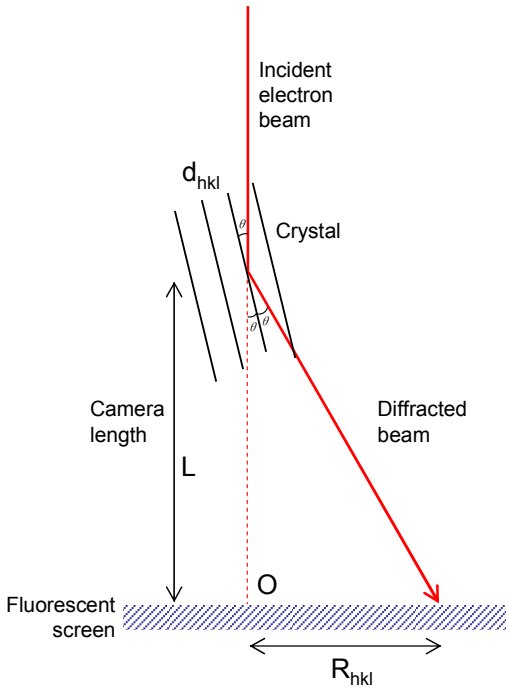

Figure 3.9 Schematic diagram showing the formation of reflection electron diffraction patterns. L is the camera length and R_{hkl} is the distance between the central spot and the diffraction spot.

In view of the small diffraction angle (<3°) and the large radius of the Ewald sphere, the Bragg's equation can be simplified (since sinθ ≈ θ for small θ (in radians)):

$$\lambda = 2d_{hkl}\theta \qquad \text{Equation 3.6}$$

From Figure 3.9, the following equation is also obtained:

$$\tan 2\theta = \frac{R_{hkl}}{L} \approx 2\theta = \frac{R_{hkl}}{L} \qquad \text{Equation 3.7}$$

where R_{hkl} is the distance between a diffracted spot and the directly transmitted electron beam. Combining these two equations we have:

$$\lambda L = R_{hkl}d_{hkl} \qquad \text{Equation 3.8}$$

λL is called the camera constant and can be obtained using a standard material of known lattice parameters. By using this equation, an unknown material then may be identified though the indexing of relevant electron diffraction spots [123,124].

TEM images can be formed by inserting an objective aperture into the back focal plane of the objective lens, selecting electrons diffracted in a particular direction. If the central spot (contains the directly transmitted electrons and some scattered electrons) is used, a bright field image is formed. Alternatively, a dark field image may be formed by aligning a diffracted beam down the optic axis of the microscope (centred dark field imaging), or moving the objective aperture to just cover the associated diffraction spot(s). In addition, the sample may be tilted in order to make the reciprocal spots of a specific set of planes intercepted by the Ewald sphere, leading to the establishment of a two-beam condition, evidenced by the presence of only one strongly excited diffraction spot on the TEM screen (of course the central spot is the other strong spot). Then, two beam dark field images may be obtained using this diffraction spot for the purpose of highlighting features which are not generally shown on normal bright field or dark field images [125]. By way of an

example, Figure 3.10 shows the difference in the contrast obtained from a cross-sectional wurtzite GaN sample grown on SiC(0001) under bright field and two-beam dark-field diffraction conditions, respectively. A high density of pure edge and mixed (edge/screw) dislocations become apparent in Figure 3.10b, obtained using the $[0\bar{1}10]$ diffraction vector.

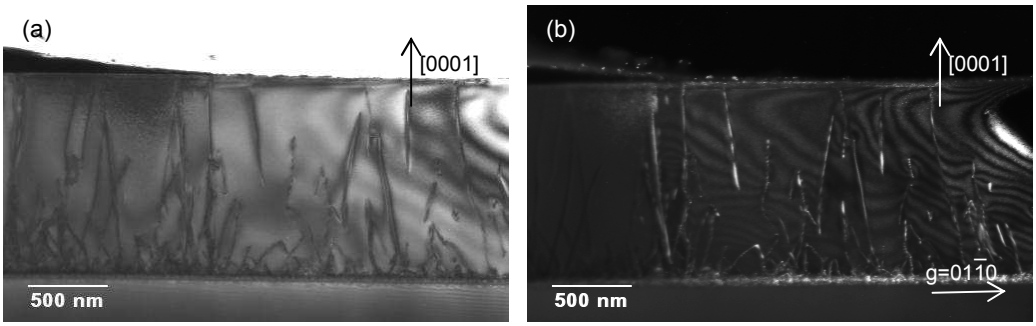

Figure 3.10 (a) Bright field image taken along the $[2\bar{1}\bar{1}0]$ projection and (b) two-beam dark-field image using the $[0\bar{1}10]$ diffraction vector of a cross-sectional wurtzite GaN grown on SiC(0001).

Further, crystal structure can also be investigated by high resolution transmission electron microscopy (HRTEM or HREM), capable of showing the positions of atoms with images being formed due to differences in the phase of electron waves scattered by a thin sample. Most modern TEMs also provide a scanning transmission mode (STEM). Electrons are focused into a very narrow probe which is scanned across the specimen with the collection angle being varied by the projector lenses. The rastering of the electron beam across the sample makes the scanning mode particularly suitable for obtaining elemental maps from EDX and EELS [60,125].

The electron microscopy in most of this work was carried out using two machines. A Jeol 2000fx TEM/STEM with a LaB_6 filament operating at 200 kV was employed for

lower magnification imaging and energy-dispersive X-ray analysis, while a Jeol 4000fx equipped with a Gatan Imaging Filter (GIF) and a tungsten or LaB_6 filament was used for high resolution TEM, EELS and energy filtered TEM (EFTEM). Part of the work was carried out using the Jeol JEM2010F equipped with a GIF at the University of Sheffield.

3.3.2.3 Reflection high-energy electron diffraction (RHEED) within TEM

The RHEED technique within a TEM may be used for the rapid structural assessment of the near surface microstructure of materials, e.g. providing an initial quick appraisal of the structure of deposited layers. The process of twist, tilt and translation of the stage along three axes enables any zone axis within the surface plane of the sample to be accessed. During RHEED, the incident electron beam, with glancing angle of less than 1°, samples a surface area of ~1mm^2, but the diffraction process is sensitive to just the top few atomic layers.

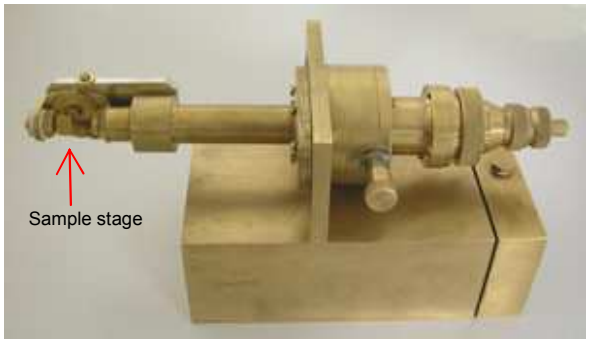

Figure 3.11 Photograph of the RHEED stage for the Jeol 2000fx

In this work, samples were assessed using a RHEED stage (Figure 3.11) mounted immediately beneath the projector lens of a Jeol 2000fx operated at 200kV to provide an overview of the microstructure of all the GaMnN/GaAs(001) samples grown by

PAMBE. Then, samples of specific interest were subsequently prepared for TEM and appraised to obtain a more detailed insight into the dynamic evolution of the epilayer microstructure.

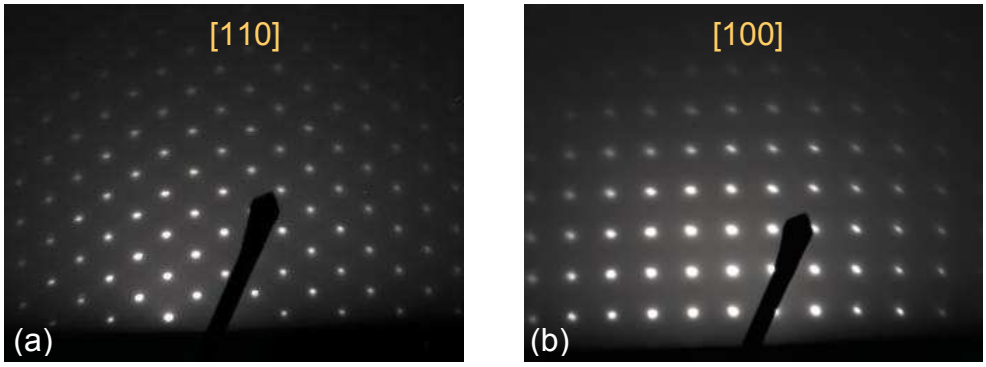

Figure 3.12 Representative RHEED patterns of a zinc-blende GaMnN/GaAs sample recorded along (a) the [110] and (b) the [100] projections, respectively.

3.3.2.4 Convergent-beam electron diffraction (CBED)

In SAED, for periodic samples, the parallel incident electron beam produces an array of sharp spots at the back focal plane of the objective lens. The smallest area from which the diffraction process can be appraised is limited by the size of the selected area aperture (~0.5-0.1 μm). Since many crystal features such as second-phase precipitates are much smaller than the selected area aperture, it sometimes becomes convenient to obtain diffraction information directly, using convergent-beam electron diffraction (CBED). The CBED technique uses a conical electron beam with an angle of convergence, 2α, controlled by the size of the condenser aperture with the electron beam probe on the sample focused down to ~10 nm. In addition to the improved spacial resolution, CBED patterns can also provide additional, useful information about a material, such as specimen thickness, unit cell and precise lattice parameters, the crystal system and true 3D crystal symmetry [124,125].

Polarity determination of zinc-blende GaMnN/GaAs(001) by CBED

As will be shown later, the microstructure of zinc-blende GaMnN/GaAs(001) is highly faulted with stacking faults and microtwins on {111} planes inclined to the advancing growth surface, which makes it very difficult to obtain polarity information directly from the epilayer using CBED. Instead, in this work, the assessment of sample polarity was performed on the GaAs substrate, presuming that the sample polarity of the GaAs is retained across the GaMnN/GaAs(001) interface into the epilayer [61-65].

The absolute polarity of GaAs [128,129] and CdTe [130] has been determined successfully using convergent beam electron diffraction (sometimes termed microdiffraction). For most cases of electron diffraction, there is no difference in the intensities of beams scattered by {hkl} and $\{\bar{h}\bar{k}\bar{l}\}$ planes, known as the Friedel's law. In order to break this indeterminacy, samples are tilted away, about 10° or more, from the <110> zone axis and the Bragg conditions for {200} and odd indices {911} and {11,1,1} reflections are satisfied. The scattering from the two high order, odd indices interferes constructively or destructively through the {200} disk with bright or dark crosses being observed. A bright cross always corresponds to the sense of advancing $\{\bar{1}\bar{1}\bar{1}\}B$ planes whereas a dark cross corresponds to advancing {111}A planes [128,129] and CdTe [130]. A simple interpretation based on the structure factor of the GaAs unit cell was given by Taftø and Spence [128]. A more detailed model using the dynamical diffraction theory was given by Ishizuka [131] and is presented briefly in the appendix to this chapter.

Correlating polarity information from in situ RHEED within MBE and CBED in TEM

The Jeol 2000fx microscope was calibrated previously using CBED of a CdTe/GaAs $\{\bar{1}\bar{1}\bar{1}\}B$ sample with known polarity, demonstrating a rotation of 180° between the TEM image and the diffraction pattern for this particular microscope. A test was performed to ensure that the sample polarity, as assessed using in-situ RHEED during GaN/GaAs(001) growth, was the same as that determined independently using CBED in the TEM, so that clear distinction could be made between orthogonal [110] and $[1\bar{1}0]$ sample projections during analysis. Zinc-blende GaN calibration check samples on (001) oriented GaAs grown under N-rich conditions were grown. An As-rich condition was used to initiate the GaN epitaxial growth. Sharp RHEED patterns appeared first demonstrating the formation of a GaAs nucleation layer which soon disappeared due to the nucleation of the GaN layer. The <110> directions within the growth surface were labelled according to the RHEED information, being 2× reconstruction corresponding to [110] projection and 4× corresponding to $[1\bar{1}0]$ projection [132]. Cross-sectional TEM specimens were made with two pieces of this calibration sample glued face to face along the same [110] projection, which was carefully noted to avoid any confusion throughout the whole preparation process. A representative many-beam bright field image along the [110] projection is shown in Figure 3.13a. By tilting this sample away about 10° from this [110] projection, the Bragg condition satisfying the 002, $\bar{1}1\bar{9}$ and $\bar{1}$,1,11 diffraction conditions was established. After slightly converging the TEM illumination, bright crosses for both sides towards the growth direction was obtained (Figure 3.13a inset and Figure 3.13b), confirming the absolute [110] sample projection, being consistent with the polarity results obtained from in-situ RHEED in MBE.

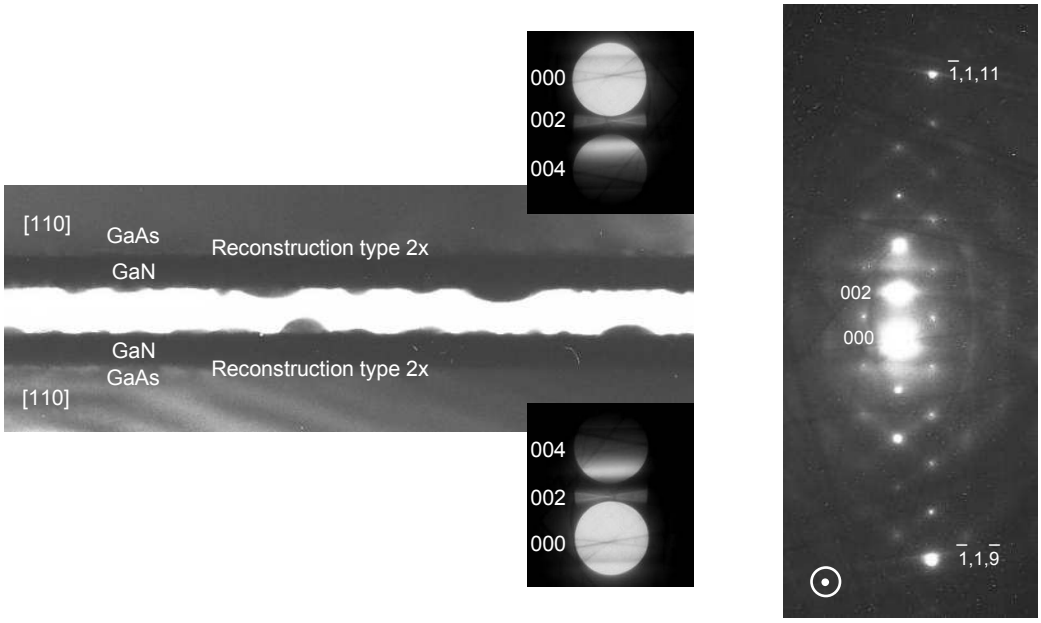

Figure 3.13 (a) Many-beam bright-field image of a GaN/GaAs calibration sample with two pieces glued along the same [110] projection. Bright crosses through 002 diffraction disc for both sides, towards the growth direction, were obtained confirming the consistency in the polarity results obtained from in-situ RHEED in MBE and CBED. (b) Representative diffraction pattern showing the precise Bragg condition satisfying 002, $\bar{1}1\bar{9}$ and $\bar{1}$,1,11 after tilting the sample away about 10° from the [110] projection[2].

3.3.2.5 Scanning electron microscopy (SEM)

In scanning electron microscopy, the electrons are accelerated through a potential difference typically of the order of 10-30 keV and the spot size formed by the magnetic lenses is of the order of a few nm. When the accelerated electrons hit the sample surface, secondary electrons, backscattered electrons and X-rays are emitted and detected to produce, respectively, secondary electron (SE) image, backscattered electron (BS) images and energy dispersive X-rays (EDX) spectra for the purpose of elemental analysis. [127]

[2] In this work, the absolute polarity of each sample was obtained using CBED performed on the GaAs substrate. Therefore, a representative CBED pattern is used in each case, demonstrating the establishment of diffraction conditions with bright cross or dark cross corresponding to the advancing B or A planes, respectively.

3.3.3 Analytical techniques

3.3.3.1 Energy dispersive X-ray (EDX) spectrometry

Electron dispersive X-ray spectrometry is a standard method for identifying and qualifying the elements within a sample. A characteristic X-ray is emitted when an outer shell electron fills the vacancy of an inner shell electron ejected by the incident high-energy electron beam. The relationship between the atomic number and energy of an emission line for a given X-ray is given by Moseley's Law [133],

$$\sqrt{E} = C_1(Z - C_2) \qquad \text{Equation 3.9}$$

where E is the energy of the emission line for a given X-ray series (e.g. K_α or K_β, etc.), Z is the atomic number and C_1, C_2 are constants. Since the generation of X-rays is a function of the atomic number, EDX analysis is ideally suited for the chemical analysis of heavier elements (Z>11).

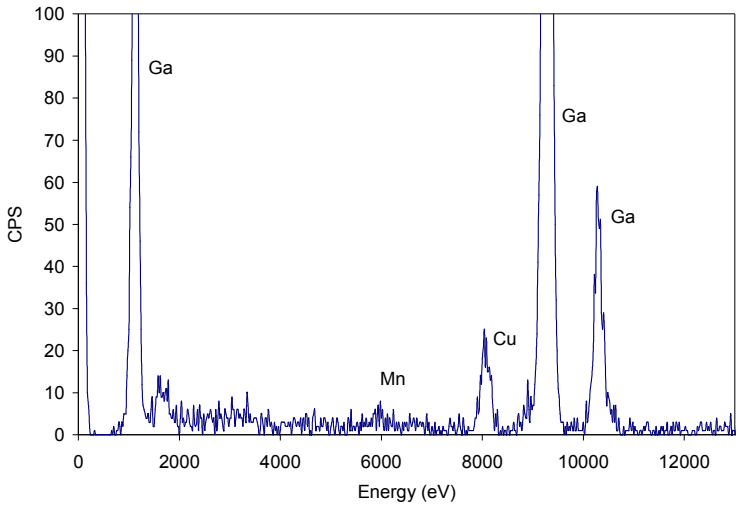

Figure 3.14 EDX spectrum obtained on a GaMnN layer grown on GaAs(001)

In this work, EDX point and line scan analyses were carried out using an Oxford Link Isis package on a Jeol 2000fx TEM/STEM operated at 200 kV. This provided semi-

quantitative elemental composition of TEM specimens. Samples were tilted slightly to avoid strong diffraction axes, but with the GaMnN GaAs interface roughly parallel to the electron beam. An acquisition time of 50 s was used to obtain sufficient counts without significant sample drift. During the EDX point analysis, a small point size sufficiently small to allow the electron beam to be focused on ~40nm features, such as MnAs inclusions, was used.

Table 3.3 Characteristic X-ray energies (keV) for elements of N, Mn, Ga, As and Cu, respectively, with corresponding edges used for identifying and quantifying each elements highlighted [134]

Z	Element	M_α	M_β	M_γ	$L_{\alpha1}$	$L_{\beta1}$	$L_{\beta2}$	$K_{\alpha2}$	$K_{\alpha1}$	$K_{\beta1}$
7	N							0.392		
25	Mn				0.637	0.649		5.887	5.898	6.489
29	Cu				0.930	0.950		8.026	8.046	8.904
31	Ga				1.098	1.125		9.223	9.250	10.263
33	As				1.282	1.317		10.506	10.542	11.724

3.3.3.2 Electron energy-loss spectrometry (EELS) and energy filtered TEM (EFTEM)[3]

During the interaction of an electron beam with a sample, some electrons within the electron beam will undergo inelastic scattering, resulting in both a loss of energy and a change in momentum. The energy transferred in such interactions due to the inner shell ionization is characteristic of the elements in the sample and can be detected by the post column spectrometer, attached under the electron microscope. When the electron beam emerging from the sample is passed through a magnetic prism, the flight path of the electrons will vary depending on their energy. This principle is used to form spectra in EELS. It is also possible to place an adjustable slit to allow only electrons with a certain range of energies through and to reform an image using just these electrons on a detector. This technique is known as EFTEM [125,126].

[3] The EELS and EFTEM were carried out by Dr Mike Fay, part of which was performed at the University of Sheffield.

The major features of EEL spectrum, as seen in Figure 3.15, are the zero loss peak, the plasmon peak, and the elemental edges. The zero-loss peak is formed by electrons that have been elastically scattered and quasi-elastically scattered by the specimen. The low loss region (0-50eV) is mainly a reflection of interactions with plasmons which are the collective, resonant oscillations of valence electrons in a solid. This region may be used to calculate the thickness of a sample. At the high loss region (>40eV), an energy loss signature due to the excitation of inner shell electrons being characteristic to the atomic number is called an ionization edge. [126]

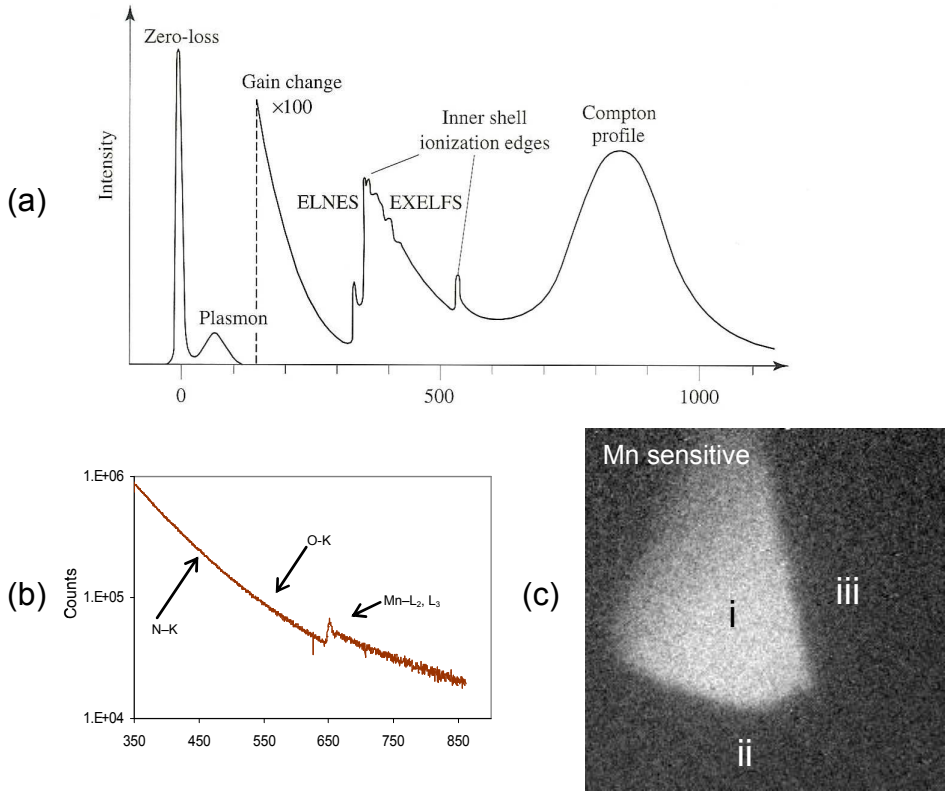

Figure 3.15 (a) Schematic diagram of an EEL spectrum on a linear scale [126]. (b) An EEL spectrum obtained on a GaMnN sample with a peak for the Mn-edges, indicating the incorporation of Mn within GaMnN. (c) Mn sensitive image taken from the GaMnN/GaAs interface in a region with an MnAs inclusion. Regions in (c) are (i) MnAs inclusion, (ii) GaAs substrate and (iii) GaMnN.

In EFTEM, a series of images are recorded across several hundred eV loss where a number of chemical species are involved, allowing quantitative analysis and reliable

accuracy of mapping, also allowing EELS spectra to be extracted from particular features.

3.3.4 Measurements of electrotransport properties of GaMnN

Four-point electrical measurements were performed using Ti/Al/Au ohmic contacts in the corners of ~3×3 mm sample squares, with the contacts annealed at 440 ºC for five minutes. Standard low frequency AC lock-in methods were used for the measurements, with excitation currents typically in the range 100nA – 1μA. Magnetic measurements were performed in a superconducting quantum interference devices (SQUID) magnetometer, with magnetic fields of up to 4000 Oe applied in the plane of the sample[4].

3.4 TEM specimen preparation

The microstructure of the GaMnN/GaAs(001) samples and the integrity of the epilayer/substrate interface were investigated using TEM techniques. Considering the high hardness of GaN, the brittle nature of III-V semiconductors and the difference in hardness between the GaMnN layer and GaAs substrate, preparation of sample foils (<1μm) suitable for TEM examination proved to be somewhat difficult. Great care and patience are required to minimize the artifacts introduced during the preparation process.

[4] The measurement of transport and magnetic properties of the GaMnN/GaAs(001) samples were performed in the School of Physics and Astronomy of The University of Nottingham and the Institute of Physics of Polish Academy of Sciences, respectively.

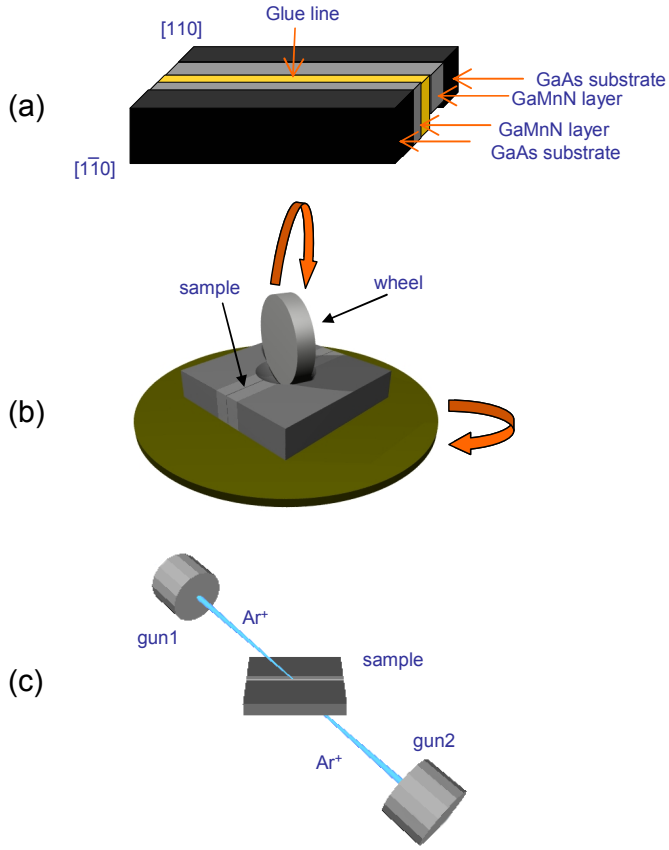

Figure 3.16 Schematic illustration of key sample preparation steps: (a) two cleaved pieces of sample glued face to face orthogonally using epoxy resin, (b) following the mechanical polishing on both sides, the specimen was dimpled from one polished side directly down to less than 30 µm, (c) Low angle ion beam milling was used to thin the specimen using low angle ion beam milling[5].

For the preparation of cross-sectional TEM specimens, in order to protect the epilayer during sectioning, two pieces of sample, orthogonally cleaved, were glued face to face using epoxy resin and cured for 24 hours under applied pressure to ensure that the glue line was as thin as possible. They were sequentially mechanically polished down to a thickness of around 100 µm using 35, 22 and 15 µm SiC grinding papers. Extra mechanical support was provided by a copper washer of 3 mm diameter and 50µm thickness, glued onto the sample. After curing, the specimen was dimpled from one polished side directly down to less than 30 µm, with dimpling conditions used being

[5] Figures 3.16b,c by courtesy of Mike Fay.

7 g load and 5 rpm stage oscillation, using 5 rpm wheel rotation and 6 and 1 μm diamond paste in sequence. A Fischione ion mill was then used to sputter the sample at a low angle of 15° with double-side initial milling performed at a voltage of 6 kV. A voltage of 2 kV was used to reduce surface amorphisation damage after perforation. Samples may also need to be plasma cleaned in O_2/Ar plasma to remove surface hydrocarbon contaminants, prior to insertion in the microscope for observation.

As to the preparation of plan-view TEM specimens, the polishing, dimpling and ion-beam milling processes are only performed on the side of the GaAs substrate, with the GaMnN layer becoming exposed upon perforation.

3.5 Summary

PAMBE provides a fine control over the growth process for GaMnN layers on GaAs(001), which is beneficial to deposit uniform GaMnN alloys. Complementary analysis is necessary for the purpose of assessing the interrelationship between process, structure and functional property of these GaMnN/GaAs(001) samples, with the near surface microstructure of each sample initially appraised using RHEED, sample bulk structure appraised using XRD, sample microstructure appraised using TEM imaging and electron diffraction techniques and sample chemical information obtained using EDX, EELS and EFTEM. Appropriate procedures for the preparation of TEM thin foils are then introduced. In addition, the GaMnN/GaAs(001) sample polarity was determined in each case using CBED, providing valuable sample orientation information for further discussion.

Appendix to Chapter Three

There are three scattering paths from the central beam to the 200 reflection, namely: $000 \rightarrow 11,1,\bar{1} \rightarrow 200$, $000 \rightarrow \bar{9}1\bar{1} \rightarrow 200$ and $000 \rightarrow 200$, as shown in Figure 3.17 [128,131].

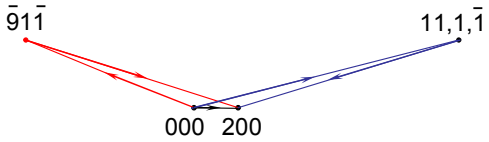

Figure 3.17 The interaction of a pair of doubly diffracted -91-1 and 11,1,-1 reflections with a 200 reflection [128].

The polynominal expression for the dynamical diffraction amplitude of an h, k reflection from a parallel-plate crystal is written in Equation 3.10 [131,135]. Here h_j represents the three-dimensional indices $h_jk_jl_j$ of each scattering vector and $h = \sum_{j=1}^{n} h_j = (hkl)$. n is the times of interactions and σ is the interaction constant. Each Φ represents a kinematical structure factor. ζ_r is an excitation error for r^{th} scattering at h^r, where $h^r = \sum_{j=1}^{r} h_j$. Z_n tends to be negligible for large excitation errors. The summation over the index l associated with the reciprocal axis normal to the crystal surface.

$$\Psi(h,k) = \sum_{l}\sum_{n}\sum_{h_1}\cdots\sum_{h_{n-1}}(-i\sigma)^n \Phi(h_1)\cdots\Phi(h_{n-1})\Phi(h_n)Z_n(\xi_1\cdots\xi_{n-1}\xi_n) \quad \text{Equation 3.10}$$

At the exact Bragg condition, Z_n is proportional to H, the sample thickness or $H^2/2$ for single or double scattering respectively. Thereby, equation 3.10 can be rewritten as:

$$\Psi(20) \approx -i\sigma H\Phi(200) + (-i\sigma H)^2 / 2[\Phi(11,1,\bar{1})\Phi(\bar{9}\bar{1}1) + \Phi(\bar{9}1\bar{1})\Phi(11,\bar{1},1)] \quad \text{Equation 3.11}$$

$$\Psi(\bar{2}0) \approx -i\sigma H\Phi(\bar{2}00) + (-i\sigma H)^2 / 2[\Phi(\bar{1}\bar{1},1,\bar{1})\Phi(9\bar{1}1) + \Phi(9\bar{1}\bar{1})\Phi(\bar{1}\bar{1},\bar{1},1)] \quad \text{Equation 3.12}$$

The structure factor of GaAs is given by Equation 3.13

$$\Phi(hkl) = \{f_{Ga}(hkl)\exp[2\pi i(-\frac{1}{8})(h+k+l)] + f_{Ga}(hkl)\exp[2\pi i(\frac{1}{8})(h+k+l)]\}G(hkl)$$

Equation 3.13

For convenience, the origin of the unit cell is moved to the centrosymmetric position with the nearest atoms at (-1/8, -1/8, -1/8) and (1/8, 1/8, 1/8). Then, the structure factors of these reflections can be written (rewrite f_{Ga}=f-Δ and f_{As}=f+Δ, where Δ is positive)

$$\Phi(200) = 8\Delta_{200}i \quad \text{Equation 3.14}$$

$$\Phi(\bar{2}00) = -8\Delta_{200}i \quad \text{Equation 3.15}$$

$$\Phi(9\bar{1}\bar{1}) = \Phi(9\bar{1}1) = 4\sqrt{2}(f_{911} + \Delta_{911}i) \approx 4\sqrt{2}f_{911} \quad \text{Equation 3.16}$$

$$\Phi(\bar{9}\bar{1}\bar{1}) = \Phi(\bar{9}\bar{1}1) = 4\sqrt{2}(f_{911} - \Delta_{911}i) \approx 4\sqrt{2}f_{911} \quad \text{Equation 3.17}$$

$$\Phi(11,1,\bar{1}) = \Phi(11,1,\bar{1}) = -4\sqrt{2}(f_{11,1,1} - \Delta_{11,1,1}i) \approx -4\sqrt{2}f_{11,1,1} \quad \text{Equation 3.18}$$

$$\Phi(\bar{1}\bar{1},1,\bar{1}) = \Phi(\bar{1}\bar{1},1,\bar{1}) = -4\sqrt{2}(f_{11,1,1} + \Delta_{11,1,1}i) \approx -4\sqrt{2}f_{11,1,1} \quad \text{Equation 3.19}$$

Substituting these values back into the general expressions for the dynamical diffraction amplitude, (Equations 3.11 and 3.12),

$$\Psi(20) \approx 8\sigma H\Delta + 32\sigma^2 H^2 f_{11,1,1}f_{9,1,1} \quad \text{Equation 3.20}$$

$$\Psi(\bar{2}0) \approx -8\sigma H\Delta + 32\sigma^2 H^2 f_{11,1,1}f_{9,1,1} \quad \text{Equation 3.21}$$

Based on this analysis, it is accepted that the direct scattering into the 200 reflection and the double scattering are in phase leading to a bright cross, whilst the direct scattering into the $\bar{2}00$ reflection and the double scattering are out of phase leading to

a black cross. All the cases analysed with the atomic coordinates as given are consistent with the absolute orientation of the GaAs.

CHAPTER FOUR

Structural characterisation of zinc-blende GaMnN epilayers grown by MBE as a function of Ga flux

4.1 Introduction

The thermodynamic preference for the formation of wurtzite GaN over zinc-blende GaN can result in phase separation reactions during the growth of zinc-blende GaN on GaAs(001) substrates [49,51,52]. Growth temperature and stoichiometry are found to have a dominant effect on the development of the zinc-blende GaN phase, depending on the growth technique and precursors used [50,136]. By way of example, exact control of the III:V ratio close to the stoichiometric condition during MBE growth allows the production of single phase zinc-blende epitaxial layers, whilst deviation to Ga or N-rich conditions reportedly produces mixed phase zinc-blende and wurtzite material [49,51,52].

The limited solid solubility of Mn within GaN also provides a challenge for the growth of uniform GaMnN alloys by MBE. Experimentally, it is found that Mn can only be incorporated into the GaN lattice under N-rich conditions [69,72], whilst growth under Ga-rich conditions is associated with an improved epilayer microstructure [137].

In practice, establishing p-type conductivity is found comparatively easier within zinc-blende GaMnN than wurtzite GaMnN, where the transition metal species needs to be responsible for both the ferromagnetic properties and the p-type behaviour. By way of example, high p-type zinc-blende GaMnN layers with carrier concentrations exceeding $10^{18}cm^{-3}$ and a detected ferromagnetic signal over 400K have been obtained by PAMBE [4,5]. Room temperature ferromagnetism and p-type conductivity have also been reported for PAMBE grown zinc-blende GaN following Mn^{+} ion implantation and annealing [6].

In this chapter, the influence of the Ga/N ratio on the microstructural development of GaMnN/GaAs(001) grown by PAMBE, as assessed using a variety of complementary analytical techniques, is studied.

4.2 Experimental

Zinc-blende GaMnN epilayers were grown on semi-insulating (001) oriented GaAs substrates at 680°C by PAMBE, as previously detailed in Chapter Three. Briefly, in this case, first, a GaAs buffer layer at ~600°C and a 60 nm GaMnN initial nucleation layer were grown at 680°C under a slightly N-rich condition. A GaMnN layer was then deposited for 2 hours at 680°C under a certain Ga/N ratio varied by changing the Ga flux from 7.5×10^{-8} mbar to $1.2x10^{-6}$ mbar, with the Mn flux fixed at a level of 1.0×10^{-8} mbar. This corresponded to a transition from N-rich to Ga-rich conditions, with the latter being identified by the development of Ga droplets on the growth surface. An overall chamber pressure of $2\text{-}3\times10^{-5}$ mbar was maintained by a flow of N_2 with the Oxford Applied Research RF plasma source operated at 450 W. The growth conditions for the sample set investigated here are summarised in Table 4.1.

A more precise method of identifying the transition point from N-rich to Ga-rich growth was also employed by plotting the GaMnN film thickness as a function of Ga-flux, with the film thickness estimated by optical reflectivity. Ga droplets on the growth surface of some samples, e.g. samples GN6 and GN7, were etched first using boiling HCl before thickness measurement. As shown in Figure 4.1, the film thickness of this sample set increased from 200 to 750 nm with increasing Ga flux and a maximum growth rate was established under nearly 1:1 stoichiometry and Ga-rich conditions.

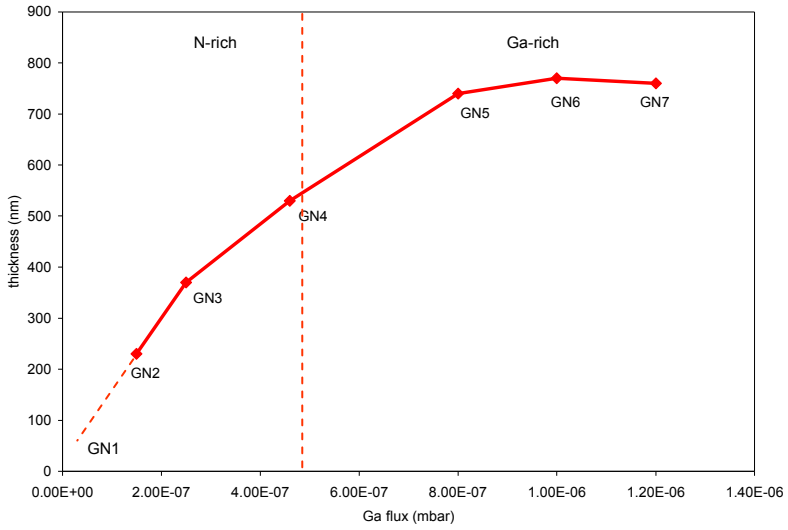

Figure 4.1 GaMnN layer thickness as a function of Ga-flux, with the transition point from N-rich to Ga-rich being identified when the film thickness reached the highest value.

Table 4.1 Details of the GaMnN /GaAs(001) sample set

Sample	**Tg / °C**	**N_2 / $\times10^{-5}$ mbar**	**Ga flux / $\times10^{-7}$ mbar**	**Mn flux / $\times10^{-8}$ mbar**	**thickness / µm**	**XRD FWHM/°**	**Ga/N ratio**	**Mn concentration / at% (EDX)**	**Comparative room temp ferromag signal**
GN1	680	2-3	0.75	1	0.12	1.2 ± 0.1	N-rich	3.3	medium
GN2	680	2-3	1.5	1	0.23	1.1	N-rich	-	strong
GN3	680	2-3	2.5	1	0.37	1.0	N-rich	-	strong
GN4	680	2-3	4.6	1	0.53	1.4	~1:1 (slightly N-rich)	4.0	medium
GN5	680	2-3	8.0	1	0.74	1.0	Ga-rich	0	weak
GN6	680	2-3	10	1	0.77	0.8	Ga-rich	0	none
GN7	680	2-3	12	1	0.76	0.9	Ga-rich	0	none

4.3 Results

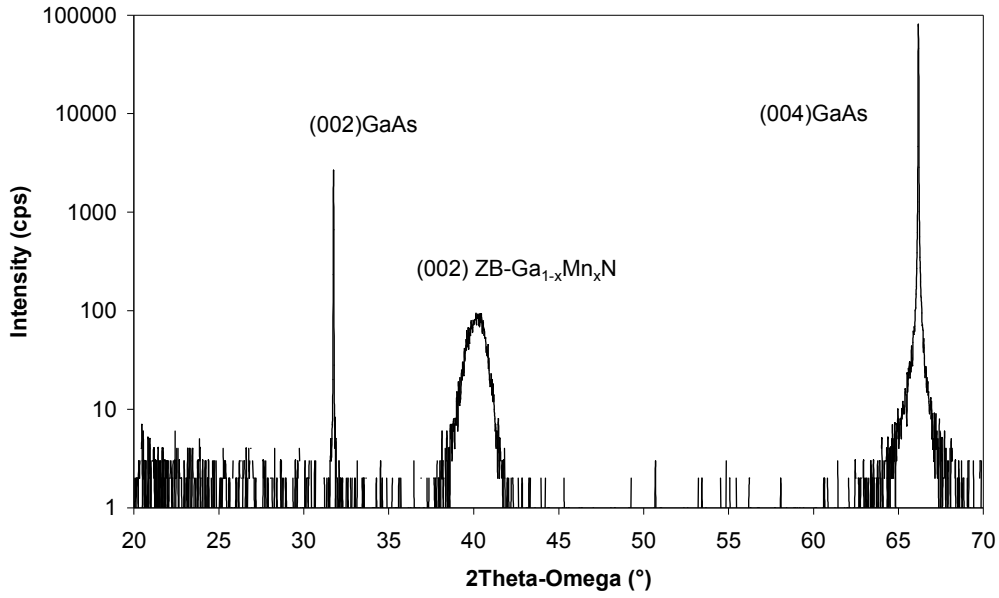

Figure 4.2 2θ-Ω X-ray diffraction profile of sample GN1 grown under N-rich conditions, showing that the epilayer is single phase zinc-blende GaMnN

The XRD spectrum from sample GN1 shown in Figure 4.2 is representative of the XRD spectra obtained across the sample set, confirming the formation of the zinc-blende phase. Variation in the full width at half maxima (FWHM) values for the 002 reflection across the stoichiometric range (Table 4.1) suggests a variation in the layer structural quality, becoming optimised for conditions of slightly Ga-rich growth. There was no evidence for the presence of second phase wurtzite material from any of these spectra.

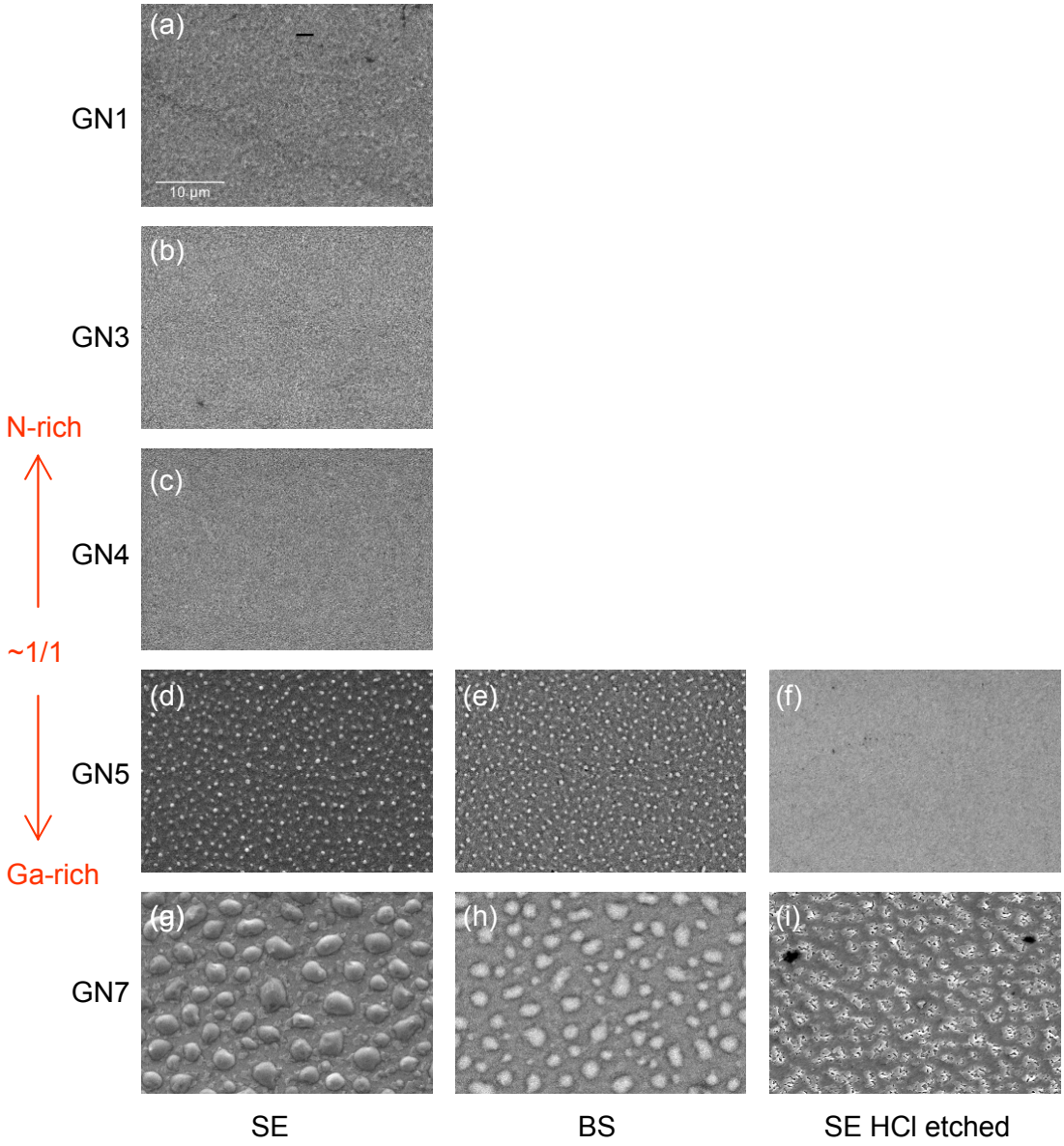

Figure 4.3 SE images of GaMnN grown under (a,b) N-rich (samples GN1 and GN3); (c) ~1:1 stoichiometry (sample GN4); and (d, g) Ga-rich conditions (samples GN5 and GN7). (e,h) back-scattered electron images of samples GN5 and GN7 and (f, i) SE images of samples GN5 and GN7 following HCl etching to remove the surface Ga droplets.

Secondary electron (SE) images of the as-grown surfaces of samples GN1, GN3, GN4, GN5 and GN7 are shown in Figure 4.3, corresponding to N-rich (GN1 and GN3), ~1:1 stoichiometry (GN4) and Ga-rich conditions (GN5 and GN7), respectively. The sample grown close to stoichiometric conditions (Figure 4.3c) appears specular, indicative of a smooth surface. The sample grown under N-rich

conditions appears to exhibit a slightly rougher surface, whilst samples grown under Ga-rich conditions show increasing amounts of Ga droplets on the sample surface with increasing Ga flux, as highlighted in the back-scattered electron images shown in Figures 4.2e,h. Figures 4.2f,i correspond to sample GN5 and GN7 following etching in boiling HCl to remove the Ga droplets, indicating a pitted surface.

Pairs of RHEED patterns recorded along orthogonal <110> projections for this sample set are presented in Figures 4.4a-j, providing information on the near surface microstructure of samples GN1, GN3, GN4, GN5 and GN7, respectively. RHEED observation of the as-grown Ga-rich samples was hindered by the presence of Ga droplets and associated oxidation, leading to the production of hazy diffraction patterns (Figures 4.4k,l). However, removal of the Ga droplets using boiling HCl allowed RHEED patterns with clear, sharp spots to be obtained (Figures 4.4g-j). All the samples demonstrated cubic structure with extra spots and/or streaks indicating varying degrees of mixed phase content at the growth surface and/or stacking disorder on inclined {111} planes. In particular, a transition from mixed hexagonal/cubic (α/β) phase material for highly N-rich growth conditions to single phase cubic material for Ga-rich growth conditions was observed. Varying degrees of anisotropy in the epilayer defect microstructure were also apparent across the sample set.

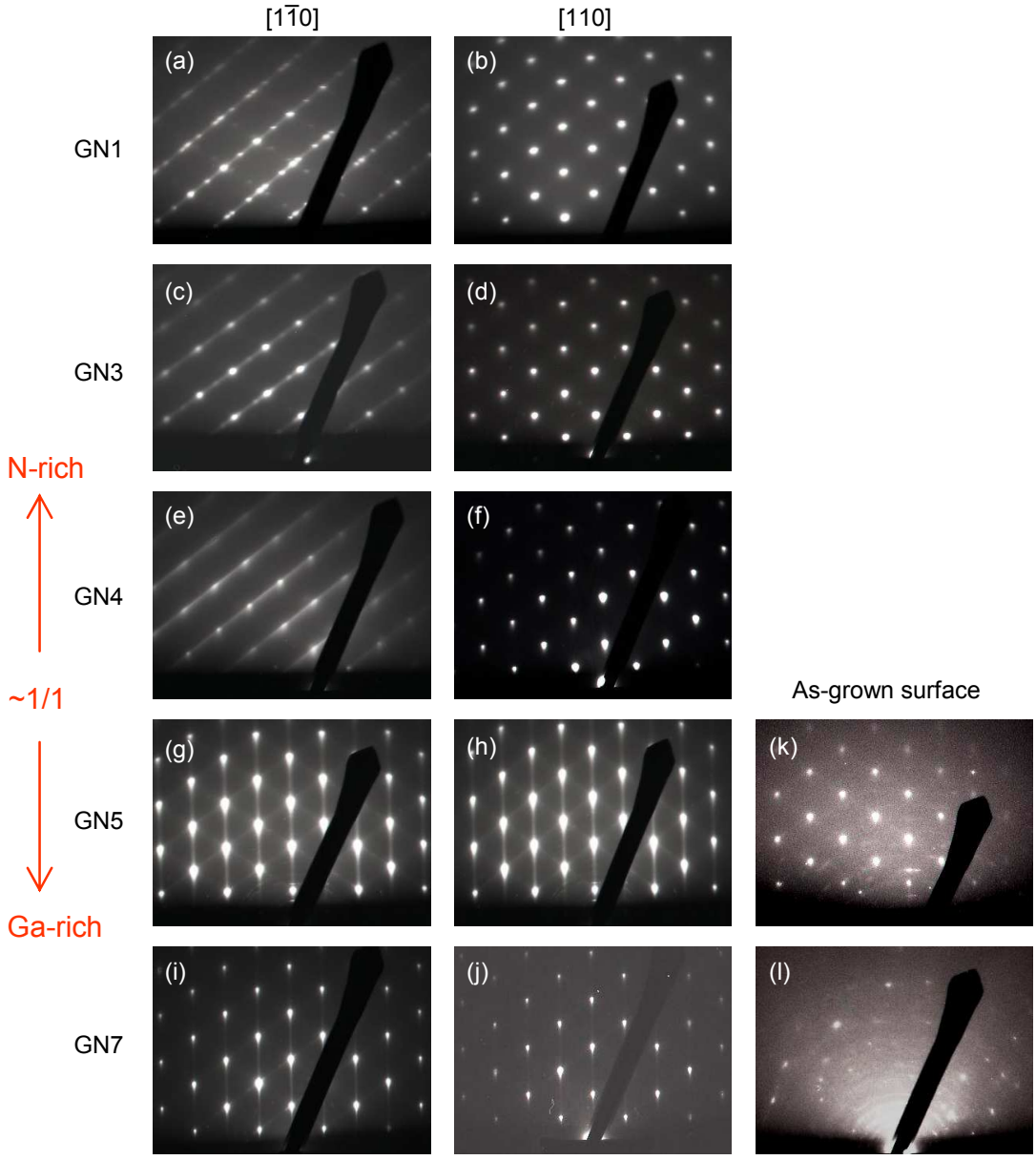

Figure 4.4 200kV RHEED patterns for the as-grown GaMnN, (a,b) sample GN1, (c,d) sample GN3 and (e,f,) sample GN4; and HCl etched (g,h) sample GN5 and (i,j) sample GN7, recorded along orthogonal <110> projections suggesting a transition from mixed cubic / hexagonal phase near surface structure under N-rich conditions to single crystal cubic phase growth under Ga-rich conditions. Strong anisotropy in the near surface microstructure of samples grown under N-rich conditions is also apparent. (k,l) RHEED patterns for the as-grown samples GN5 and GN7, respectively.

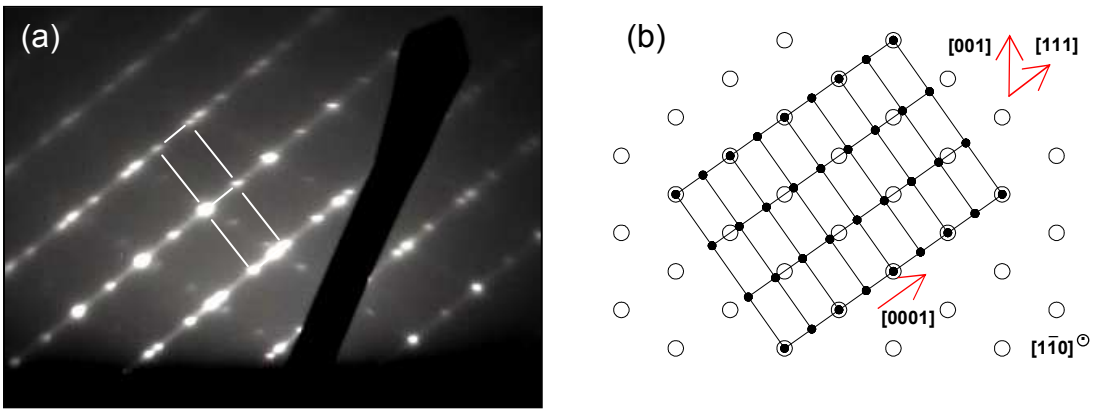

Figure 4.5 Enlargement of the $<1\bar{1}0>$ RHEED pattern of Figure 4.4a corresponding to GaMnN grown under highly N-rich conditions. (b) Associated schematic illustration denoting diffraction spots corresponding to the zinc-blende (open circles) and wurtzite (solid dots) phase.

By way of example, for sample GN1 grown under highly N-rich conditions, dominant diffraction spots from both cubic and hexagonal material at the growth surface were identified, as emphasised by the enlarged diffraction pattern of Figure 4.5a. The indexing of Figure 4.5a, clarified with reference to the schematic diagram of Figure 4.5b (indexed absolutely following subsequent polarity investigation of the associated TEM sample foil), illustrates the orientation relationship between the two phases for the projection of $[1\bar{1}0]_\beta$ // $[11\bar{2}0]_\alpha$ with a dominant domain variant of $[111]_\beta$ // $[0001]_\alpha$. Such a precise orientation relationship does not occur for the orthogonal projection of this mixed phase sample and consequently just the $[110]_\beta$ diffraction pattern is apparent within Figure 4.4b. It is noted that the extra spots due to the surface hexagonal phase became faint with increasing Ga flux, disappearing when the Ga/N ratio approached ~1:1 stoichiometry (Figure 4.4e), while streaks preferentially aligned along the $[111]_\beta$ direction for the $[1\bar{1}0]_\beta$ sample projection were maintained, indicating the preferential alignment of inclined planar defects (i.e. thin microtwins and stacking faults) predominantly on just one set of {111} planes inclined to the

growth surface (Figures 4.4a, c and e). Similar streaks were observed along the complete set of <111> directions for both orthogonal <110> projections of the samples grown under Ga-rich conditions, again attributable to a high density of inclined planar defects, but without the same sense of strong anisotropy in their distribution (Figures 4.4g-j). The variation in the anisotropic distribution of inclined planar defects suggests that this effect arises from the transition from N-rich to Ga-rich growth, e.g. due to differences in III/V stoichiometry at the growth surface, rather than being due to slight vicinality of the substrate.

The presence of well-defined diffraction spots for these RHEED patterns is indicative of a rough growth surface, i.e. due to coupling of the electron beam with three-dimensional volumes of near surface material, whilst streaks perpendicular to the growth plane (Figures 4.4g-j) are generally attributed to a smoother surface whereby two dimensional coupling of the beam with the material tends to occur, with consequent formation of diffraction rods rather than points in reciprocal space. In this context, the presence of streaking perpendicular to the shadow edge of samples grown under Ga-rich conditions, following HCl etching, is attributed to patches of relatively smooth surface. More precisely, the diffraction effect of streaks normal to the growth surface is attributed to material that is not perfectly flat, but with slight local mis-orientations combined with some degree of surface disorder [138].

TEM investigations across the sample set demonstrated the presence of highly faulted defect microstructures in all the specimens. GaAs buffer layer thicknesses were confirmed at 145±5 nm in each case. The epilayer thicknesses of the samples grown under N-rich conditions were found to increase with increasing Ga flux, ranging e.g.

from ~200±30 nm for sample GN1, reaching 400±10 nm for sample GN4, and establishing a plateaux value for samples grown under Ga-rich conditions, e.g. around 590±20 nm for sample GN7. These increasing layer thickness values broadly agree with the optical reflectivity measurements.

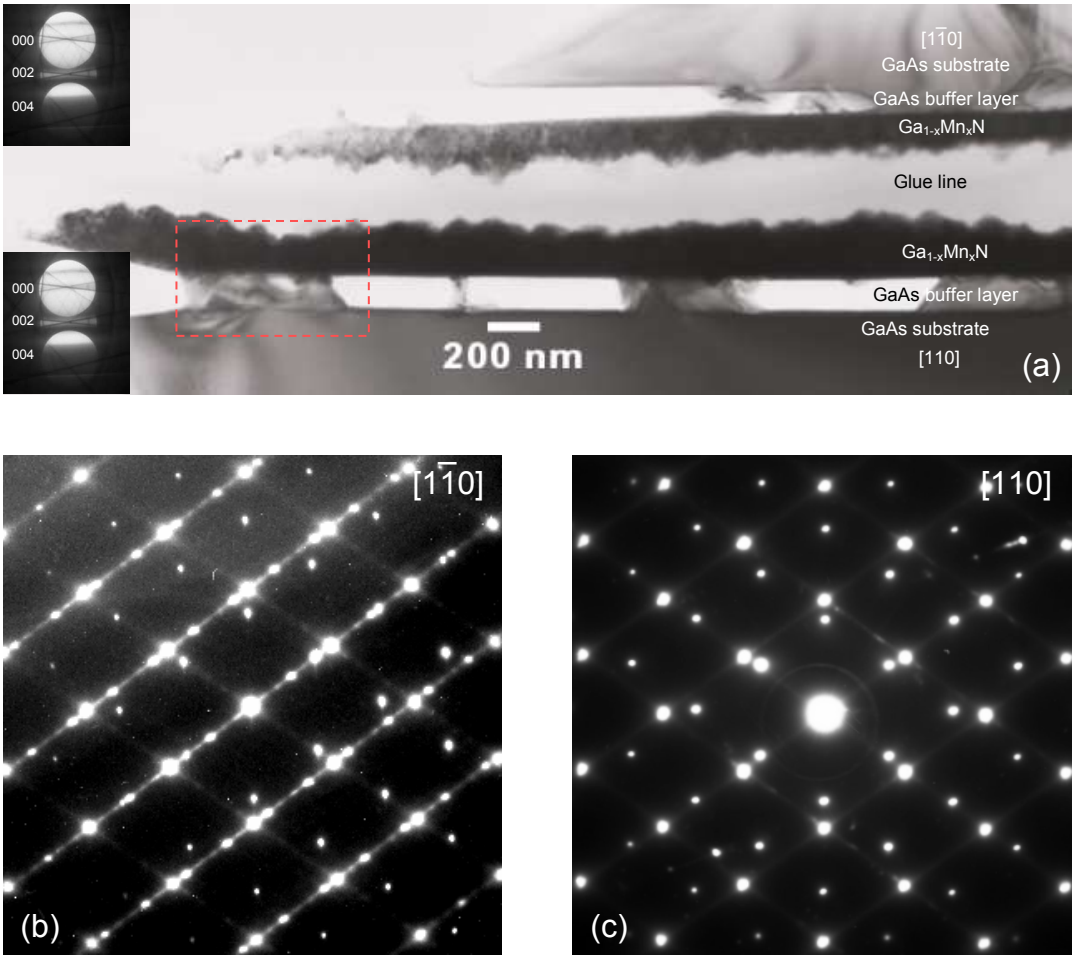

Figure 4.6 (a) Low magnification cross-sectional, many beam TEM image of sample GN1, corresponding to orthogonal <110> projections across the glue line. (b) [1$\bar{1}$0] zone axis and [110] zone axis SAED patterns confirm the epitaxial growth of GaMnN on the GaAs(001) substrate.

By way of illustration, Figure 4.6a presents a low magnification, many-beam, bright field, cross-sectional TEM image of sample GN1, corresponding to orthogonal [110] and [1$\bar{1}$0] sample projections either side of the glue line. In addition to the main

defining features of the highly faulted epilayer with rough surface morphology, voids within the buffer layer flattening out at the GaAs buffer/substrate interface and pyramidal inclusions on the scale of ~100 nm extending into the buffer layer were observed. Two SAED patterns recorded along $[1\bar{1}0]$ and [110] zone axes are also shown in Figures 4.6b and c, respectively, demonstrating the overlapping of well defined diffraction spots from both the epilayer and the substrate confirming the epitaxial growth of GaMnN on GaAs(001) with precise orientation relationship of $(001)_{GaMnN}//(001)_{GaAs}$ and $[110]_{GaMnN}//[110]_{GaAs}$. A strong anisotropy is also apparent in that the $[1\bar{1}0]$ zone axis pattern contains extra spots from hexagonal GaMnN and streaks along <111> directions indicating a high density of stacking disorder on inclined {111} planes, whilst the [110] zone axis diffraction pattern exhibits clearer, sharp diffraction spots.

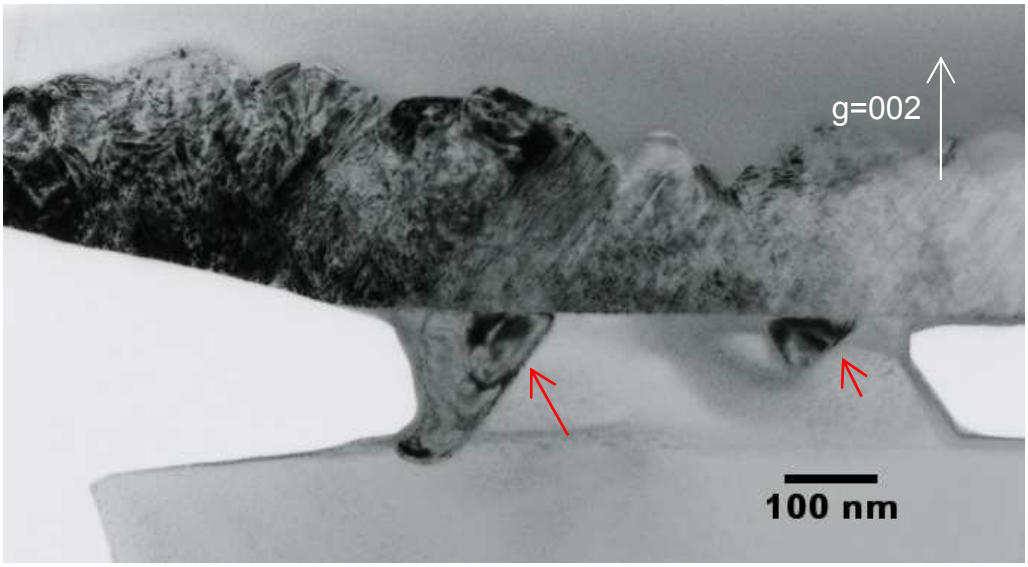

Figure 4.7 002 dark field image of boxed region of sample GN1 in Figure 4.6a showing α-MnAs inclusions extending into the GaAs buffer layer.

Figure 4.7 shows a dark field image of the boxed region within Figure 4.6a, clarifying the highly faulted nature of the epilayer, along with pyramidal precipitates (arrowed)

extending into the GaAs buffer layer. EDX measurements confirmed the presence of Mn and As within such inclusions (Figure 4.8c). Associated selected area diffraction patterns (Figure 4.8a) confirmed that the inclusions comprised α-MnAs. The indexing of Figure 4.8a is clarified, following determination of absolute sample polarity, with reference to the schematic diagram of Figure 4.8b. The orientation relationship here between α-MnAs and GaAs is given by $[1\bar{1}20]_{MnAs}$ // $[110]_{GaAs}$ with two domain variants according to the stacking of closed packed planes, e.g. $[0001]_{MnAs}$ // $[\bar{1}\bar{1}1]_{GaAs}$. It is noted that this orientation relationship between α-MnAs and GaAs is consistent with that of MnAs formed within GaAs following Mn ion implantation and annealing [31], whilst differing from two reported orientations for the direct epitaxial growth of MnAs on GaAs(001), as assessed using RHEED and XRD (i.e. $[\bar{1}\bar{1}20]_{MnAs}$ // $[110]_{GaAs}$ and $[0001]_{MnAs}$ // $[\bar{1}\bar{1}0]_{GaAs}$ (termed type A), and $[\bar{1}\bar{1}20]_{MnAs}$ // $[\bar{1}\bar{1}0]_{GaAs}$ and $[\bar{1}\bar{1}02]_{MnAs}$ // $[110]_{GaAs}$ (termed type B)) [36].

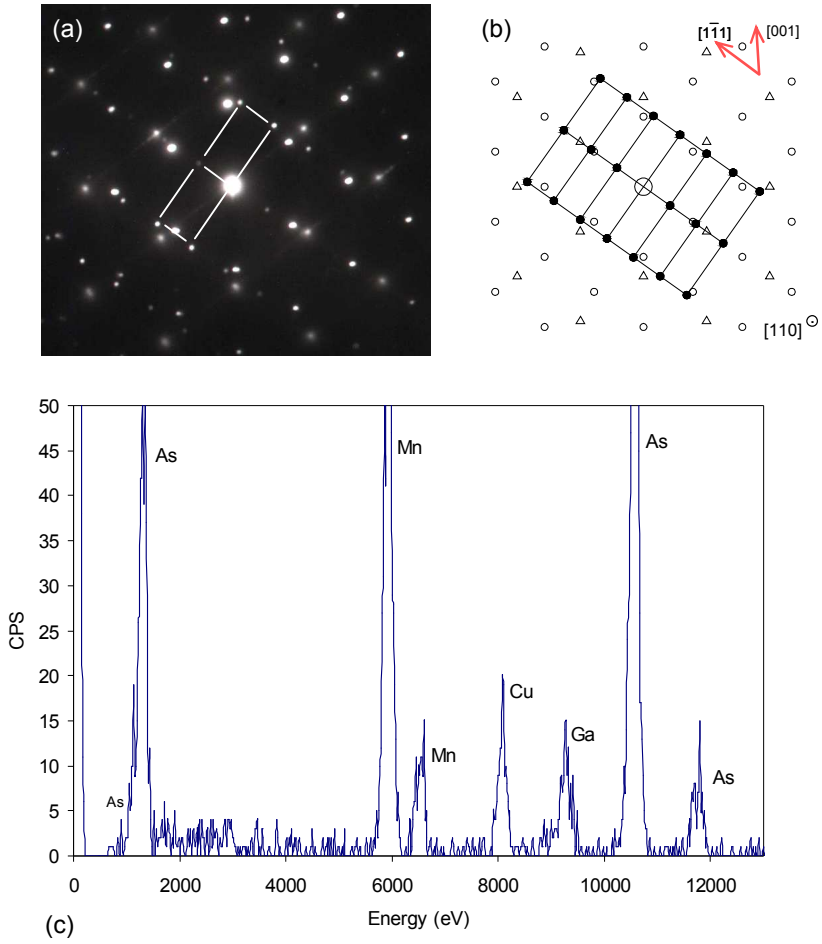

Figure 4.8 (a) Selected area diffraction pattern recorded from the region of an inclusion. (b) Schematic illustration denoting diffraction spots due to zinc-blende GaMnN (open triangles); GaAs (open circles) and α-MnAs (solid dots). (c) EDX spectrum demonstrating the inclusions comprise Mn and As.

Figure 4.9 shows a plan view TEM image from an electron transparent foil sectioned through the GaMnN/GaAs interface plane of sample GN1, as evidenced by the overlapping diffraction pattern inset. In particular, a number of features, ~100-200nm in size, exhibiting differing contrast levels were delineated, and these again showed strong Mn and As signals with EDX analysis, consistent with the presence of α-MnAs.

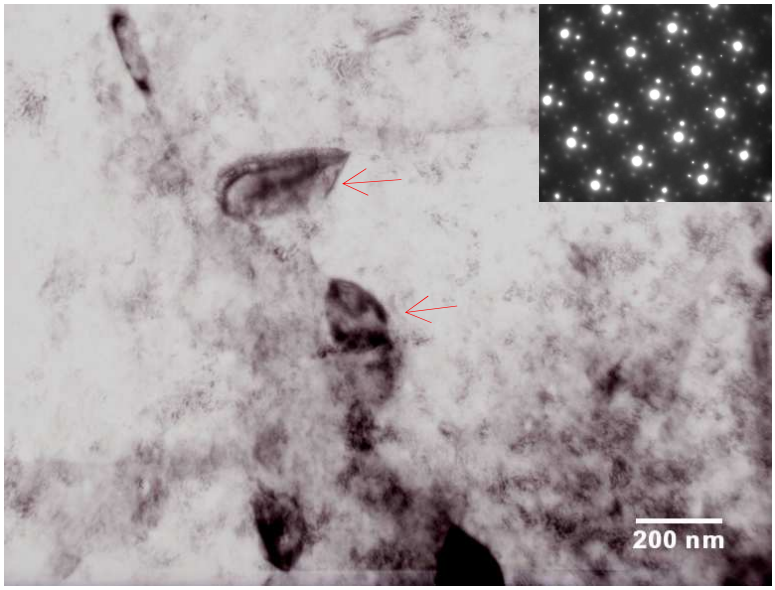

Figure 4.9 Plan-view TEM image through a section of the GaMnN/GaAs(001) interface plane of sample GN1 showing the distribution of MnAs inclusions, with the [001]GaMnN//[001]GaAs zone axis diffraction pattern inset.

It is emphasised that such MnAs inclusions were identified within all the samples across the stoichiometry range, using EDX and SAED, with decreasing size upon transition to Ga-rich growth conditions, as illustrated by Figures 4.10a,b (samples GN4 and GN7), corresponding to inclusion sizes of 70±10nm and 40±10nm, respectively. Voids extending into the buffer layer were also observed for all the samples. Further, the orientation relationship between these MnAs inclusions and the GaAs substrates was investigated using SAED carefully throughout the sample set by the identification of joint diffraction patterns from GaAs and MnAs along either the [110] or $[1\bar{1}0]$ projection. When combined with the information on sample polarity obtained from the GaAs substrates, it was found that the orientation relationship between these two materials is in fact affected by the Ga/N ratio: a swap in orientation relationship occurs when the Ga/N ratio was changed from N-rich ($[11\bar{2}0]_{MnAs}//[110]_{GaAs}$) to Ga-rich ($[11\bar{2}0]_{MnAs}//[1\bar{1}0]_{GaAs}$) growth as summarised in Table 4.2.

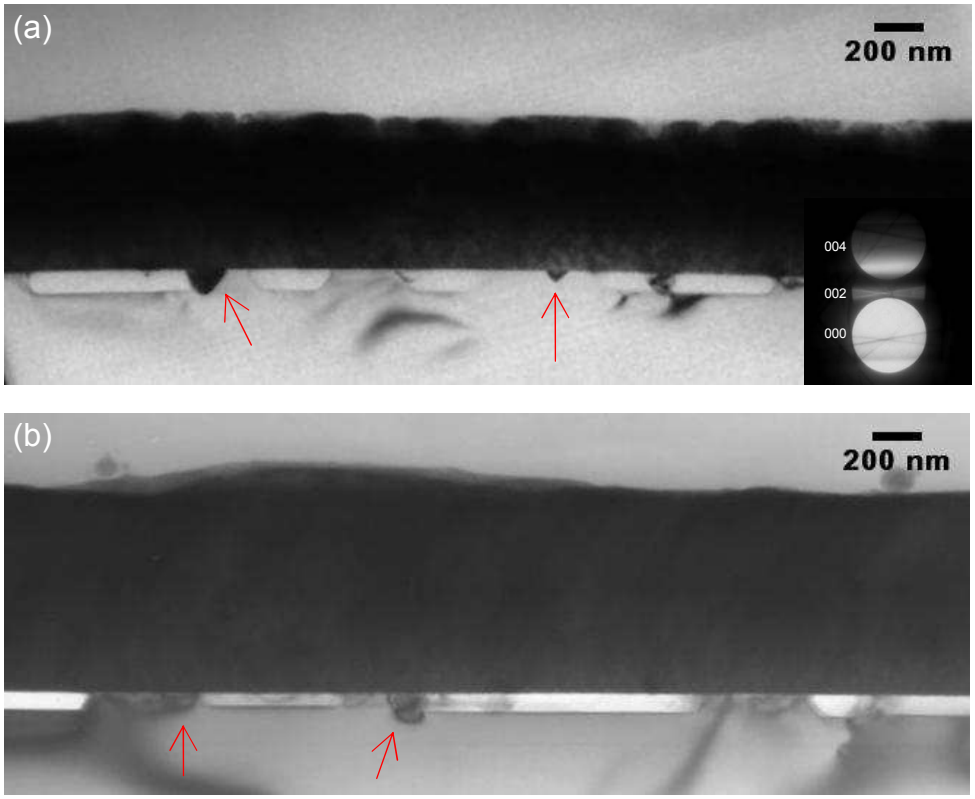

Figure 4.10 Cross-sectional TEM images of (a) sample GN4 and (b) sample GN7, again showing the presence of voids and α-MnAs inclusions extending into the GaAs buffer layer.

Table 4.2 Orientation relationship between the MnAs and GaAs across the sample set

Sample	**Growth condition**	**Orientation relationship 1** $[1\bar{1}20]_{MnAs}//[110]_{GaAs}$	**Orientation relationship 2** $[1\bar{1}20]_{MnAs}//[\bar{1}\bar{1}0]_{GaAs}$
GN1	N-rich	√	
GN4	N-rich	√	
GN5	Ga-rich		√
GN6	Ga-rich		√
GN7	Ga-rich		√

Selected area electron diffraction and diffraction contrast imaging experiments were performed in order to clarify the origin of the hexagonal phase within the N-rich samples of this sample set, as indicated by RHEED. Figure 4.11a shows a centred dark field image formed from a diffraction spot attributed to wurtzite GaMnN (e.g. as arrowed in Figure 4.11b), as distinct from streaks and extra spots at 1/3<111> positions arising from the presence of stacking faults and microtwins. This indicates the localisation of small grains of wurtzite GaMnN at the growth surface. Slight

overlap from twinning reflections through the objective aperture, due to slight convergence of the imaging beam, also contributes to this dark field image, partially highlighting the stacking disorder on one set of {111} planes. Since selected area diffraction experiments provided no evidence for the presence of wurtzite domains through the bulk of the epilayer and no evidence was found for hexagonal phase material at the epilayer/substrate interfaces, the formation of wurtzite GaMnN is attributed to a cool down effect at the end of growth whereby a slight change in surface stoichiometry might have occurred corresponding to increasing N-rich conditions, allowing small grains of the more stable hexagonal phase to become established at the growth surface.

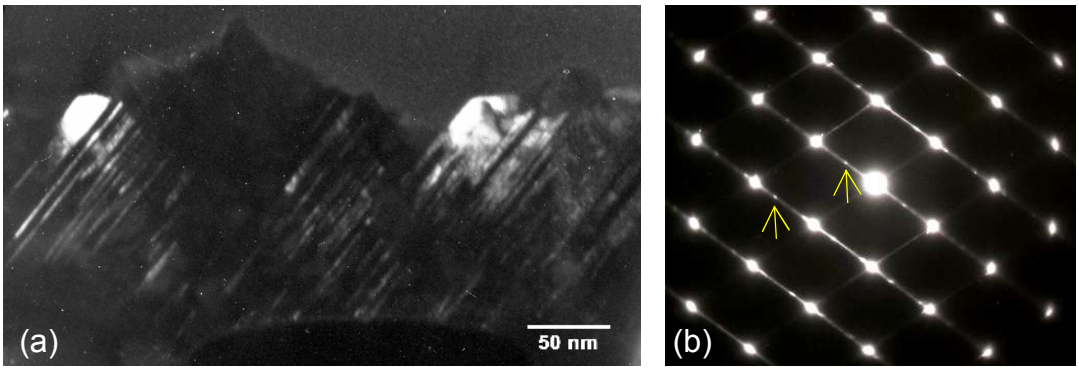

Figure 4.11 (a) Dark-field, cross-sectional TEM image of the near surface microstructure of sample GN1 suggesting that the wurtzite GaMnN phase corresponds to localised small grains at the growth surface. (b) Associated $[1\bar{1}0]$ selected area electron diffraction pattern, with wurtzite diffraction spots used to form such dark field images (arrowed).

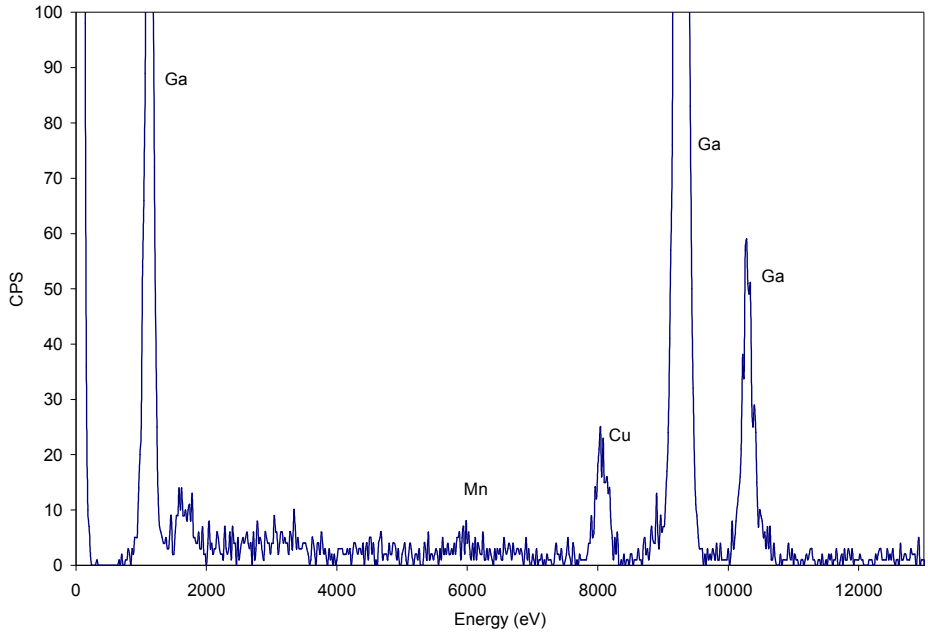

Figure 4.12 EDX spectrum of sample GN1 indicating the incorporation of Mn with this sample.

The Mn content across the sample set was measured using an Oxford Instruments EDX system attached to the Jeol 2000fx TEM with a representative spectrum obtained from sample GN1 shown in Figure 4.12. Using spot mode, a relatively uniform Mn content of ~ 3.3 at% was indicated for sample GN1, peaking at a value of ~ 4.0 at% for sample GN4, while the Mn content was below the detectability limit of EDX for samples grown under Ga-rich conditions. This is consistent with reports of wurtzite GaMnN/sapphire grown by MBE as assessed using EDX [69] and SIMS [72], respectively, which demonstrate that N-rich (and Mn-rich) conditions are required for the successful incorporation of Mn into the crystal lattice.

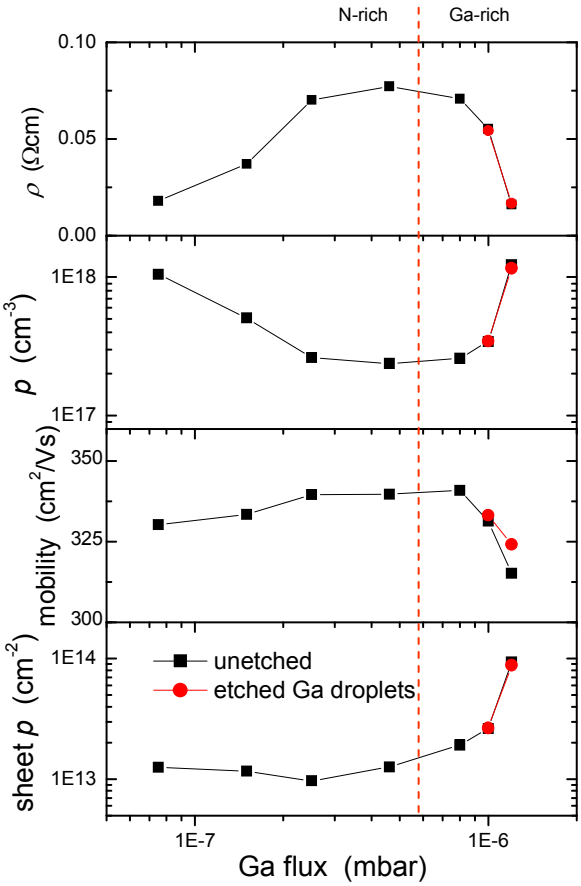

Figure 4.13 Resistivity, bulk hole concentration, hole mobility, and sheet carrier concentration of this sample set.

The electrical properties[6] of these samples were appraised in detail as published elsewhere [4,139,140]. Briefly, these zinc-blende GaMnN films grown on (001) oriented GaAs substrates are all p-type materials. Nearly identical results were obtained for samples grown under Ga-rich conditions before and after removal of Ga droplets on the growth surface, as shown by the solid-dot data points in Figure 4.13, with electrical properties being plotted as a function of the Ga flux. There was no obvious change in sheet hole density and hole mobility with increasing Ga flux until the sample growth was carried out under Ga-rich conditions, where sheet hole density

[6] The electrical property measurements were carried out by Kevin Edmonds in the School of Physical and Astronomy.

increases and hole mobility decreases slightly. For both N-rich and Ga-rich growth conditions, a bulk hole density of about 10^{18} cm^{-3} with a corresponding mobility of 300 $cm^2V^{-1}s^{-1}$ were achieved.

4.4 Discussion

It is noted that a full discussion of the growth and microstructural development of these GaMnN/GaAs(001) with increasing Ga flux will be given in Chapter Seven, with particular attention being given to the following questions:

N-rich and nearly 1:1 Ga/N ratio growth conditions are associated with the incorporation of Mn into GaN lattice, whilst Ga-rich conditions are associated with a slightly improved GaMnN microstructure and a maximum growth rate. Identical results regarding the strong influence of Ga/N ratio on Mn incorporation into hexagonal GaN were also achieved by Haider et al [69] and Kuroda et al [72]. Based on well established theories on the growth of zinc-blende and wurtzite GaN, it is considered that the growth surface is always terminated by Ga atoms, being independent on Ga/N ratio. Therefore, Ga-rich conditions lead to the formation of a thick Ga layer on the sample surface, inhibiting Mn migration to the growth front. In parallel, under N-rich conditions, strong Mn-N bonds may form on the growth front, resulting in an anisotropic growth as confirmed by SAED and RHEED.

Combining the experimental results presented in Chapter Five and Chapter Six, MnAs inclusions at the GaMnN and GaAs interface extending to the GaAs substrate were identified within all samples. It is considered that these MnAs are formed due to the

diffusion of Mn through the GaMnN and GaAs interface during growth and have no effect on the material bulk functional properties.

4.5 Summary

The Ga/N ratio was found to have a dominant impact on the zinc-blende GaMnN epilayer growth rate and resultant composition, morphology and microstructure. A maximum growth rate is associated with growth under nearly 1:1 Ga:N ratio and Ga-rich conditions. The indication from RHEED patterns and XRD spectra, together with SEM observation is that slightly Ga-rich conditions corresponds to an optimised, but still highly faulted microstructure. These results are enhanced by TEM observation, giving the insight into the development of the GaMnN microstructure, containing a high density of planar defects on inclined {111} planes. Hexagonal phase is only located on the surfaces of samples grown under highly N-rich conditions, attributed to a cool down effect at the end of growth. Mn incorporation is only associated with nearly 1:1 Ga:N ratio and N-rich growth conditions, whilst no Mn was detected using EDX for samples grown under Ga-rich conditions.

α-MnAs inclusions and voids extending into the GaAs buffer layer were observed in all cases, however they are considered not to affect the layer electrical and magnetic properties. It is noted that the orientation relationship is affected by the growth conditions, and that N-rich conditions are associated with the $[1\bar{1}20]_{MnAs}//[110]_{GaAs}$ orientation relationship, whilst Ga-rich conditions are associated with $[1\bar{1}20]_{MnAs}//[\bar{1}\bar{1}0]_{GaAs}$.

CHAPTER FIVE

Microstructural characterisation of zinc-blende GaMnN grown by MBE as a function of Mn flux

5.1 Introduction

In view of the Mn solid solubility issue leading to reports of various phase separation reactions, establishing appropriate conditions for the growth of uniform alloys of GaMnN and for increasing Mn contents, becomes an intriguing challenge. For example, the precipitation of Mn_3N_2 and $Mn_6N_{2.58}$ have been reported for GaN epilayers grown on sapphire substrates by MOCVD followed by Mn^+ ion implantation and annealing, as assessed by XRD [81]. Conversely, the development of precipitates of $GaMn_3N$ [72,78] and Mn_4N [141] alloys have been found for wurtzite GaMnN grown on sapphire substrates by MBE, as assessed using XRD. It was suggested that high temperature annealing [81] and high concentrations of Mn within the GaMnN lattice [72,78,141] were responsible for the formation of these second phase precipitates.

In parallel, magnetic measurements show a remarkably large variation in experimental T_C values, from a few K to well above room temperature. By way of example, for a GaMnN sample with 14 at% Mn grown on 4H-SiC(0001) substrates by MBE, ferromagnetic properties up to 750 K were reported, with Mn-rich clusters

being identified by TEM rather than by XRD, whilst a sample with a lower Mn content of 7.6 at% was reported as having a very low T_C below 6 K, exhibiting no trace of any second phase material [76]. Further, GaMnN films with 3 at% Mn grown on sapphire substrates by MOCVD were confirmed to be single phase by XRD, showing a ferromagnetic signal up to 350 K. The substantial variation in the experimental T_C values is suggested to be due to Mn-rich precipitates and the formation of giant magnetic moments within these precipitates [114].

To date, most reports concerning room temperature ferromagnetism in GaMnN employ XRD, selected-area electron diffraction (SAED) within TEM and/or extended X-ray absorption fine structure (EXAFS) as main characterisation methods to identify the alloy uniformity and Mn positions. However, considering the levels of Mn doping within alloy GaMnN and the associated very high defect density, it is often very difficult to determine the nature of any additional Mn-rich phases using these conventional methods. Even if a high T_C is apparent, it can only be speculatively attributed to additional Mn-rich phases.

In this chapter, the influence of increasing Mn flux on the development of the GaMnN microstructure is investigated. High levels of Mn incorporation under high Mn flux is suggested to promote the formation of Mn-rich nano clusters, providing a real chance for the identification of these precipitates using XRD, electron diffraction, high-resolution TEM and energy filtered TEM. The growth conditions for the sample set investigated here are summarised in Table 5.1. Briefly, an overall chamber pressure of $2\text{-}3\times10^{-5}$ mbar and a Ga flux of 2×10^{-7} mbar were maintained to provide slightly N-rich growth conditions, considered to be beneficial for Mn incorporation. The Mn flux

was varied from 0 to 25×10^{-9} mbar corresponding to Mn concentrations of 0 to ~6.6 at%, as estimated by the correlation of Mn-flux and the corresponding Mn concentration obtained from secondary ion mass spectrometry (SIMS) measurements [5].

Table 5.1 Growth details of the GaMnN/GaAs(001) sample set with increasing Mn flux

Sample	Tg / °C	N_2 / $\times10^{-5}$ mbar	Ga flux / $\times10^{-7}$ mbar	Mn flux / $\times10^{-9}$ mbar	Estimated Mn concentration from MBE / at%	Estimated Mn concentration from SIMS / at%	Estimated Mn concentration from EDX / at%
M0	680	2-3	2	0	0	0	
M1	680	2-3	2	0.495	0.3	0.04	
M2	680	2-3	2	1.65	1	0.22	
M3	680	2-3	2	4.95	3	1	
M4	680	2-3	2	25	15	6.6	~5

5.2 Results

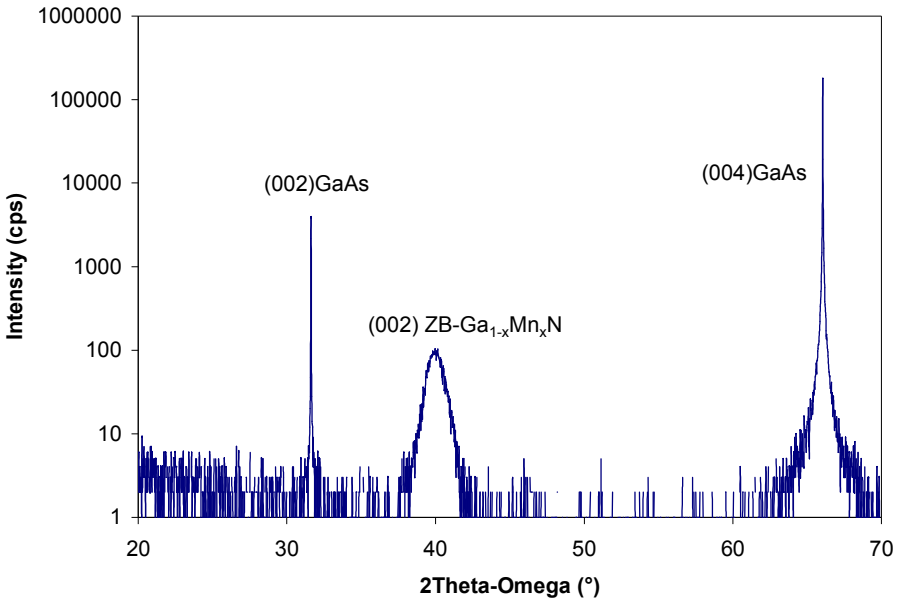

Figure 5.1 2θ-Ω X-ray diffraction profile of sample M4 grown under the highest Mn flux and a slightly N-rich condition, indicating that the epilayer is single phase zinc-blende GaMnN, without evidence for any extra peaks from additional phases.

A representative XRD spectrum obtained from sample M4 using a simple 2θ-Ω scanning mode is presented in Figure 5.1, indicating that the epilayer is single phase zinc-blende GaMnN. It is noted that even for this sample grown under highest Mn flux, there are no additional peaks attributable to any second phase material.

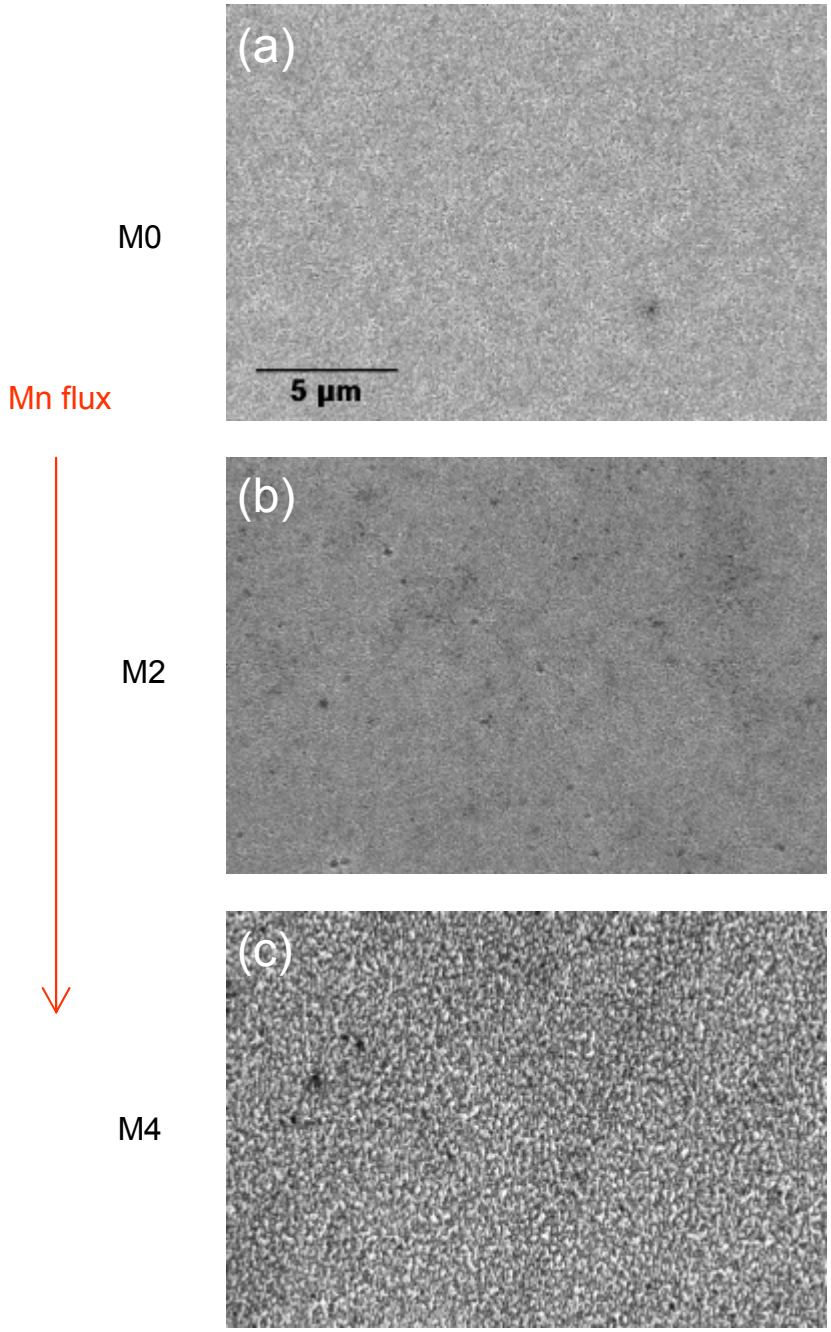

Figure 5.2 SE images of GaMnN grown (a) without Mn presence (sample M0), (b) under low Mn flux (sample M2) and (c) under the highest Mn flux (sample M4), indicating the surfaces of this sample set became increasingly rough with increasing Mn flux.

The surface morphology of this sample set was observed using SEM. The two pictures shown in Figures 5.2a,b depict relatively smooth surfaces of samples M0 and M2, grown in the absence of Mn and under low Mn flux, respectively, whilst the sample grown under the highest Mn flux exhibited a fine-grained structure with an increased surface roughness, indicative of a change in growth mode as a result of the involvement of high-concentrations of Mn during growth.

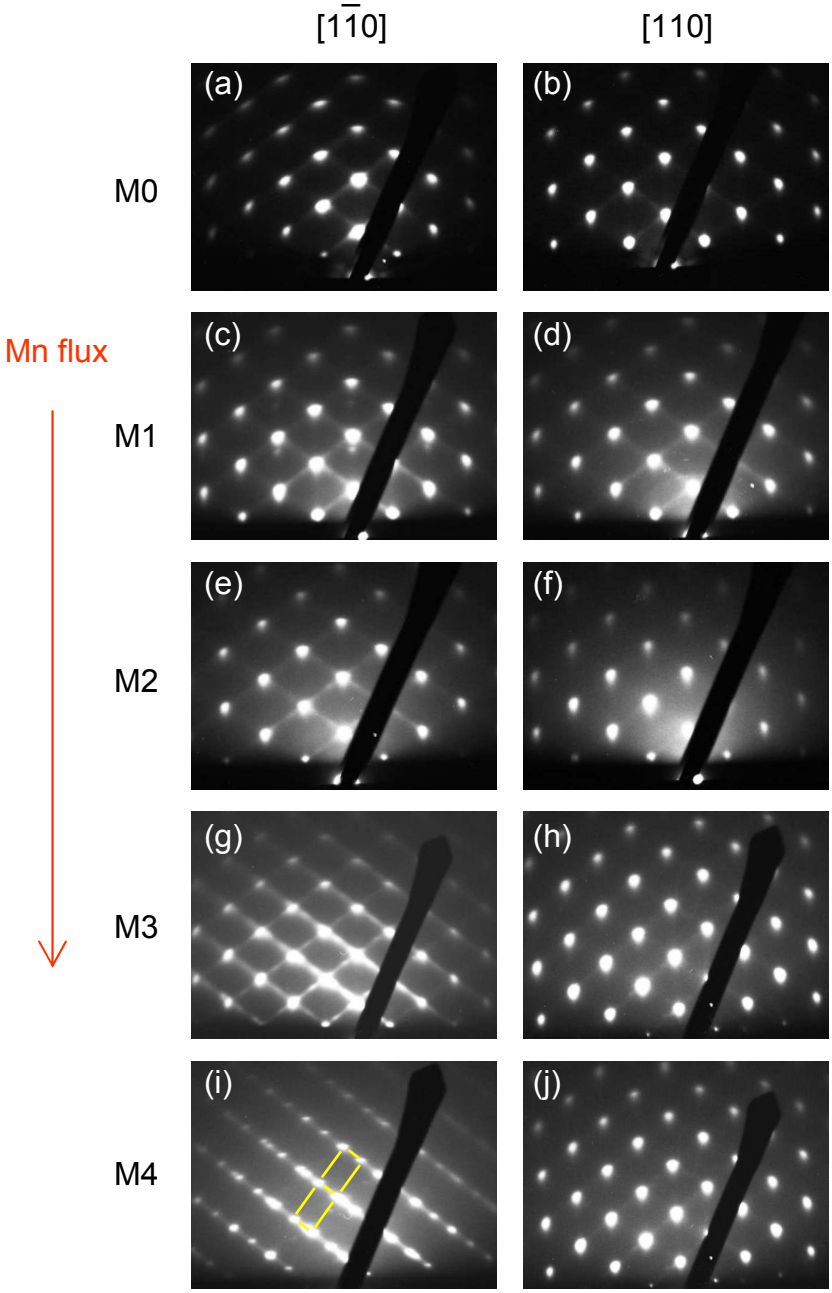

Figure 5.3 200 kV RHEED patterns for GaMnN, (a,b) sample M0, (c,d) sample M1, (e,f) sample M2, (g,h) sample M3 and (i,j) sample M4, recorded along orthogonal <110> projections, demonstrating a transition from single crystal cubic phase growth without Mn presence and under low Mn flux, to mixed cubic / hexagonal phase growth under high Mn flux. Increasing levels of anisotropy along these two projections with increasing Mn flux is also apparent.

RHEED patterns of this sample set recorded along orthogonal <110> projections are presented in Figure 5.3. A transition from single phase cubic growth in the absence of Mn (sample M0) and under low Mn flux (samples M1 and M2) to cubic / hexagonal

mixed phase growth under high Mn flux (samples M3 and M4) was observed. Increasing levels of anisotropy along the two orthogonal <110> projections was also apparent with increasing Mn content.

By way of clarification, as shown in Figures 5.3a,b for sample M0 grown in the absence of Mn, clear, sharp spots were observed for both <110> orthogonal projections, indicative of single phase cubic growth of the GaMnN layer on GaAs(001). Intermediate levels of Mn flux (samples M1 and M2) lead to the appearance of additional faint streaks along <111> directions for both orthogonal projections due to the formation of high densities of stacking faults on inclined {111} planes. For these three samples, no obvious anisotropy along the orthogonal <110> projections was detected. Further, as the Mn flux increased to 4.95×10^{-9} mbar (sample M3), along the $[1\bar{1}0]$ projection, the intensity of these streaks (Figure 5.3g) becomes stronger and additional spots from hexagonal GaMnN also slightly appear. For sample M4 grown under the highest Mn flux, these additional spots become strongest with streaks displaced nearly completely. Hence, a strong anisotropy is apparent evidenced by the overlapping of diffraction spots from both cubic and hexagonal GaMnN along the $[1\bar{1}0]$ projection, with only clear, sharp diffraction spots from cubic GaMnN along the [110] projection. Overall, the Mn flux facilitates the formation of stacking disorders on inclined {111} planes, with high levels of Mn flux leading to the more extreme condition of mixed phase cubic / hexagonal growth.

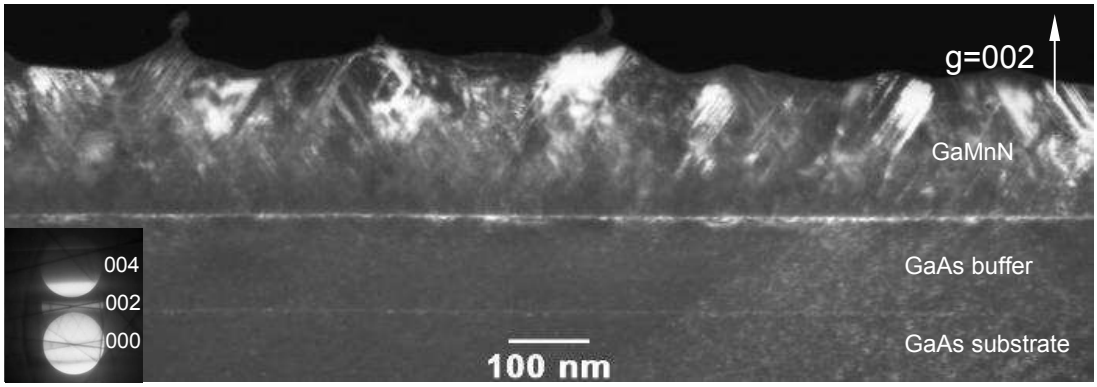

Figure 5.4 002 two beam dark field image of sample M1 in the $[1\bar{1}0]$ projection showing cubic epitaxy.

TEM investigations across the sample set demonstrated the presence of highly faulted defect microstructures in all the specimens. By way of illustration, Figures 5.4 and 5.5 present 002 two beam, dark field, cross-sectional TEM images for samples M1 and M4, respectively. It is noted that the bright line delineated at the position of the GaMnN/GaAs interface in both figures is tentatively attributed to scattering from remnant oxide and/or small nucleation grains. Sample M1 with a layer thickness of ~200 nm has a relatively flat growth surface, indicating a relatively steady growth mode under conditions of low Mn flux. The typical feature of a high density of stacking faults on inclined {111} planes for zinc-blende GaN grown on these cubic GaAs substrates is also shown in this sample.

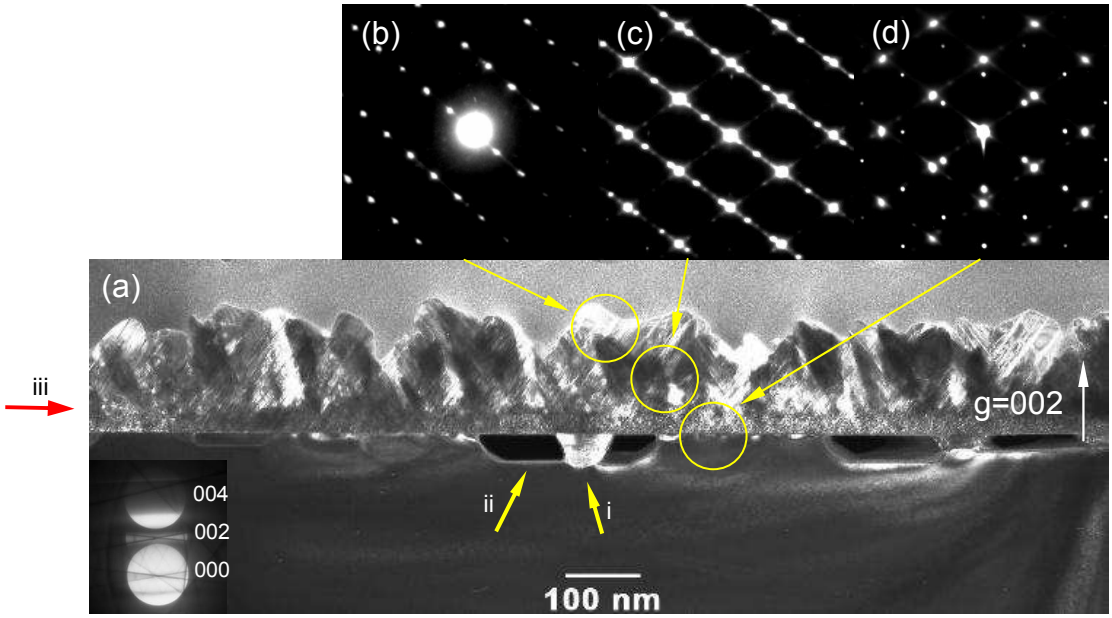

Figure 5.5 (a) 002 two beam, dark field image of sample M4 in the $[1\bar{1}0]$ projection showing a rough growth surface and mixed phase growth. Inclusions and associated voids in the substrate, and an initial nucleation layer are arrowed i, ii and iii, respectively. The inset CBED pattern confirms the sample polarity of being $[1\bar{1}0]$. (b-d) Associated SAED patterns recorded from different positions across the epilayer of this sample. (b) $[11\bar{2}0]$ diffraction pattern from a hexagonal grain at the sample surface; (c) overlapping diffraction patterns from zinc-blende and wurtzite grains in the bulk of the sample; and (d) sharp diffraction spots associated with the zinc-blende nucleation layer and the GaAs substrate confirming the cubic epitaxy of the initial nucleation layer of GaMnN on GaAs(001).

However, a very rough growth surface and a large variation in epilayer thickness from ~100 nm to 200 nm are observed for sample M4. Inclusions (arrowed i) at the interface extending into the GaAs buffer layer and associated voids (arrowed ii) were also observed. Further, a distinct nucleation layer of 40 to 50 nm in thickness (arrowed iii) and columnar grains on top of this layer were revealed. Selected area electron diffraction (SAED) and diffraction contrast imaging experiments were performed to clarify the distribution of phases throughout this sample. Three SAED patterns recorded at the sample surface, in the bulk and at the GaMnN/GaAs(001) interface are illustrated in Figure 5.5b,c and d, respectively. It is confirmed that the initial GaMnN nucleation layer is single cubic material with accurate epitaxial relationship with respect to the GaAs(001) substrate $((001)_{GaMnN}$ // $(001)_{GaAs}$ and

$[110]_{GaMnN}$ // $[110]_{GaAs}$). The development of stacking faults propagating on inclined {111} planes in this layer is also evidenced by faint streaks along <111> directions in Figure 5.5d, as compared with sharp and clean diffraction spots from the GaAs substrate. The layer then changes growth mode from single cubic phase growth to mixed phase cubic and hexagonal growth, taking the form of columnar grains. As shown in Figure 5.5c, overlapping diffraction spots from both cubic and hexagonal GaMnN together with streaks along <111> directions were established, confirming the mixed phase growth and the formation of high density of stacking faults on inclined close packed planes. Evidence from dark field images obtained using diffraction spots only attributable to hexagonal phase material, as distinct from spots from cubic microtwins, was obtained with columnar hexagonal grains extending from the initial nucleation layer towards the epilayer surface being highlighted, rather than just being associated with the epilayer surface due to a cool down effect at the end of growth, as identified for highly N-rich (low Mn content) growth conditions in Chapter Four.

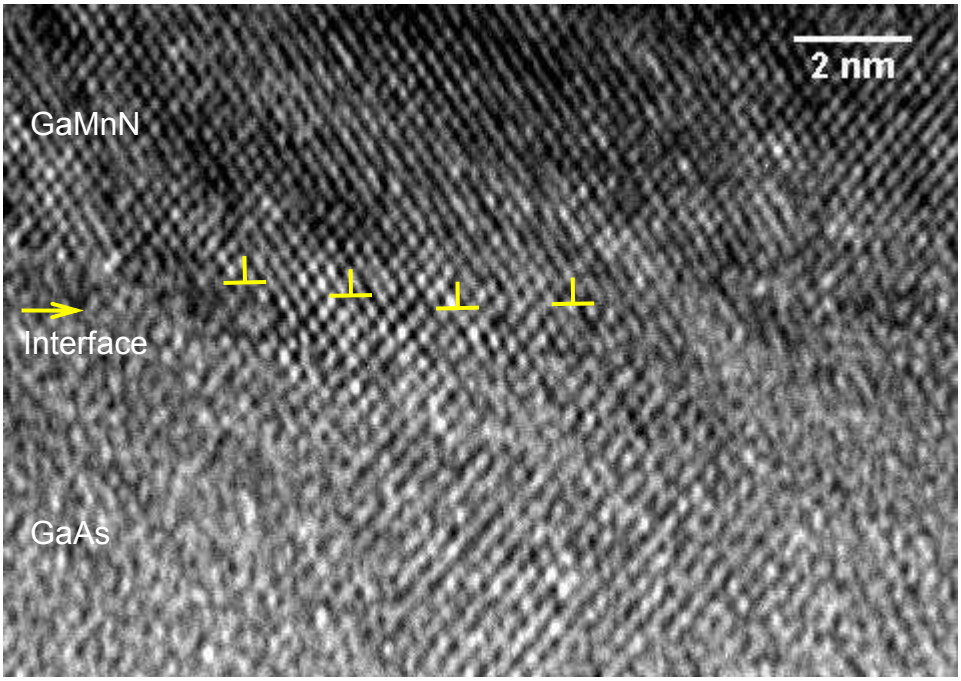

Figure 5.6 Cross-sectional HREM image of sample M4 taken along the $[1\bar{1}0]$ direction showing the GaMnN and GaAs interface and an array of 60° misfit dislocations

Thin regions within this TEM sample foil also provided an opportunity for the direct observation of the GaMnN microstructure at the atomic level using high resolution TEM. A HREM micrograph showing the GaMnN/GaAs interface in the [110] projection is presented in Figure 5.6. Due to the difference in hardness of GaMnN and GaAs, it is seen that a large part of GaAs layer became damaged during the ion beam milling process, resulting in blurring of the interface in some regions, with no recognisable atomic arrangement. For the limited region showing clear lattice fringes for both the GaMnN and GaAs, the interface appears to be flat on the atomic scale with an overall interfacial roughness of only a few mono layers, suggesting a clean, well controlled growth process at the nucleation stage. The GaMnN layer is plastically relaxed by the formation of edge type misfit dislocations without further propagation. Since the lattice mismatch between GaN and GaAs is $(a_{GaAs} - a_{GaN}) / a_{GaAs} = (5.65 - 4.52) / 5.65 = 20\%$ with regard to the GaAs, it is not surprising to see

that such a large mismatch is compensated by an array of edge dislocations with a period of every five GaN lattice planes.

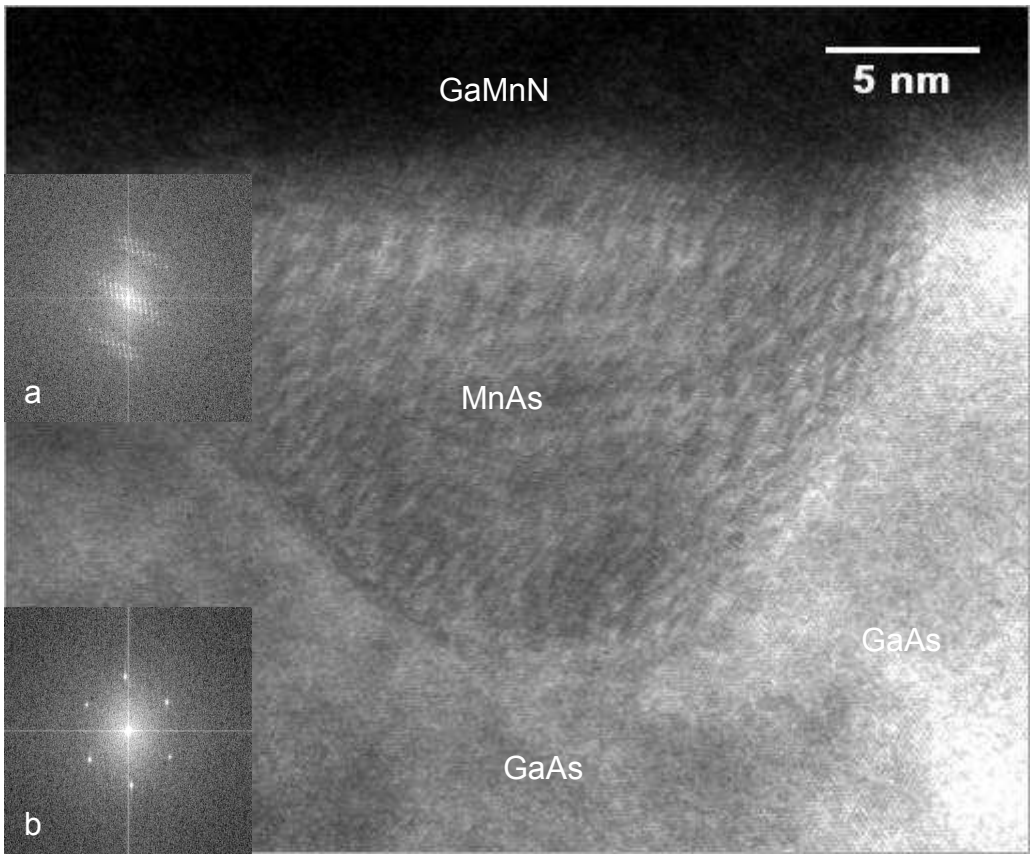

Figure 5.7 TEM micrograph obtained at the GaMnN GaAs interface, showing a MnAs inclusion with FFT inset for (a) MnAs and (b) GaAs

EFTEM and convergent beam electron diffraction were performed to appraise a MnAs inclusion, extending into the GaAs buffer layer, as shown in Figure 5.7 with diffraction patterns obtained from fast Fourier transforms (FFT) of (a) MnAs and (b) GaAs inset. A distinct interface between these two phases is indicated, further supported by the chemical content images of Figure 5.8. It is noted that no associated voids beside this inclusion are present in this case.

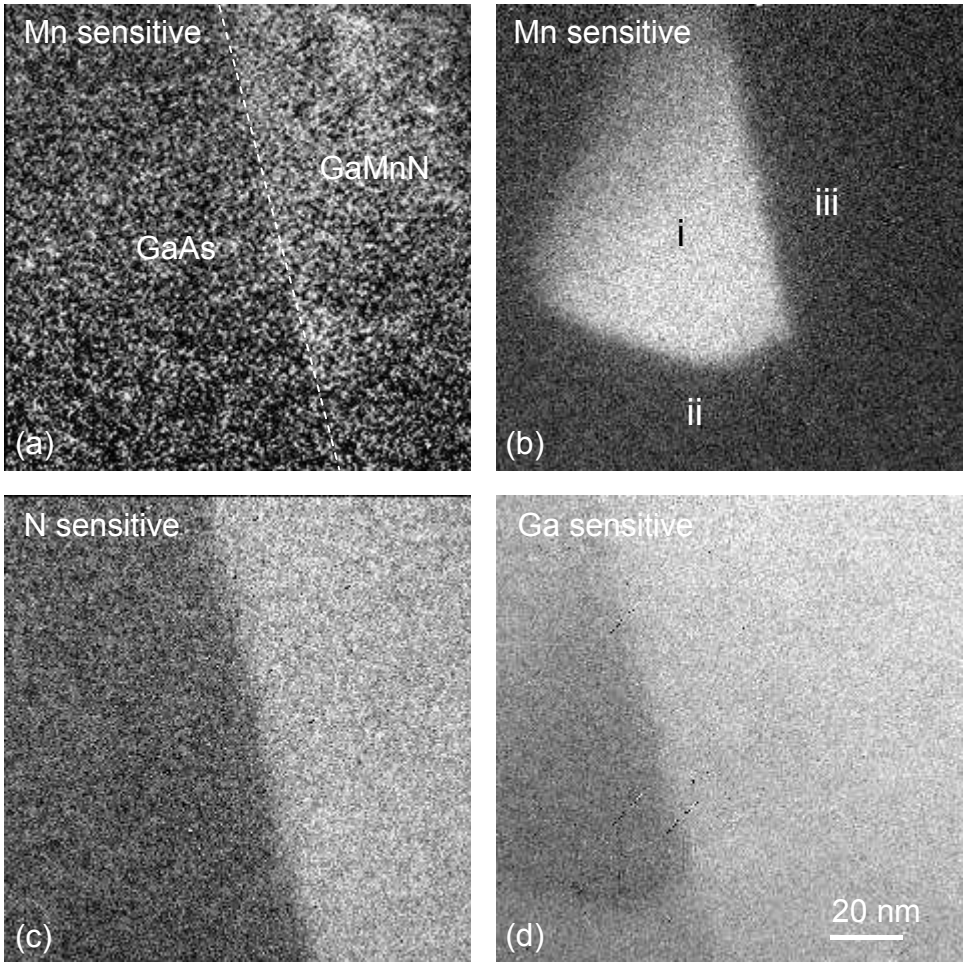

Figure 5.8 EFTEM images, (a) Mn sensitive image taken from a GaMnN/GaAs interface in a region without MnAs inclusions showing contrast due to the Mn incorporation in GaN. (b) Mn sensitive, (c) N sensitive and (d) Ga sensitive images taken from the GaMnN/GaAs interface in a region with an MnAs inclusion. Labelled regions in (b) are (i) MnAs inclusion, (ii) GaAs substrate and (iii) GaMnN.

Elementally sensitive images acquired from the same region as Figure 5.7 were obtained using energy filtered TEM (EFTEM), as shown in Figure 5.8[7]. It is noted that beam flicker during the acquisition of the EFTEM series from 1000 eV upwards made As mapping unreliable. However, contrast between the GaMnN and the GaAs substrate in the Mn sensitive image taken from the interface in a region without MnAs inclusions provides evidence for the incorporation of Mn into the GaMnN layer. In

[7] The EFTEM and HREM work was carried out by MW Fay, part of which was obtained at the University of Sheffield.

comparison, high levels of Mn were observed in the region containing a MnAs inclusion, with a depletion of Ga and N, confirming that these inclusions are indeed Mn-rich.

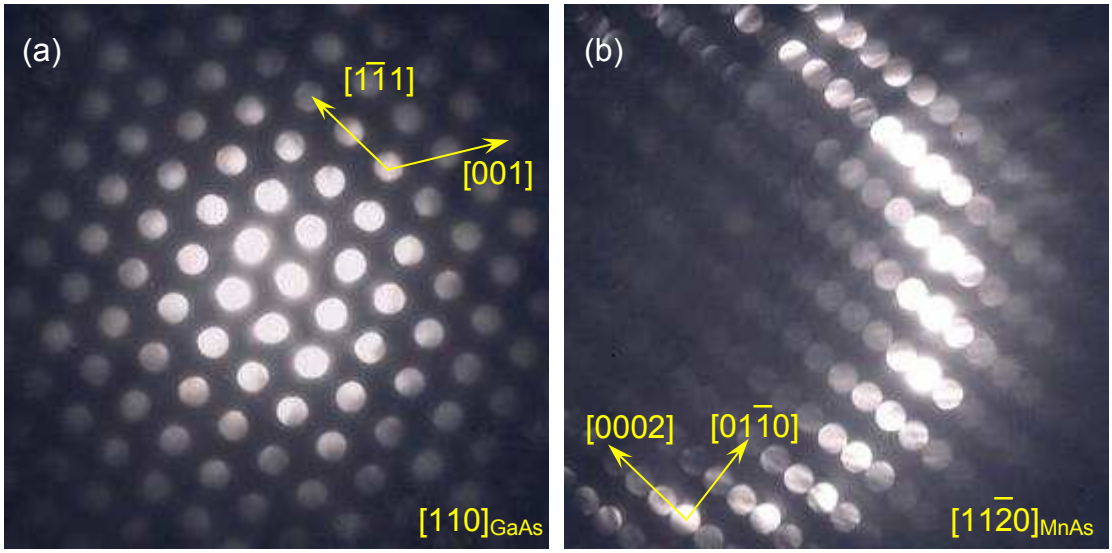

Figure 5.9 Convergent beam electron diffraction patterns obtained from (a) the GaAs substrate and (b) a MnAs inclusion along the $[110]_{GaAs}$ zone axis.

Considering the sizes of these MnAs inclusions and the limited size of selected area apertures within a TEM, it was generally found to use selected area electron diffraction to establish appropriate diffraction conditions for the purpose of identifying such second phase precipitates. The Jeol 4000fx TEM was employed for convergent-beam electron diffraction for the assessment of very small precipitates, making use of its ability to focus the electron beam down to a very small probe. CBED patterns obtained from the GaAs substrate and a MnAs inclusion along the $[110]_{GaAs}$ zone axis are presented in Figures 5.9a and b, respectively. The symmetry and calculated lattice parameters are consistent with the precise indexing of MnAs inclusions detailed in Chapter Four. Therefore, combining the evidence from EFTEM

and CBED, MnAs inclusions precipitated at the GaMnN and GaAs interface were again confirmed to be a typical feature of the direct growth of GaMnN on GaAs(001).

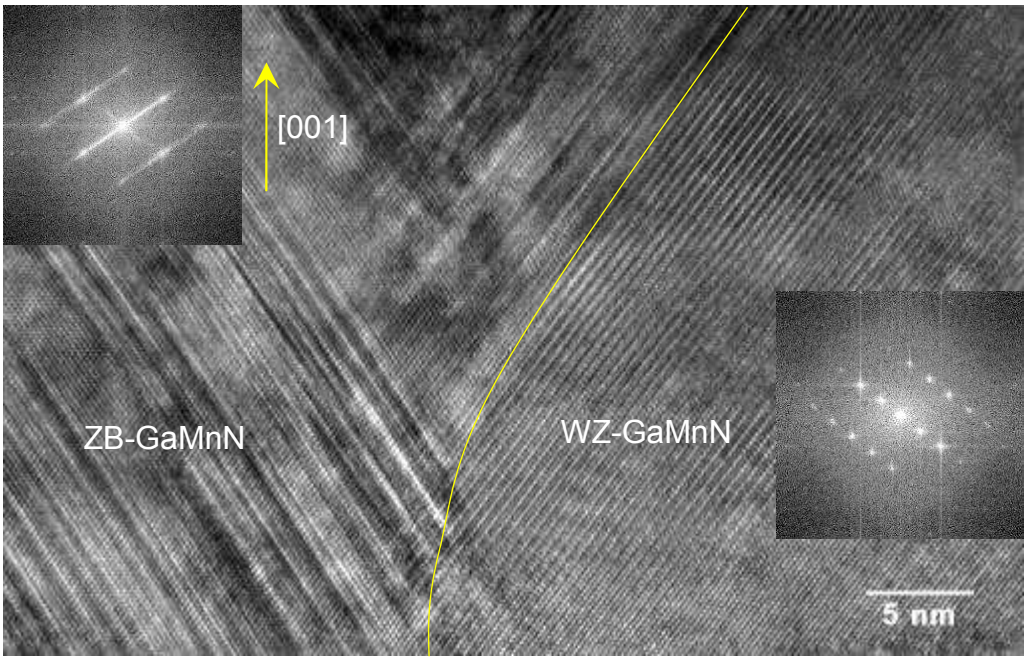

Figure 5.10 HREM image obtained from the bulk of sample M4 along the $[1\bar{1}0]$ zone axis showing an interface between zinc-blende and wurtzite GaMnN columnar grains with corresponding FFT patterns inset.

As the observation region was moved from the GaMnN GaAs interface to the bulk of the sample, boundaries between columnar cubic and hexagonal grains are commonly found. A representative HREM image with corresponding FFT patterns inset confirming the α/β phase compositions is shown in Figure 5.10. Clearly, the presence of a high density of stacking faults propagating on inclined {111} planes is identified as being a typical feature for zinc-blende grains, whilst the hexagonal GaMnN grains display a well-defined crystal structure.

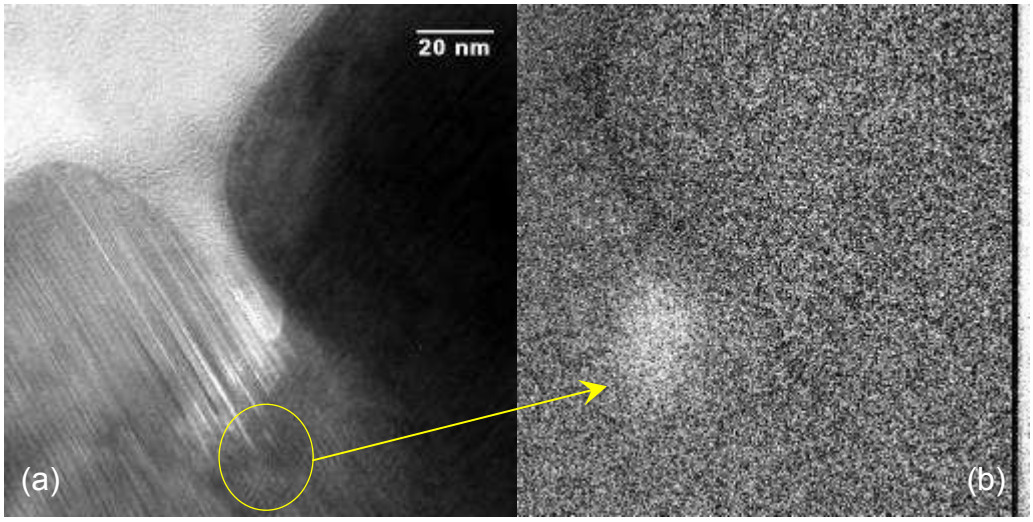

Figure 5.11 (a) TEM image of sample M4 taken in a region containing a Mn-rich precipitate (circled) with the corresponding area highlighted in the (b) Mn-sensitive EFTEM image.

In order to examine the probability of the formation of Mn-rich nano-clusters within the GaMnN lattice of sample M4, EFTEM was performed, especially across the Mn-edge for Mn-sensitive images. Figure 5.11a shows a TEM image taken from a region containing a Mn-rich precipitate with the corresponding location revealed in the Mn-sensitive EFTEM image (Figure 5.11b), following shift correction and background subtraction.

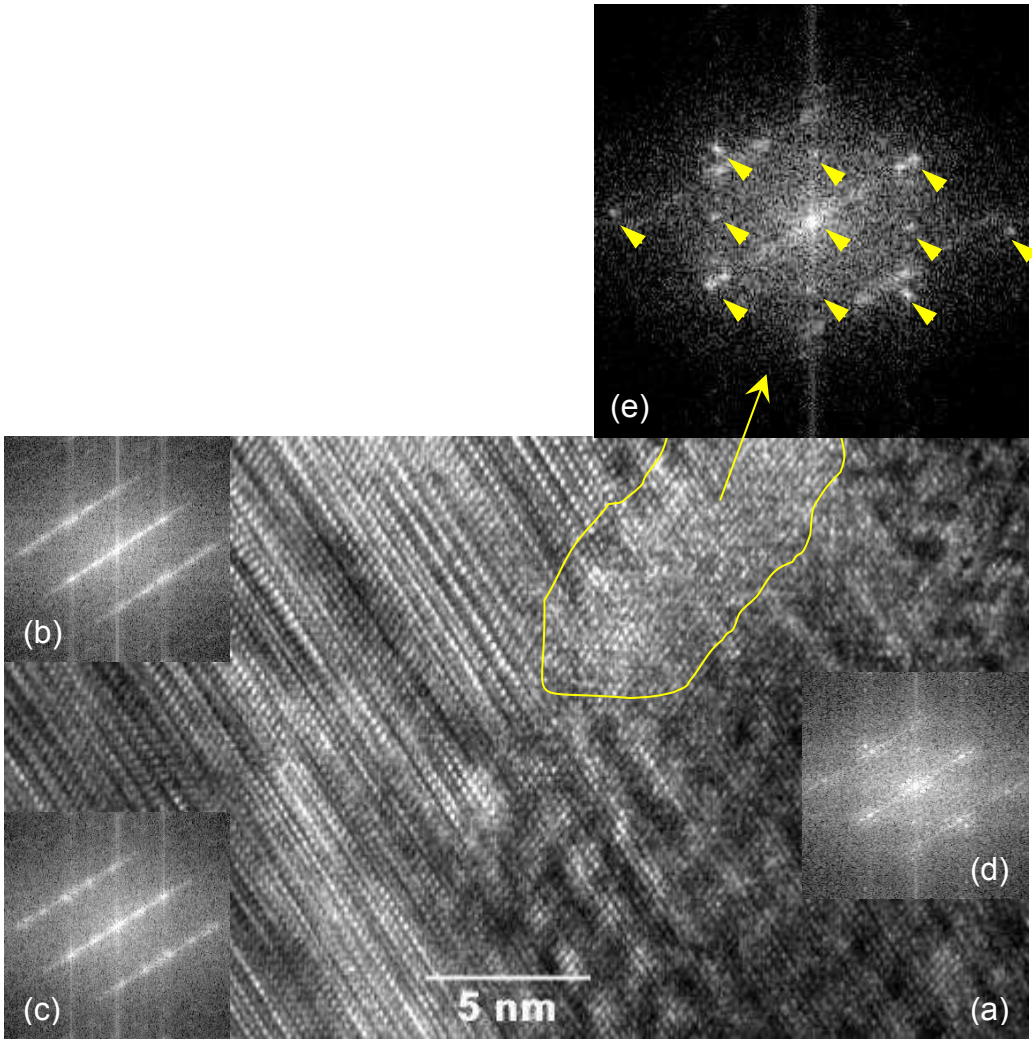

Figure 5.12 (a) HREM image of sample M4 recorded at the boundary of a cubic and a hexagonal grain, with FFT patterns inset confirming regions of (b) mixed phase cubic and hexagonal GaMnN, (c) hexagonal GaMnN and (d) cubic GaMnN. (e) FFT pattern containing additional diffraction spots obtained from the circled region in (a) denoting a lattice symmetry distinct from both cubic and hexagonal GaMnN, suggests the precipitation of a Mn-rich nano-cluster at the grain boundary.

Once the variation in chemical composition is shown in Figure 5.11b was observed, the TEM was immediately switched to the high-resolution mode in order to obtain crystallographic information from precisely the same region. Figure 5.12a presents a HREM image obtained from the circled region in Figure 5.11a. FFT patterns inset are obtained across this boundary, again revealing differing phase compositions at different locations. By way of example, strong streaks along <111> directions plus faint extra spots from the hexagonal phase are apparent in Figure 5.12b, indicative of

a high density of stacking faults in cubic GaMnN with a small amount of hexagonal phase embedded. Further, these extra spots became dominant in Figure 5.12c confirming this region in the lower left corner of this image to be hexagonal GaMnN, whilst the right hand side of Figure 5.12a is found to be cubic, as indicated by Figure 5.12d. In particular, as distinct from the typical features of α/βphase separation in this sample, a region of ~5 nm in size located at the grain boundary of two phases was identified to be of strong interest. In addition to the spots from the cubic GaMnN, there are also symmetric extra spots in the associated FFT pattern (Figure 5.12e) recorded over this region, being distinct from the typical patterns for both the <110> zone axis of cubic GaMnN and the $[11\bar{2}0]$ zone axis for hexagonal GaMnN. An attempt was made to index these extra spots, with the zone axis diffraction data for either the cubic or hexagonal GaMnN removed. Therefore, according to the fine detailed analysis of this particular region using complementary HREM and EFTEM techniques, the region in this case is considered to be an example of a Mn-rich nano precipitate, not detected previously by XRD or SAED.

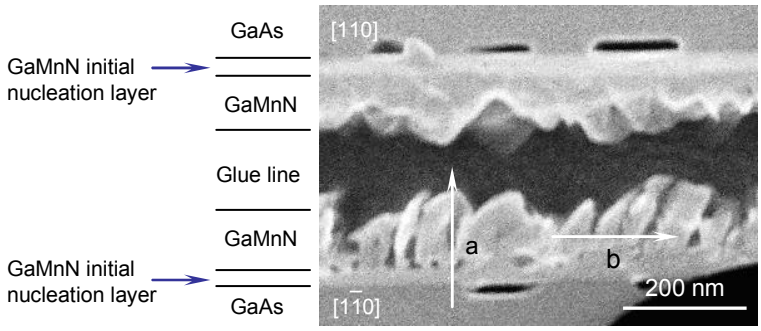

Figure 5.13 SE image of sample M4 obtained using the Jeol 2000fx TEM/STEM. Clear columnar grains are revealed for the $[1\bar{1}0]$ projection, whilst a more uniform film coverage is observed in the [110] projection. EDX line profiles were acquired with the electron beam scanned parallel (arrowed by a) or perpendicular (arrowed by b) to the GaMnN and GaAs interface on the $[1\bar{1}0]$ side.

A secondary electron image for sample M4 (Figure 5.13), corresponding to orthogonal <110> projections for both sides of the TEM specimen, was generated using the Jeol 2000fx TEM/STEM. The $[1\bar{1}0]$ sample projection demonstrated the presence of columnar grains on top of the initial GaMnN nucleation layer, while the [110] sample projection demonstrated a more continuous grain structure. A rough growth surface was revealed for both sides. Such anisotropy suggests that most of the grains were preferentially elongated along the $[1\bar{1}0]$ direction, rather than [110] direction, implying a dramatic change in the growth mode under high Mn flux.

The Mn incorporation in sample M4 was also assessed using EDX. With reference to the SE image of Figure 5.13, EDX line profiles with the electron beam scanned perpendicular and parallel to the GaMnN/GaAs interface in the $[1\bar{1}0]$ projection are presented in Figures 5.14a and b, respectively. The perpendicular scan (Figure 5.13a), demonstrated an increasing Mn concentration from ~5 to over 25 at% with increasing GaMnN layer thickness, suggesting an accumulation of Mn as the growth progresses as a result of the large amount of incoming Mn exceeding the Mn solid solubility within GaN combined with a surfactant effect. For the parallel scan, a significant jump in the Mn content from ~4 up to over 25 at% is detected (Figure 5.14b), whilst the Mn is uniformly distributed in the majority of the sample at a level of ~5 at%.

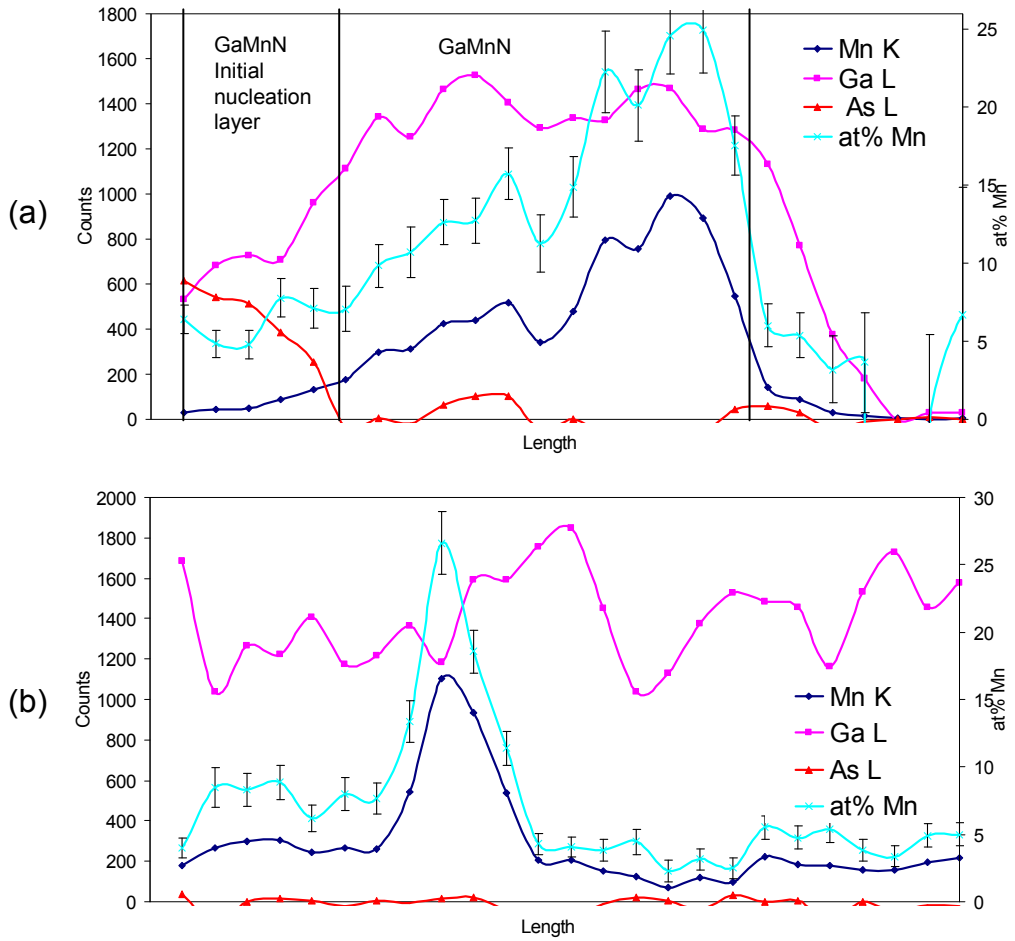

Figure 5.14 EDX line profiles with the electron beam scanned (a) perpendicular and (b) parallel to the GaMnN/GaAs interface (Figure 5.13). Note: the Mn concentration is calculated by assuming Mn atoms within GaMnN lattice only occupy the Ga sites (not corrected for variations in sample thickness).

Electrical measurement of resistivity, Hall coefficient, hole concentration and mobility were performed on this sample set with the results listed in Table 5.2[8]. There is no obvious trend in these measured properties with respect to the increasing Mn flux. However, for sample M4 containing the highest Mn content, the layer appears metallic, with a dramatic drop in resistivity and a big increase in mobility being observed.

[8] The electrical property measurements were carried out by Kevin Edmonds in the School of Physical and Astronomy.

Table 5.2 Results of electric measurement of this sample set.

Sample	Mn flux/ $\times 10^{-9}$ mbar	Estimated Mn concentration from SIMS/ at%	ρ (Ω·cm)	R_{Hall} (Ω/T)	p_{Hall} (cm^{-3}) (sheet density divided by thickness in cm to get volume density)	μ_{Hall} ($cm^2V^{-1}s^{-1}$)
M0	0.000	-	-	-	-	-
M1	0.495	0.04	0.17	4.5	4.00×10^{18}	8
M2	1.650	0.22	8.40	783.3	2.60×10^{16}	28
M3	4.950	1.0	1.30	778.9	2.70×10^{16}	78
M4	25.000	6.6	0.02	23.5	8.86×10^{17}	289

5.3 Discussion

It is noted that a full discussion of the growth of these GaMnN/GaAs(001) with increasing Mn flux will be given in Chapter Seven. Briefly, it is considered that a high concentration of Mn on the growth surface has a dominant effect on development of GaMnN microstructure, reducing the mobility of Ga atoms on the growth surface, resulting in an anisotropic growth or even mixed phase columnar growth under the highest Mn flux. The revelation of a Mn-rich precipitate by EFTEM suggests that Mn-rich nano-clusters may exist within samples with low Mn concentrations, being considered to be closely connected with sample bulk functional properties.

5.4 Summary

GaMnN epilayers grown on GaAs(001) substrates by PAMBE as a function of Mn flux have been assessed using a variety of structural characterisation techniques. Increasing Mn flux is associated with the build up of a Mn surfactant layer during the early states of growth and a transition from zinc-blende single phase growth to zinc-blende/wurtzite mixed phase growth. The Mn surfactant effect is suggested under high Mn-flux during growth of GaMnN. The sample grown under the highest Mn-flux was mainly investigated. Combining the information from both HREM and EFTEM, a Mn-rich inclusion with distinct lattice structure located at the grain boundary

between a cubic and a hexagonal grain was found and suggested to be a general case for samples with high Mn-concentration.

CHAPTER SIX

Microstructural characterisation of GaMnN on GaAs(001) grown by plasma-assisted MBE as a functional of temperature

6.1 Introduction

Experimentally, it is found that Mn can only be incorporated into the GaN lattice under N-rich conditions [69,72], whilst growth under Ga-rich conditions is associated with a slightly improved epilayer microstructure as presented in Chapter Four. It is suggested that under N-rich conditions, Mn also exhibits a surfactant effect on the GaMnN growth front with its surface accumulation, under conditions of high Mn flux, favoring a mixed cubic and hexagonal phase growth mode as described in Chapter Five. Also, due to the limited solid solubility of Mn within GaN, Mn-rich nano-precipitates with distinct atomic arrangement are found by EFTEM and HREM. It is therefore apparent that new growth routes need to be explored for the purpose of establishing uniform p-type GaMnN alloys.

In this chapter, GaMnN on GaAs(001) substrates grown under Ga and N-rich conditions, respectively, at temperatures from 680°C down to 186°C are characterised. Such low temperatures well below the normal GaN growth temperature

allow the investigation of enhanced Mn incorporation under nominally Ga-rich growth conditions. The growth details are listed in Table 6.1.

Table 6.1 Details of the growth of GaMnN layers on GaAs(001) substrates as a function of growth temperature, under slightly Ga-rich and N-rich conditions.

No.	Tg / °C	Ga flux / $\times 10^{-7}$mbar	Mn flux / $\times 10^{-8}$mbar	Growth condition	Mn at% obtained by EDX
M0	680	2	0	N-rich	0
N680	680	2	10	N-rich	~1.8 (estimated by MBE)
N597	597	2	10	N-rich	-
N443	443	2	10	N-rich	~5.0
N265	265	2	10	N-rich	-
N186	186	2	10	N-rich	-
G680	680	6.6	10	Ga-rich	-
G507	507	6.6	10	Ga-rich	-
G340	340	6.6	10	Ga-rich	~1.5-2.0
G265	265	6.6	10	Ga-rich	~2.5-4.5
G186	186	6.6	10	Ga-rich	-

Note: Where the notation Nxxx or Gxxx refers to N-rich or Ga-rich growth conditions and a growth temperature of xxx°C, respectively.

6.2 Results

6.2.1 GaMnN growth under N-rich conditions, as a function of growth temperature

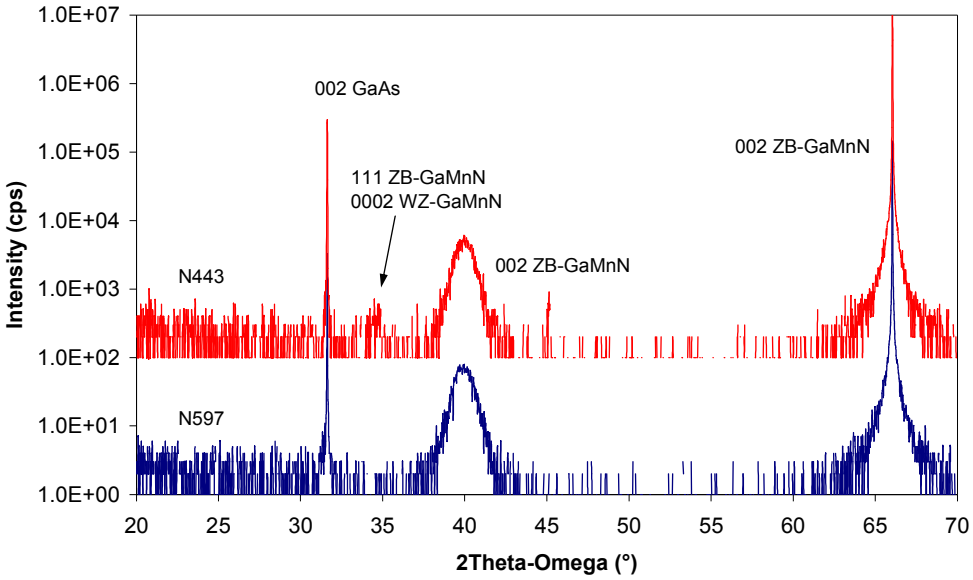

Figure 6.1 2θ-Ω X-ray diffraction profiles of samples N597 and N443 grown under N-rich conditions at 597°C and 443°C, respectively. The extra peak emerging at 443°C is considered to be due to the presence of randomly oriented cubic and hexagonal GaMnN grains. Note: The two XRD spectra are simply offset in this figure by multiplying the spectrum of sample N443 by 100 in order to highlight the structural evolution with decreasing growth temperature under such N-rich conditions.

Samples were initially examined by XRD using the simple 2θ-Ω scanning mode. Two representative XRD spectra are selected and plotted together in Figure 6.1 to illustrate the microstructural evolution of this sample set as a function of growth temperature. For samples grown at and above 597°C, no extra peaks besides the 002 reflection from zinc-blende GaMnN were detected, suggesting the formation of epitaxial cubic GaMnN with respect to the GaAs(001) substrate under such growth conditions. In comparison, for samples grown at 443°C and below, an additional peak located at about 34~35° became apparent. The corresponding lattice spacing calculated is

consistent with that of {111} planes for cubic and {0002} planes for hexagonal GaMnN, being 2.61 Å and 2.59 Å, respectively. Since the 2θ-Ω scan mode employed here can only pick up reflections from lattice planes parallel to the growth surface, without e.g. considering the possible presence of Mn-rich precipitates within the GaMnN lattice, this peak can only be considered to be a possible joint contribution of both polycrystalline cubic or/and hexagonal GaMnN.

Secondary electron (SE) images of the surfaces of as-grown samples N680, N443 and N186 are shown in Figures 6.2a-c. Sample N680 exhibits a comparatively rough surface which is characteristic for N-rich conditions at 680°C. The surface morphology is improved for sample N443 and becomes smoothest for sample N186, grown at the lowest temperature examined.

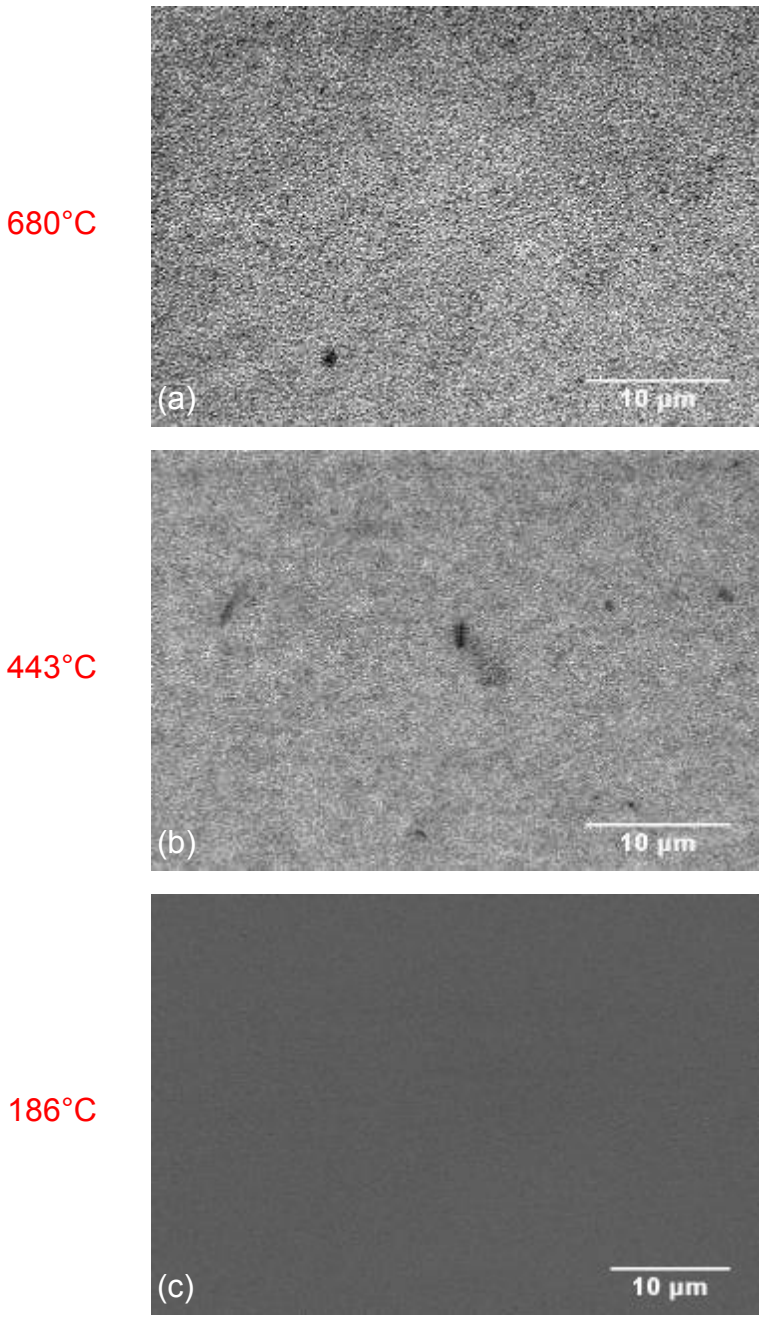

Figure 6.2 Secondary electron images of GaMnN samples grown under N-rich conditions at (a) 680°C, (b) 443°C and (c) 186°C.

RHEED was performed across the sample set in order to select samples for the purpose of more detailed conventional TEM examination. Patterns of a sample grown at 680°C under the same Ga/N ratio but in the absence of Mn (sample M0) are also shown for comparison. Clear and sharp spots with faint streaks along both orthogonal <110> projections are obtained, suggesting a well defined microstructure for this

epitaxial GaN layer (Figure 6.3a,b). Figures 6.3c-i show a sequence of RHEED patterns illustrating a transformation of the as-grown GaMnN surface microstructure with decreasing growth temperature. RHEED patterns for the sample grown at 680°C and 597°C suggest a predominant cubic epitaxy but with a strong anisotropy with respect to the two orthogonal <110> projections. By way of example, along the <110> projection, diffraction spots in Figure 6.3c are sharp and distinct indicative of a rough growth surface (Figures 6.3c), whilst along the $<1\bar{1}0>$ projection, additional streaks along a <111> direction were apparent, being evidence for the formation of this planar defects predominantly on inclined {111} planes. Also, two types of extra spots need to be clarified: emerging spots in Figure 6.3c which become stronger in Figure 6.3e and additional strong spots along <111> directions are all attributed to the presence of hexagonal GaMnN, but with a different orientation relationship with respect to the predominant cubic GaMnN. At growth temperatures of 443°C and below, the samples become polycrystalline (Figures 6.3g-i) with an indication of slightly preferred orientation at 443°C transforming to much finer grained polycrystalline material at 186°C, as evidenced by the more continuous diffraction rings. Only one representative RHEED pattern is presented in these three cases due to the lack of dominant zone axis diffraction conditions, as the sample was rotated about the growth axis. Indexing of Figure 6.3i confirmed the sample grown at the lowest temperature of 186°C comprised mixed phase cubic and hexagonal GaMnN.

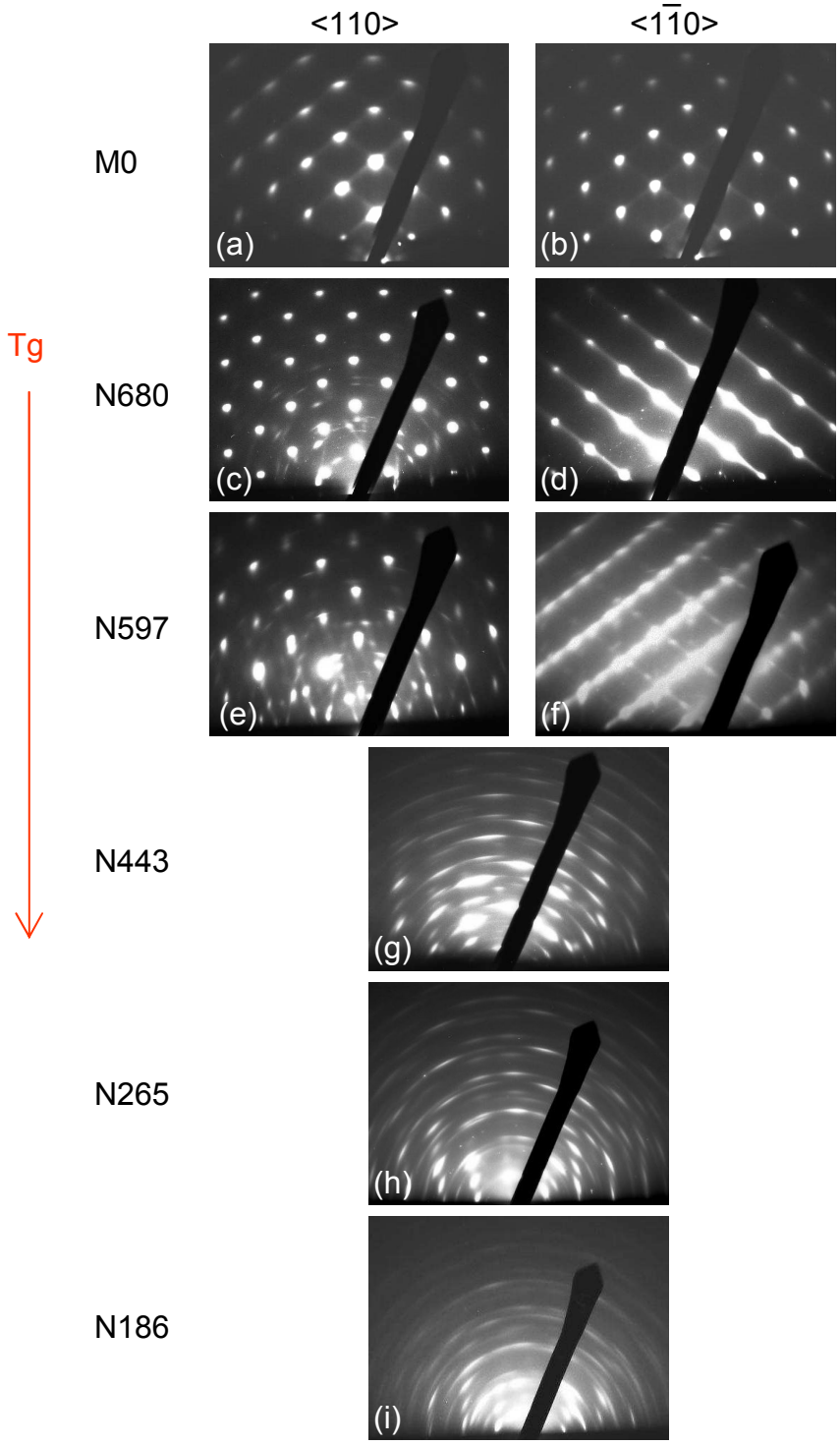

Figure 6.3 RHEED patterns of the near surface microstructures of samples grown under slightly N-rich conditions as a function of temperature. (a,b) Sample M0, (c,d) sample N680 and (e,f) sample N597 recorded along orthogonal <110> projections. (g,h,i) Samples N443, N265 and N186, respectively, indicative of increasing levels of polycrystallinity.

Figure 6.4 shows an 004 dark-field image of sample M0 growth in the absence of Mn under a slightly N-rich condition at 680°C. The GaN epilayer has adopted a precise orientation relationship of $<110>_{GaN}//<110>_{GaAs}$ and $(001)_{GaN}//(001)_{GaAs}$ and exhibits a high density of stacking faults on {111} planes. A similar microstructure for a sample grown at 680°C under a slightly N-rich condition and a low Mn flux is also shown in Figure 5.4 of Chapter Five.

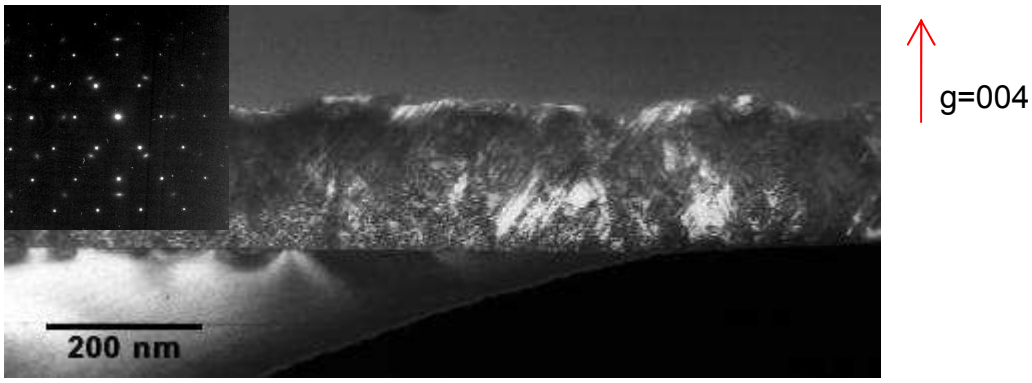

Figure 6.4 Cross sectional 004 two-beam dark-field image of sample M0 grown in the absence of Mn at 680°, showing the epilayer contains a high density of stacking faults on inclined {111} planes.

In comparison, an 004 two-beam dark-field image of a GaMnN layer grown under a slightly N-rich condition at 443°C (sample N443) is presented in Figure 6.5. A relatively uniform initial layer of GaMnN with thickness ~150 nm is confirmed by CBED to be single phase cubic material with the usual epitaxial orientation relationship of $<110>_{GaMnN}//<110>_{GaAs}$ (Figures 6.5b,c). The layer above then adopts a columnar growth mode, with the development of columnar grains of both cubic and hexagonal GaMnN. This is confirmed by SAED (Figure 6.5d) recorded along the $<110>_{GaAs}$ projection over this GaMnN layer, which is dominated by strong diffraction spots from cubic GaMnN, with additional diffraction spots attributed to the development of randomly oriented mixed phase columnar grains.

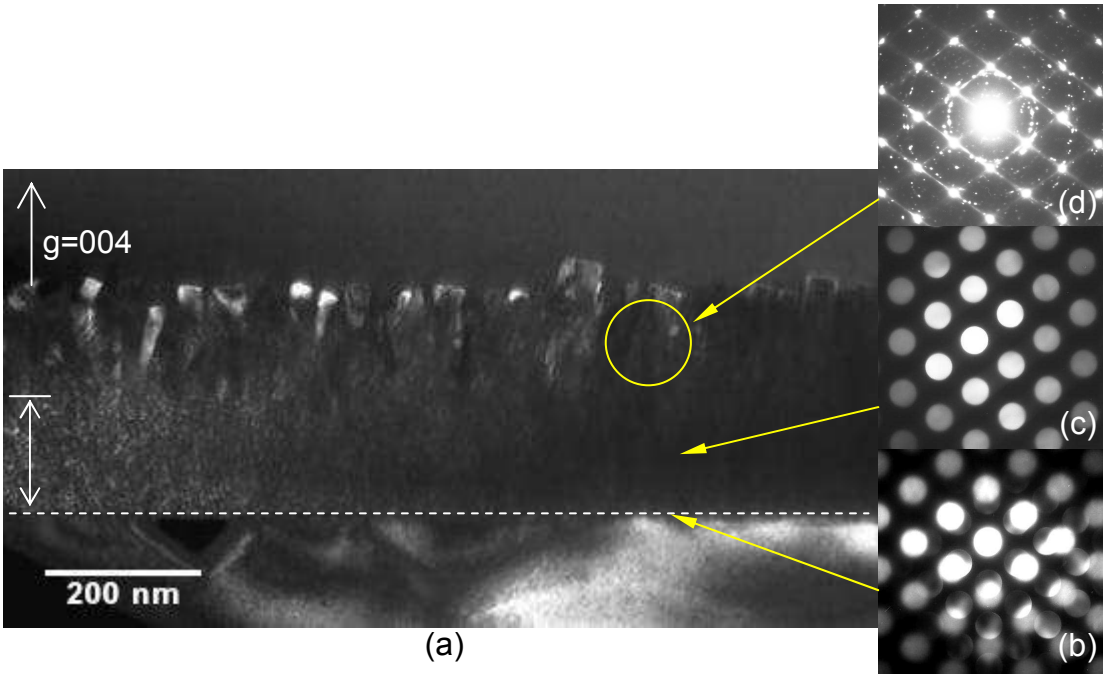

Figure 6.5 (a) Cross sectional 004 two-beam dark-field TEM image of sample N443 showing the formation of columnar grains of cubic and hexagonal GaMnN on top of the initial nucleation layer of cubic GaMnN of thickness of around 150 nm. CBED patterns obtained (b) at the GaMnN/GaAs interface and (c) over the initial GaMnN nucleation layer confirming the initial cubic epitaxy of GaMnN on GaAs(001). (d) A SAED pattern obtained from these GaMnN columnar grains, dominated by strong diffraction spots from cubic GaMnN, with additional diffraction spots attributed to the development of the mixed phase growth columns.

Further, the phase composition of these columnar grains was investigated in detail by acquiring CBED patterns with the electron beam focused onto individual growth columns. Except for Figure 6.6a, showing a typical overlapping of diffraction spots from both cubic and hexagonal GaMnN along $<110>_{\beta}$ and $<1\bar{1}20>_{\alpha}$, respectively, no other example of these low index zone axis diffraction patterns for cubic GaMnN were found during the operation of the Jeol 4000fx. However, several patterns for hexagonal GaMnN along different zone axes were recorded and indexed, suggesting that this low temperature growth layer contains a large number of randomly oriented grains of hexagonal GaMnN. In addition, the precise indexing of Figure 6.5d reveals that besides the well defined diffraction spots from cubic GaMnN, nearly all the extra spots forming rings can be attributed to hexagonal GaMnN with random orientations.

The Mn concentration of this sample was appraised using EDX, indicating a uniform distribution of Mn, of about 5 at%, throughout the epilayer, being higher as compared with that for the sample grown at 680°C, demonstrating an improved incorporation of Mn under such low temperature growth conditions.

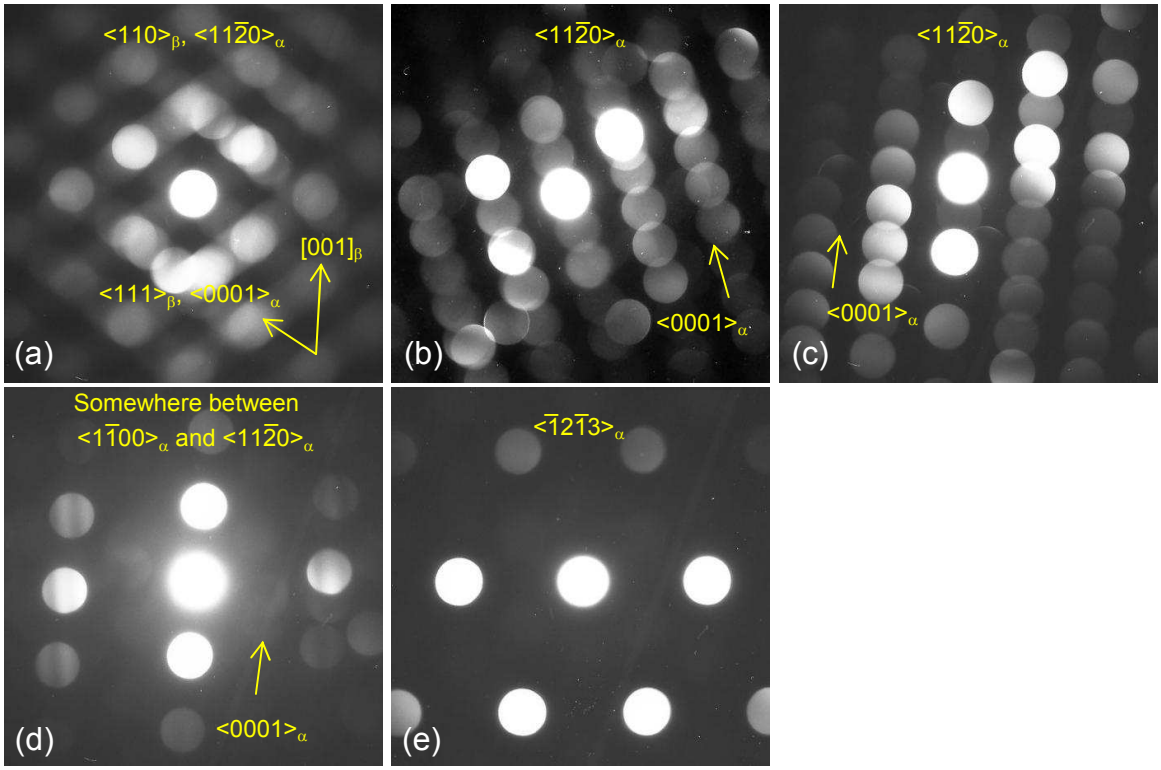

Figure 6.6 CBED patterns obtained with the electron beam focused only on single columnar grains, suggesting a random distribution of grains of hexagonal GaMnN.

6.2.2 GaMnN growth under Ga-rich conditions, as a function of growth temperature

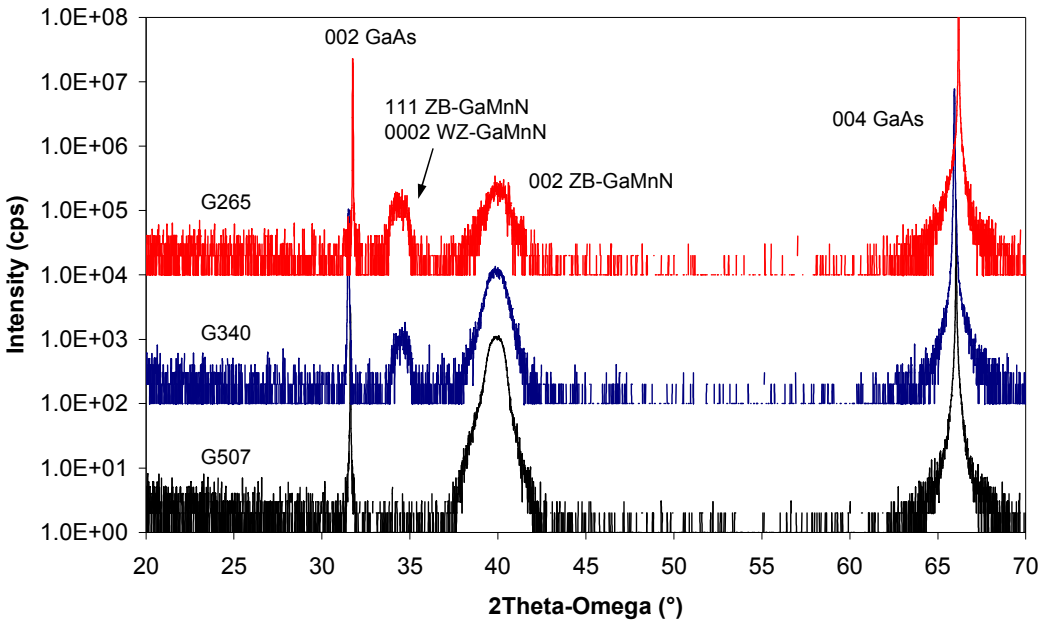

Figure 6.7 2θ-Ω X-ray diffraction profiles of samples G507, G340 and G265 grown under Ga-rich conditions at 507°C, 340°C and 265°C, respectively. The extra peaks emerging at 340 and 265°C are considered to be due to the presence of randomly oriented grains of cubic and hexagonal GaMnN. Note: These XRD spectra are simply offset in this figure by multiplying the spectrum of sample G340 by 100 and G265 by 10000, respectively, in order to highlight the structural evolution with decreasing growth temperature under such Ga-rich consitions.

Representative XRD spectra for this sample set obtained using the 2θ-Ω scanning mode are shown in Figure 6.7. An additional peak located at about 34~35° emerges when the growth temperature is reduced to 340°C and 265°C, again being attributed to the formation of polycrystalline cubic or/and hexagonal GaMnN within the predominantly zinc-blende GaMnN lattice.

Representative SE images for this sample set grown under Ga-rich conditions are shown in Figure 6.8. Ga droplets formed on the as-grown surfaces of samples G680 and G507 were removed by immersion in boiling HCl for the purpose of RHEED

investigation (e.g. Figures 6.8a,b). At 340°C, the Ga droplets are no longer evident (Figure 6.8c) whilst remnant faint streaks suggest a slightly reduced mobility of Ga adatoms on the surface under such Ga-rich conditions. A slightly rough surface, again with traces of these streaks, is shown in Figure 6.8d after HCl etching. At the lower growth temperatures of 265°C (and 186°C, figure not shown), no liquid Ga was observed during growth and no Ga droplets were formed after growth. As a consequence, a great improvement in the surface morphology was observed (e.g. Figure 6.8e).

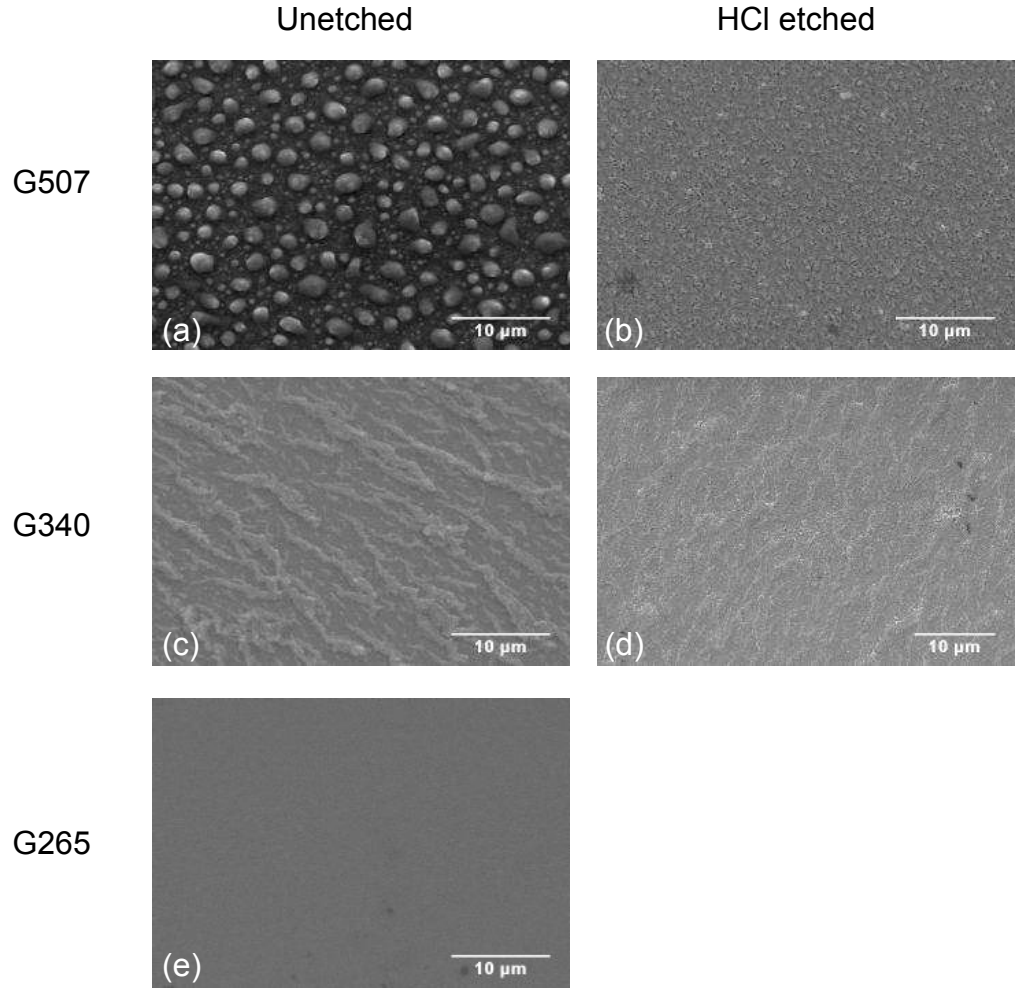

Figure 6.8 SE images of GaMnN samples grown at under slightly Ga-rich conditions. (a,b) as-grown and etched surfaces of sample G507; (c,d) as-grown and etched surface of sample G340; (e) as-grown surface of sample G265.

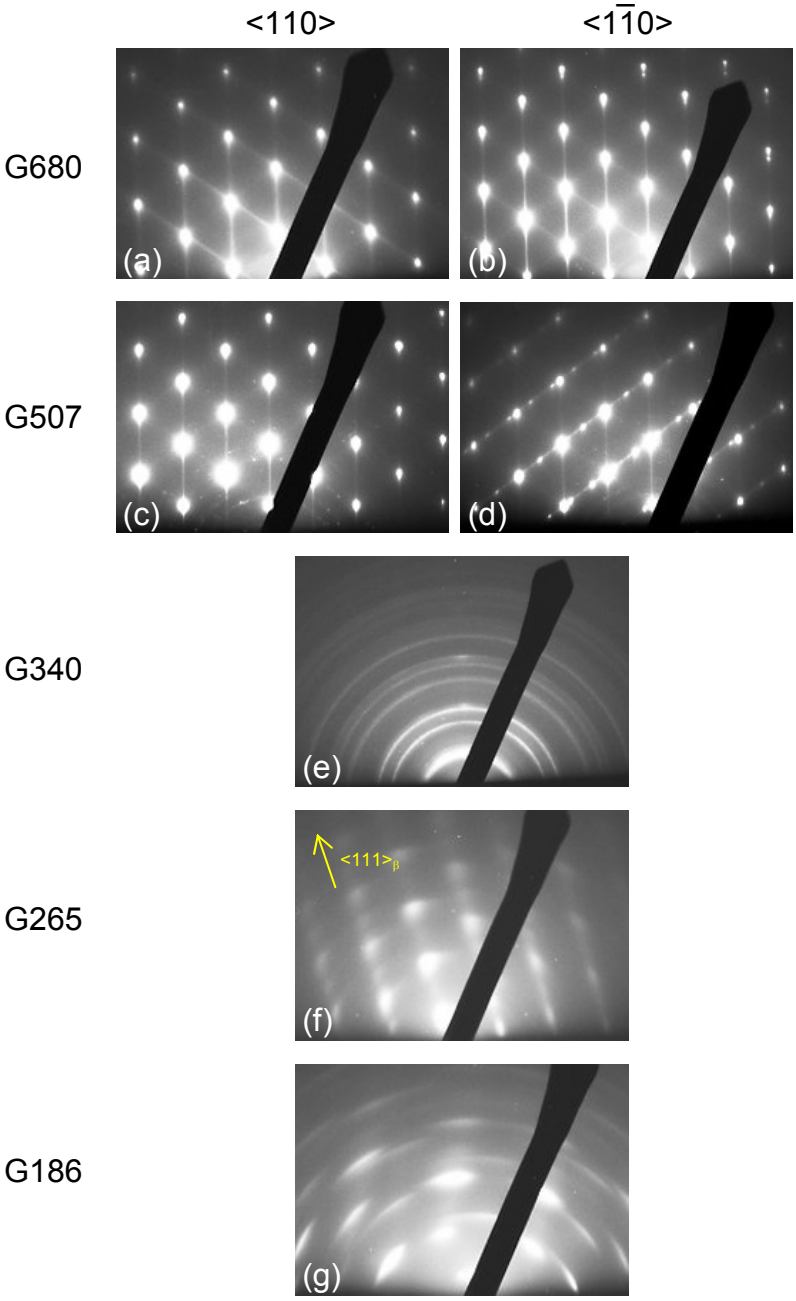

Figure 6.9 RHEED patterns of GaMnN grown under slightly Ga-rich conditions. (a,b) Sample G680 and (c,d) sample G507 recorded along orthogonal <110> projections. (e,f,g) samples G340, G265 and G186, respectively.

RHEED patterns of this sample set are presented in Figure 6.9. A curious transition from cubic growth (samples G680 and G507) to polycrystalline cubic growth (sample G340) then to more crystalline growth with a tilted axis (samples G265 and G186) in

terms of the original growth direction was achieved with decreasing growth temperature.

Samples G680 and G507 demonstrated cubic growth, whilst streaks perpendicular to the shadow edge in Figures 6.9a,b suggest that there are small smooth areas on the sample surface but the overall epilayer is still rough. Extra spots in Figure 6.9d due to hexagonal phase are indicative of a strong anisotropy along the orthogonal <110> projections for sample G507.

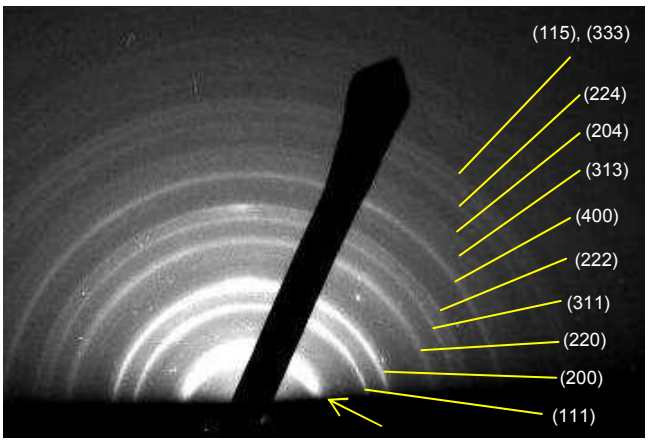

Figure 6.10 Enlarged image of Figure 6.9e with precise indexing of diffraction rings confirming the formation of polycrystalline zinc-blende GaMnN at 340°C.

As 340°C, clear, sharp diffraction spots disappeared, being replaced by continuous diffraction rings as a result of the formation of polycrystalline material. Since all RHEED patterns in this work were recorded using the Jeol 2000fx operated at 200 kV, the camera constant was calculated with reference to a known material and used to index these diffraction rings. However, in practice, the camera constant may vary slightly, depending on the height of the area sampled by the incident electron beam above the plate camera, and also on the accuracy of the spacing measurement on the negatives for both the reference material and the unknown sample. These factors

make the RHEED indexing process not so simple and straightforward. However, in this particular case for sample G340, nearly all the diffraction rings in Figure 6.9e were successfully confirmed to be associated with zinc-blende GaMnN. An enlarged image of the RHEED pattern of Figure 6.9e is presented in Figure 6.10 with each diffraction ring labelled accordingly. In addition, a strong diffraction ring near the shadow edge (arrowed in Figure 6.10) with corresponding lattice spacing of ~3.39~4.42 Å is apparent. With reference to the XRD data of various Mn-N, Mn-Ga and Ga-Mn-N compounds, this diffraction ring is considered to be due to the presence of polycrystalline $Ga_{5.2}Mn$, which is unfortunately not confirmed by SAED.

As the growth temperature was reduced further down to 263°C and 186°C, the RHEED patterns implicated a tilted growth, with closed packed planes roughly parallel to the shadow edge. Detailed characterisation of these samples by TEM is presented.

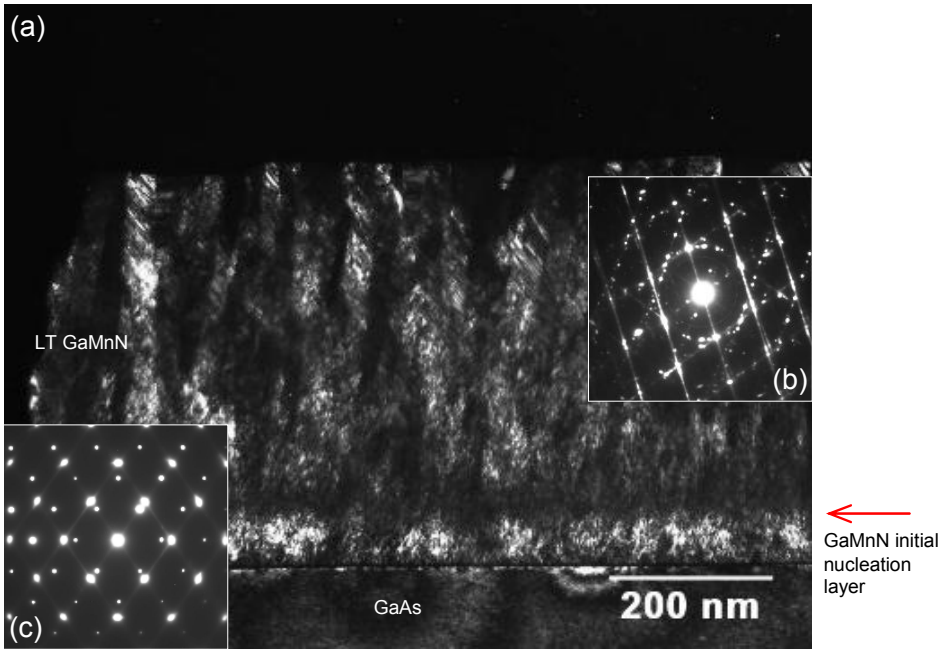

Figure 6.11 (a) 004 dark field TEM image of sample G340 (b,c) inset SAED patterns recorded within the low-temperature grown GaMnN and at the high temperature GaMnN buffer layer, respectively.

An 004 dark-field image of G340 with diffraction patterns inset is shown in Figure 6.11. The epilayer is estimated to be 500 nm thick, indicating a relatively high growth rate under such slightly Ga-rich conditions even at this low growth temperature. An initial high-temperature nucleation layer of about 60 nm is highlighted and confirmed to be single crystal cubic phase by the electron diffraction pattern inset (Figure 6.11c). The epilayer becomes highly faulted, containing a very high density of thin planar defects. An SAED pattern recorded over this part of the layer is shown in Figure 6.11b, revealing this layer to comprise predominantly epitaxial and randomly oriented cubic and hexagonal GaMnN. This seems to be inconsistent with the RHEED pattern shown in Figures 6.9e and 6.10 in which no rings or diffraction spots attributed to hexagonal GaMnN were identified. The explanation of this discrepancy can be made in terms of the size of regions sampled by the electron beam in RHEED and SAED. The probe of the incident electron beam during RHEED samples material on the scale

of ~1 mm^2, whilst in TEM mode the size of the area selected to form a diffraction pattern is on the scale of hundreds of nanometres. Accordingly, RHEED patterns provide an overview of the sample near surface microstructure, whilst fine scale lattice structures may be appraised by SAED.

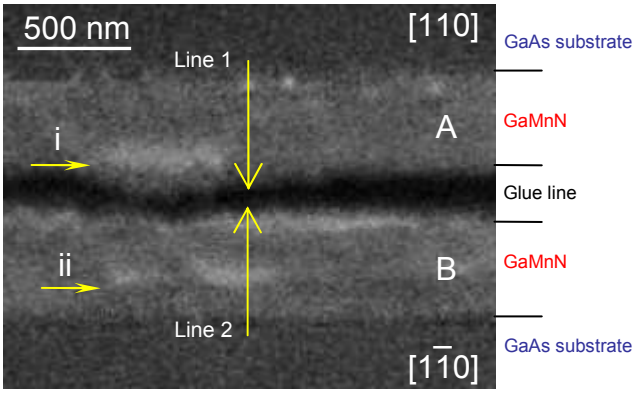

Figure 6.12 (a) SE image (b) EDX line profile 1 (c) EDX line profile 2 (shown in Figure 6.13a and b respectively) of sample G340 acquired using scanning mode of Jeol 2000fx

Figure 6.12 shows a cross-sectional SE image of sample G340 obtained using the scanning mode of the Jeol 2000fx. EDX line scans were subsequently performed from the interface towards the sample surface on both sides for the purpose of investigation of the Mn incorporation with representative results plotted in Figure 6.13a and b, respectively. As for the SE image, two bands, one near the surface on side A arrowed by 'i', the other located in the middle of the layer on side B arrowed by 'ii', are highlighted, suggesting features different from their surrounding areas. The Mn concentration on side A seems comparatively low throughout the layer, at a level of ~1.5~2 at%. Given the large associated errors, this data set is indicative of Mn incorporation on the level of detestability. In comparison, a significant increase in the Mn content from the line trace on side B was apparent, as shown in Figure 6.13b. A number of scans carried out at different locations on this side confirmed this

observation indeed to be a general case for this sample. The coincidence in location of the band structure highlighted in Figure 6.12b and this high Mn concentration signal in EDX suggests that a Mn-rich layer has developed mid way during the growth, accommodating excessive Mn under such Ga-rich growth conditions. It is worth mentioning that the variation of Ga counts does not indicate different levels of Ga content, but is considered to be due to a variation of sample layer thickness.

(a)

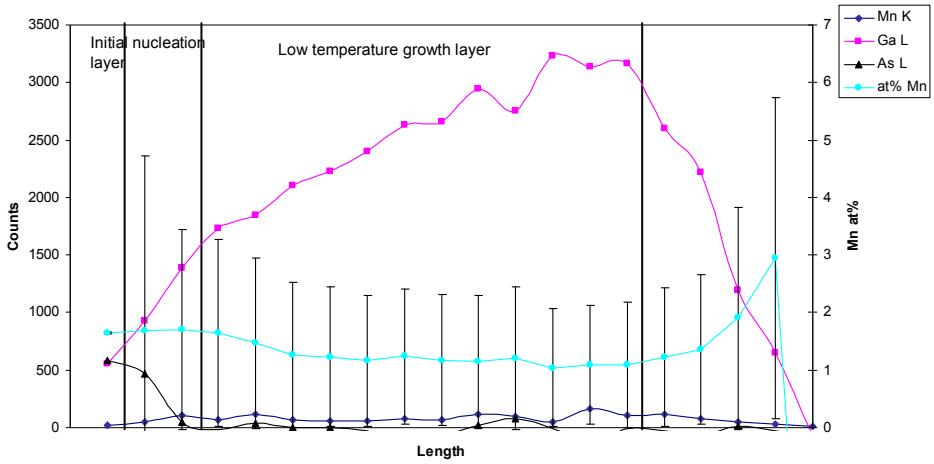

(b)

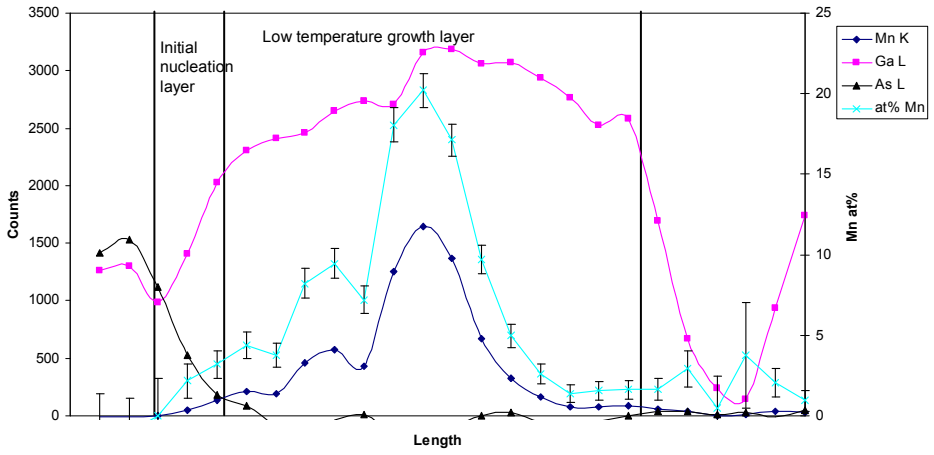

Figure 6.13 EDX line profiles for sample G340 obtained with the scanned electron beam following (a) line 1 and (b) line 2 in Figure 6.12.

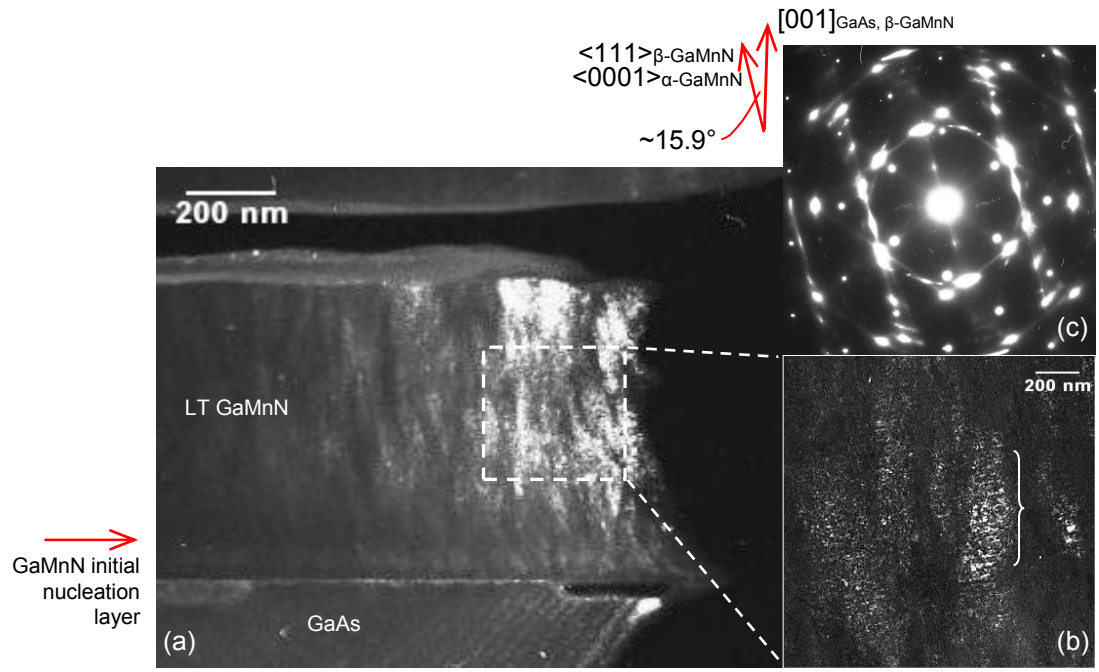

Figure 6.14 (a) 004 two-beam dark field TEM image of sample G265. (b) Dark field image using diffraction spots only attributed to hexagonal GaMnN illustrating steaks nearly parallel to the substrate epilayer interface. (c) SAED pattern recorded over the whole layer confirming the tilted growth.

An 004 two-beam dark field TEM image of sample G265 is shown in Figure 6.14. The thickness of the GaMnN layer is estimated to be ~500 nm, similar to that of sample G340. The tilted growth in terms of the original growth axis suggested by RHEED (Figure 6.9f) was confirmed by SAED (Figure 6.14c) recorded over this sample, including the GaAs substrate, as presented in Figure 6.14c. This SAED pattern looks complicated due to an overlap of several sets of diffraction spots attributed to the GaAs substrate, the initial epitaxial GaMnN nucleation layer, and the low temperature grown cubic and hexagonal GaMnN with associated thin planer defects. This pattern is simply selected to illustrate the tilted growth with key directions labelled alongside, with a measured angle of 15.9° between the closed packed planes, i.e. <111> for cubic GaMnN and <0001> for hexagonal GaMnN, and the [001] direction for the GaAs substrate. Further, an SAED pattern recorded only over the low temperature grown layer and an associated schematic illustration are also

presented in Figures 6.15a and b, respectively. Surprisingly, there is no evidence for the presence of polycrystalline cubic and hexagonal GaMnN, which is normally considered to be a typical feature for GaN grown at such a low temperature. Instead, the coexistence of cubic and hexagonal GaMnN together with cubic GaMnN microtwins suggests that in response to such conditions, the sample has adopted a modified growth mode, with the development of a structure of randomly intermixed close packed planes. The faulted growth is also evidenced by streaks highlighted in Figure 6.14b, obtained only using diffraction spots attributed to wurtzite material.

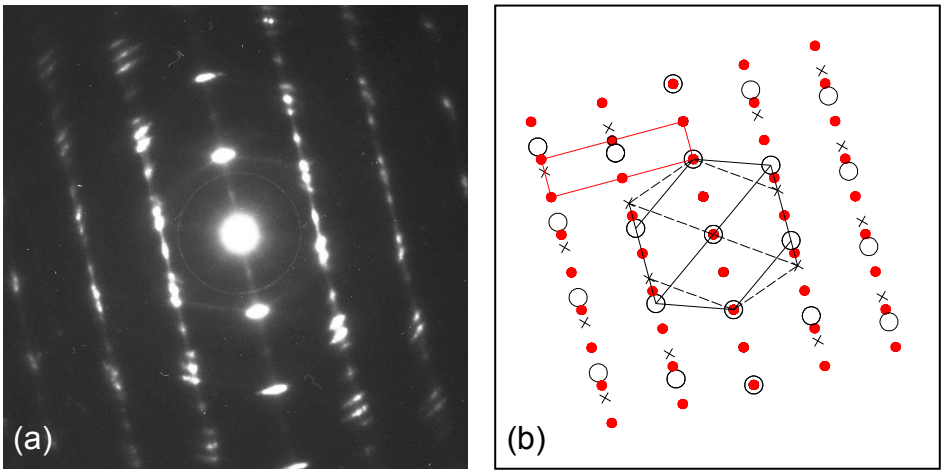

Figure 6.15 (a) SAED pattern recorded from the low-temperature grown GaMnN (G265). (b) Schematic diagram showing the association of diffraction spots from the hexagonal phase (solid dots), the cubic phase (open circles) and cubic microtwins (crosses).

The EDX spectrum (Figure 6.16) scanned across the epilayer indicates that Mn is incorporated into the epilayer at a concentration of ~2.5-4.5 at%, which is generally higher than that for sample G340, suggesting an improved growth condition for Mn incorporation. In addition, the trend of increasing Mn concentration with increasing layer thickness was also evident of a surfactant effect, with accumulated Mn on the growth front, as reported previously in Chapter Five.

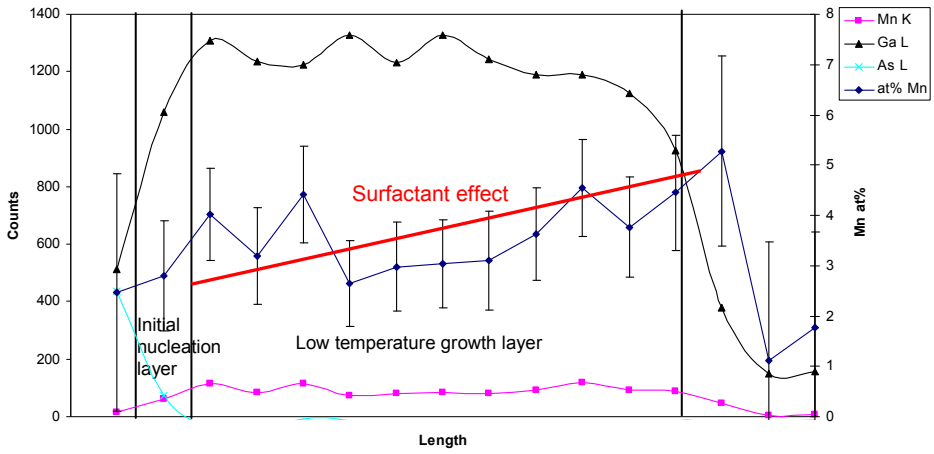

Figure 6.16 EDX spectrum of sample G265 showing the elemental variation across the epilayer. The Mn atomic concentration is calculated by assuming Mn and Ga atoms are 100 at%.

Table 6.2 Electrical properties of samples grown at low temperatures under Ga-rich or N-rich conditions

No.	Growth Temp (°C)	Growth condition	R_{Hall} (Ω/T)	p_{Hall} (cm^{-3}) (sheet density divided by thickness in cm to get volume density)	μ_{Hall} ($cm^2V^{-1}s^{-1}$)	Mn at%
M0	680	N-rich	-	-	-	0
N680	680	N-rich	60.2	5.37×10^{17}	269	~1.8 (estimated by MBE)
N597	597	N-rich	103.7	3.01×10^{17}	213	-
N443	443	N-rich	143.5	2.17×10^{17}	241	~5.0
N265	265	N-rich	14.6	2.1×10^{18}	252	-
N186	186	N-rich	26.2	1.2×10^{18}	238	-
G680	680	Ga-rich	19.7	6.4×10^{17}	307	-
G507	507	Ga-rich	23.9	5.2×10^{17}	320	-
G340	340	Ga-rich	48.3	1.8×10^{17}	274	~1.5-2.0
G265	265	Ga-rich	39.5	3.2×10^{17}	233	~2.5-4.5
G186	186	Ga-rich	35.1	3.6×10^{17}	299	-

The results of electrical measurements for this sample set grown under Ga-rich and N-rich conditions are listed in Table 6.2[9]. The Hall effect measurements show

[9] The electrical property measurements were carried out by Kevin Edmonds in the School of Physical and Astronomy.

unambiguously that whatever growth conditions used, these Mn-doped films are p-type. For samples grown under a slightly N-rich conditions, a slightly increase in hole density is achieved as the growth temperature is reduced, with a nearly constant corresponding mobility of more than 200 $cm^2V^{-1}s^{-1}$. Also there is a significant drop in Hall coefficient. For samples grown under nominally Ga-rich conditions, even though a steady increase in Hall coefficient is detected, the hole density and mobility values appear to be almost independent of the growth temperature and increasing Mn incorporation as evidenced by EDX.

6.3 Discussion

It is noted that a more comprehensive discussion of these results in the wider context of GaMnN growth is presented in Chapter Seven. Attention is mainly being given to the influence of growth conditions of reduced temperature under Ga-rich conditions. Since no fast-moving liquid Ga during growth and Ga droplets after growth were observed under such growth conditions, it is considered that the disappearance of Ga is associated with either a large amount of N vacancies within these GaMnN layers or a possible shift from slightly Ga-rich conditions to N-rich conditions. In addition, the tilted growth is due to a random build up of close-packed planes for both cubic and hexagonal GaMnN on one of the {111} planes of cubic microtwins within the epitaxial cubic GaN/GaAs(001).

6.4 Summary

GaMnN samples grown on GaAs(001) substrates under conditions of reduced growth temperature have been investigated. Under N-rich conditions, reducing the temperature is simply associated with the transformation from single crystal cubic

growth to polycrystalline cubic and hexagonal mixed phase growth. In comparison, under Ga-rich conditions, low temperature growth leads to a recovery from polycrystalline growth to a tilted mixed phase growth with close packed planes for both cubic and hexagonal GaMnN oriented roughly parallel to the growth surface. This mode of growth is also accompanied by an improved Mn incorporation which is not commonly found for samples grown under such Ga/N ratios at elevated temperature.

CHAPTER SEVEN

Discussion

7.1 Introduction

In this chapter, the key observations regarding the epitaxial growth of GaMnN/GaAs(001) by PAMBE as a functional III/V ratio, Mn-flux and growth temperature are initially summarised. The effect of the incorporation of Mn on the development of GaMnN microstructure is thus interpreted based on the directionality of chemical bonding of a Ga-terminated surface and the interaction between the adatoms and the underlying lattice. A fuller discussion about the interrelationship between the processing, structure and functional properties of GaMnN/GaAs(001) is also presented.

7.2 Effect of the incorporation of Mn on the development of the GaMnN/GaAs(001) microstructure and functional properties

7.2.1 GaMnN/GaAs(001) Process map, based on this work

Prior to the deposition of GaMnN layers under different growth conditions, an initial nucleation layer of GaMnN (i.e. a GaMnN buffer layer) was grown on the GaAs(001) buffer layer in the presence of a trace level of As at 680°C under a slightly N-rich

condition[10]. The GaMnN layers of interest were then grown and characterised as a function of Ga/N ratio, Mn flux and growth temperature, respectively. Since an overall chamber pressure was maintained by a flow of N_2 and the power of the RF plasma source used to generate the activated nitrogen was fixed at 450 W, the Ga/N ratio was varied merely by changing the Ga flux. The growth of GaMnN samples with increasing Mn concentration was carried out under slightly N-rich conditions. It is noted that both of these two sample sets were deposited at 680°C. In Figure 7.1, the three axes corresponding to these three growth parameters along with each sample positioned in 3D according to its growth condition were presented.

[10] For convenience, the terms GaMnN or GaMnN layer in the following discussion simply refer to the GaMnN layer grown on the initial nucleation layer or buffer layer of GaMnN deposited under specific growth conditions.

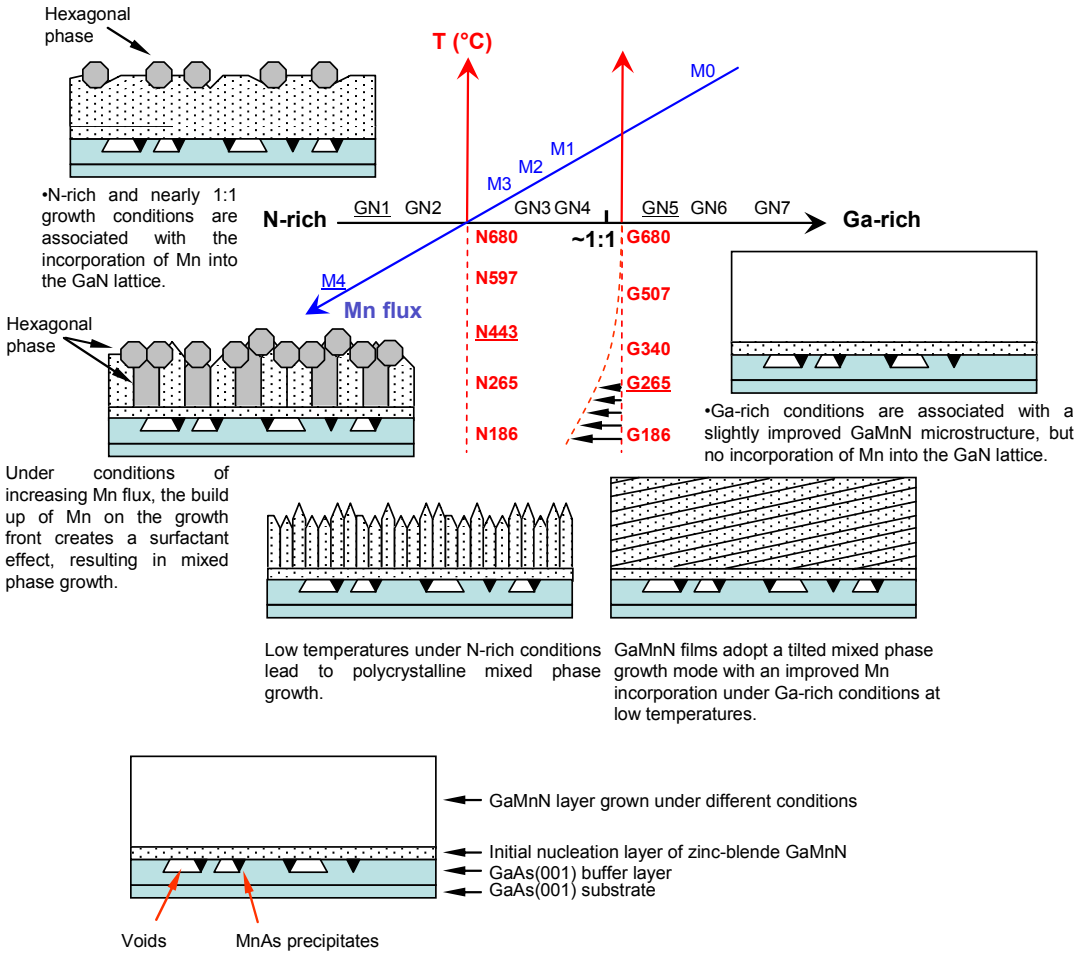

Figure 7.1 Summary of the growth of GaMnN layers on GaAs(001) as a function of Ga/N ratio, Mn flux and growth temperature, respectively. The three axes represent the three main growth parameters, i.e. the Ga/N ratio, the Mn flux and the growth temperature, respectively. Each sample is positioned according to its growth condition. An overall chamber pressure of $2\text{-}3\times10^{-5}$ mbar was maintained by a flow of N_2 with the activated N generated by the RF plasma source operated at 450 W. The beam equivalent pressures for Ga and Mn were set at levels of $\sim10^{-7}$ mbar and $\sim10^{-9}$ mbar, respectively. MnAs precipitates extending into the GaAs buffer layer were identified, using SAED and EDX, for all samples.

The key observations during this work are also summarised in Figure 7.1. Briefly, the initial GaMnN nucleation layer maintains a precise orientation relationship with respect to the GaAs substrate. However, MnAs precipitates and associated voids were found at the interface of GaMnN and GaAs extending towards the GaAs substrate. At 680°C, N-rich and nearly 1:1 growth conditions are associated with the incorporation of Mn into the GaN lattice, whilst Ga-rich conditions are associated with a slightly improved GaMnN microstructure and a maximum growth rate, but without the

incorporation of Mn. Under conditions of increasing Mn flux (under slightly N-rich conditions), the build up of Mn on the growth front creates a surfactant effect, resulting in a mixed phase columnar growth mode. Under N-rich conditions, reducing the temperature is simply associated with the transformation from single crystal cubic growth to polycrystalline cubic and hexagonal mixed phase growth. Under Ga-rich conditions, low temperature growth leads to a tilted mixed phase growth mode with closed packed planes of both hexagonal and cubic phases tilted at 15.9° with respect to the $(001)_{GaAs}$ plane, whilst improved Mn incorporation under Ga-rich conditions was also detected using EDX.

7.2.2 Initiation of GaMnN cubic epitaxy on GaAs(001)

The use of As to promote the formation of single phase zinc-blende GaN on GaAs(001) substrates has long been recognized [50]. It was considered that due to the big difference in bond strength between Ga-As (2.17 eV [142]) and Ga-N (4.97 eV [143]), arsenic acts as a catalyst on the growth surface, i.e. allowing the mobile and highly active nitrogen to replace the As and bond to the Ga atoms. Also, the presence of As during the growth of zinc-blende GaN leads to a change of the surface reconstruction from the equilibrium (4×1) to (2×2) or c(2×2) and to a lowered surface energy according to first-principle total-energy calculations [56]. In parallel, it is worth mentioning that N-rich conditions also play an important role during the early stages of the cubic growth of GaN [47-49], i.e. providing sufficient N to form stronger Ga-N bonds, being essential for the cubic epitaxy of GaN on the GaAs(001) to be quickly initiated.

In this work, a trace level of As was universally employed under slightly N-rich conditions at the beginning of the growth. The presence of a low-concentration of Mn-flux was found to have no obvious influence on the development of the GaMnN microstructure. SAED has confirmed in several cases that the GaMnN buffer layer maintains the same orientation with respect to the GaAs substrate (e.g. Figure 5.5d). Details of the interface and the nature of the planar defects of the GaMnN initial nucleation layer near the interface become evident from HREM observations. For example, Figure 5.6 shows that the interface is flat with no sign of oxidation or amouphourisation. The lattice mismatch between the two layers is accommodated by the development of a closely spaced array of misfit dislocations, in good agreement with reports by Trampet et al [61] and Chandrasekhar et al [65]. However, it is noted that the high density of thin planar defects (i.e. stacking faults and microtwins) must also contribute to the relaxation of the misfit strain during the initiation of epitaxy. More importantly, in between two nearby dislocations, the continuity of the {111} lattice planes across the interface is clearly visible, which becomes the basis for the assessment of GaMnN absolute polarity using CBED, ascertained from the polarity of the GaAs substrate.

Formation of MnAs inclusions

MnAs inclusions at the GaMnN and GaAs interface extending to the GaAs buffer layer have been identified successfully, combining the use of SAED to provide the structural information and EDX analysis to provide the chemical composition. It was also observed that size of MnAs inclusions was dependent on the growth conditions, decreasing with increasing Ga-flux and becoming smaller at reduced temperatures. It is noted that zinc-blende GaMnAs grown on (001) oriented GaAs by MBE, following

annealing, has also been found to contain MnAs precipitates distributed throughout the epilayer, as assessed using TEM [31]. The presence of MnAs precipitates within as-grown low temperature MBE material, as assessed using in-situ RHEED in MBE and XRD, has also been reported [144]. Similarly, it has been suggested that MnAs precipitates are formed within zinc-blende InMnAs epilayers grown on (001) oriented InAs or GaAs substrates, as evidenced by magnetic measurements [12] and XRD [145], respectively, whilst being suppressed at low growth temperatures of ~200°C [12,146]. It is also noted that α-MnAs adopts the NiAs-type structure, involving both anions and cations on the same close packed lattice planes and the α-MnAs phase is stable under ambient conditions accordingly to the binary phase diagram [147]. In this work, as confirmed by SAED and CBED, MnAs inclusions within samples grown under N-rich conditions were embedded within the GaAs buffer layer with an orientation relationship of $[11\bar{2}0]_{MnAs}$ // $[110]_{GaAs}$ and $[0001]_{MnAs}$ // $[1\bar{1}1]_{GaAs}$, being consistent with that of MnAs formed within GaAs following Mn ion implantation and annealing [31], whilst differing from those of MnAs formed via the direct epitaxial growth of MnAs on GaAs(001), i.e. $[\bar{1}\bar{1}20]_{MnAs}$ // $[110]_{GaAs}$ and $[0001]_{MnAs}$ // $[1\bar{1}0]_{GaAs}$ (termed type A), and $[\bar{1}\bar{1}20]_{MnAs}$ // $[1\bar{1}0]_{GaAs}$ and $[1\bar{1}02]_{MnAs}$ // $[110]_{GaAs}$ (termed type B)) [36].

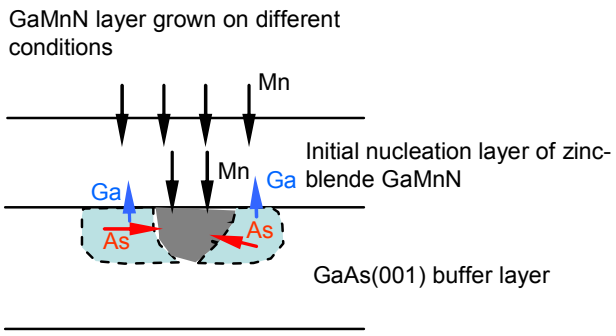

Figure 7.2 Formation of MnAs inclusions at the GaMnN and GaAs interface due to the migration of Mn from the GaMnN layer.

In view of the limited solid solubility of Mn within GaN, it is considered that Mn diffuses through this initial GaMnN layer and reacts with the GaAs buffer, with the consequent development of MnAs precipitates as observed. As illustrated in Figure 7.2, the process of MnAs precipitation may involve three steps, i.e. the incorporation of Mn into the GaMnN layer, the migration of Mn from the GaMnN layer to the interface and the reaction between Mn and As to form MnAs with the consequent displacement of Ga. During the deposition of the various GaMnN layers, including the GaMnN grown under different conditions and the GaMnN initial nucleation layer, strong exchange of Mn for Ga in GaAs may occur in some regions, leading to the introduction of well defined MnAs precipitates and leaving the surrounding region depleted with As in some degree and highly strained, hence being associated with the initiation of void formation. Due to the varying size of MnAs inclusions as a function of the growth, it is evident that their presence is not only dependent on the interactions that occur during the deposition of the GaMnN buffer layer, but also dependent on growth conditions, which determine both the mobility and concentration of Mn within the growing layer. Since Mn may only be incorporated into GaN under N-rich or nearly 1:1 conditions, it is not surprising to observe that such growth conditions are associated with larger MnAs inclusions as compared with Ga-rich conditions, and it is

considered that the small inclusions observed within samples grown under Ga-rich conditions are formed only during the deposition of the GaMnN buffer layer. Similarly, further expansion of MnAs may be prohibited due to the reduced Mn mobility at low temperatures. In parallel, voids on one or both sides of the MnAs inclusions are considered to be a result of the preferential ion beam milling of the strained As depletion region in the buffer layer. It is noted that the presence of such features within plan-view TEM foil through the GaN GaAs interface suggests that some of the Ga and As are transported into the growth film [63], although there was no evidence from detectable level of As in the GaMnN in the present work.

Quite interestingly, with reference to the polarity information obtained from the GaAs substrates, it was confirmed by SAED and CBED that the orientation relationship between the MnAs inclusions and the GaAs substrates changes from $[11\bar{2}0]_{MnAs}//[110]_{GaAs}$ under N-rich conditions to $[11\bar{2}0]_{MnAs}//[1\bar{1}0]_{GaAs}$ under Ga-rich conditions, as summarised in Table 4.2. This observation, however, serves as additional evidence supporting the interpretation regarding the formation of MnAs inclusions due to the migration of Mn down to the interface. Since growth conditions, i.e. Ga-rich or N-rich, correspond to different levels of Mn concentration in the top GaMnN layer, it is presumed that the observed polarity dependence may be attributed to a joint effect of Mn concentration which provide Mn source and the bonding directionality of GaAs which determine the orientation of MnAs depending on the supply of Mn, with the orientation relationship of $[11\bar{2}0]_{MnAs}//[110]_{GaAs}$ adopted initially at low Mn concentrations, changed to $[11\bar{2}0]_{MnAs}//[1\bar{1}0]_{GaAs}$ at high Mn concentrations.

In previous related work, much thicker GaN(~150 nm)/AlN(~50-150 nm) buffer layers were introduced between the GaMnN and GaAs as a diffusion barrier, confirming that p-type conductivity was indeed due to the Mn incorporation in the GaN lattice [5]. In this case arsenic was again used as a surfactant to initiate the growth of the undoped zinc-blende GaN buffer layer, but subsequent layers including the undoped AlN buffer layer were grown without this arsenic surfactant. The Mn shutter was opened only after the growth of the undoped GaN and AlN buffer layers. It was evident from TEM observations that MnAs inclusions extending into the GaAs substrate were suppressed by this GaN/AlN buffer layer [148], supporting the conclusion that the MnAs precipitates observed without the buffer layers here indeed arose due to Mn diffusion. The plan-view image of sample GN1 (Figure 4.9) shows that the MnAs inclusions are distinct, and as such would appear not to be detrimental for the layer transport properties [139,140]. In view of reported high Curie temperatures for bulk α-MnAs of 313 K [30] and for nano-particles embedded in GaAs of 330 K [33], the possibility of the direct influence of MnAs precipitates on the magnetic properties of these films can probably be discounted, since they are lower than the ~400 K T_C values determined for some of these GaMnN films.

7.2.3 Growth of GaMnN/GaAs(001) as a function of Ga/N ratio

Even though the samples were deposited under conditions of fixed Mn flux, significantly differing incorporation levels of Mn were observed, depending on whether the layers were grown under N-rich or Ga-rich conditions. Slightly N-rich growth conditions were found to be preferable for the effective incorporation of Mn, although this was also associated with a reduced growth rate and a highly faulted anisotropic defect microstructure as compared with growth under Ga-rich conditions.

Identical results regarding the strong influence of Ga/N ratio on the Mn incorporation into hexagonal GaN were also achieved by Haider et al [69] and Kuroda et al [72]. There is no evidence for the varying levels of Mn through this sample (0~4.0 at%) set having a destabilising effect on the formation of the zinc-blende GaMnN phase. It is possible that reports of mixed phase heteroepitaxy in the literature represents more extreme conditions of III/V ratio during growth [49,51,52].

Hall effect measurements revealed unambiguously that these GaMnN samples grown under increasing Ga flux corresponding to a transformation from N-rich conditions to Ga-rich conditions are p type (Figure 4.13). The Ga droplets on the surfaces of samples grown under Ga-rich conditions were found to have no influence on the electrical measurements. The origin of the electrical properties of this sample set is generally considered to be the incorporation of Mn into GaN under different growth conditions, but with additional possibilities of doping by C and/or O within the GaN (as potential trace level contaminants from within the MBE growth chamber), with the diffusion of Mn into the GaAs buffer layer being eliminated [139]. For both N-rich and Ga-rich growth conditions, a bulk hole density of about 10^{18} cm^{-3} with a corresponding mobility of 300 $cm^2V^{-1}s^{-1}$ were achieved. Since the presence of Mn within samples grown under Ga-rich conditions is undetectable using EDX, there is no direct correlation of the Mn content with respect to the transport properties, e.g. hole concentration and mobility, across the range of III/V growth conditions. The lack of a linear relationship between Mn content and hole concentration within these GaMnN layers grown under varying Ga/N ratio raises a question about the true status of excess “un-activated Mn” within the layer. In all cases for this sample set, a ferromagnetic signal was retained to above 400 K, as picked up by superconducting

quantum interference device magnetometer (SQUID) with magnetic field applied in the sample plane [140]. A large increase in magnetization was observed from 15 K down to 2 K with a clear hysteresis, attributed to a magnetic coupling between the Mn ions. Although nitride based precipitates were not observed within the samples examined here using XRD and TEM, it has been suggested that the high temperature magnetic performance of such GaMnN heterostructures arises from nano-sized Mn_xN_y clusters [140]. For the moment, this interpretation remains an open question. In a similar fashion, two distinct ferromagnetic signals were often detected and considered to originate from the co-existence of two phases, i.e. the ferromagnetic GaMnN alloy with low temperature ferromagnetism and Mn-rich nano-clusters responsible for high temperature ferromagnetism that persists to over room temperature [75,84].

Growth mechanism under varying Ga/N ratio at 680°C– a simple model

In order to improve the growth of GaMnN in a systematic way, it is necessary to understand the underlying kinetic processes during the propagation of these films. Surface reconstructions of GaN(001) have been intensively studied by means of RHEED measurements, STM and first-principle total-energy calculations [49,54,99]. Briefly, no matter what the growth conditions employed, the surface layer during growth is more or less covered by excess Ga atoms, with thickness of the Ga layer being dependent on Ga/N ratio [99]. These Ga adatoms are moving fast with their mobility being affected by the presence of N adatoms (or other atoms on the growth surface). In view of the meta-stable nature of zinc-blende GaN, both Ga and N atoms on the growth surface have the tendency to occupy hexagonal sites with any wrong placement for these two types of atoms leading to the nucleation and subsequent

propagation of a high density of stacking faults on {111} planes or even mixed phase growth. Certainly, the addition of Mn may change the growth mode and to date this has not been quite understood. The effect of the presence of Mn during the growth of hexagonal GaMnN was investigated by Kuroda et al [72]. A drop in desorption time due to the induced disturbance by the presence of Mn, especially under conditions of lower Ga surface coverage was observed. In this work, EDX measurements confirmed that Mn may only be incorporated into cubic GaN under N-rich or nearly 1:1 Ga/N growth conditions, in good agreement with reports regarding the growth of hexagonal GaMnN [69,72]. Further, a strong anisotropy along the orthogonal <110> projections confirmed by RHEED and SAED indicated that, under N-rich conditions, both a high density of stacking faults and the development of a hexagonal phase on the sample surface, due to a cool down effect at the end of growth, are mainly located on the absolute {111}A planes. With reference to the theories regarding to the growth of pure cubic GaN/GaAs(001), a proposed model is now given in an attempt to interpret the differing incorporation of Mn under Ga-rich or N-rich growth conditions and the development of such anisotropic growth features, respectively.

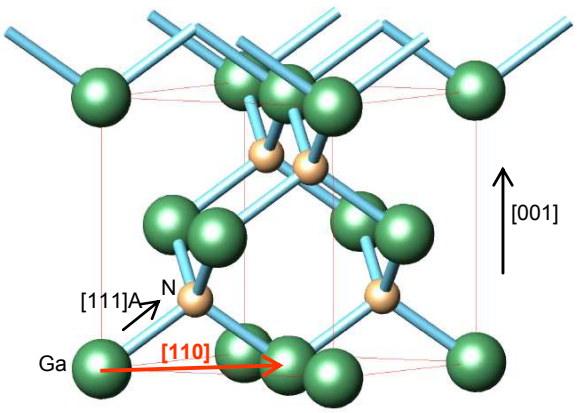

Figure 7.3 Schematic illustration of the Ga-terminated GaN (001) surface in which all the Ga dangling bonds lie in the (110) planes.

Due to the weak bond strength between Ga atoms as compared with that of Ga-N, the mobility of Ga atoms is significantly high during growth. This suggests that the first layer of the growing GaMnN must be terminated by Ga atoms, with two dangling bonds for each Ga being upward and with the other two already bonded to the underlying lattice N atoms. In view of the polar nature of cubic GaN, it is apparent to note in Figure 7.3 that all these available dangling bonds lie in the (110) planes. Due to the involvement of Mn on the growth surface, picturing the interaction between these three elements, i.e. Ga, N and Mn, becomes quite complicated. However, the situation may be simplified by initially considering the chemical bond energies between each possible pairs of elements on the growth front and the associated bonding directionalities. It is known that Ga forms weak Ga-Ga bonds (1.43 eV), while Mn forms weaker Mn-Mn bonds (0.63 eV) [42]. Once two N adatoms meet each other, a much stronger linkage (9.82 eV [42]) may take place, leading to the formation of a N_2 molecule which is easily desorbed from the growth surface. Even though there are no direct reports about the bond energies of Ga-N, Mn-N and Mn-Ga, they may be derived according to their chemical bond types and elemental properties, i.e. electronegativities. It was suggested by Al-Brithen et al that Sc-N may have the same bond strength as Ga-N, being 4.97 eV [143]. In addition, while the Ga-N bond has more ionic character than the Mn-N bond, the Mn-N bond in turn has more ionic character than the Mn-Ga bond, and the sequence of the bond energies of the various dimers on the growth surface may be written as: N-N (9.82 eV) > Ga-N (~4.97 eV) ≥ Mn-N > Mn-Ga ≥ Ga-Ga (1.43 eV) > Mn-Mn (0.63 eV). This suggests that it is quite possible for a Mn atom and a N atom to meet each other on the growth front and form a strong Mn-N bond, implicating that under certain levels of Mn, the incorporation of N atoms into the GaMnN lattice may also involve the incorporation

of associated Mn atoms. In view of the electronegativities of Ga, N and Mn, the exposed Ga dangling bonds and the N-side of the Mn-N dimers should be slightly negatively charged (labelled in Figure 7.4) and this energy barrier must be conquered in order to incorporate N atoms.

In addition, the size of the Mn ions (r=139 pm), being similar to that of Ga (r=126 pm) and much bigger than N (r=75 pm) also needs to be considered. During the dynamic process of the incorporation of N, the occupation of N on any wrong lattice sites may result in the nucleation of stacking faults on {111}A planes (or even the hexagonal phase), which once established are normally maintained throughout the epilayer. It is noted this kind of proposed initiation of stacking faults may exist uniformly on all {111} planes during the growth of pure cubic GaN, but may happen predominantly on {111}A planes during the growth of cubic GaMnN under N-rich conditions simply, because in the later case, a further rotation mechanism along these Ga-N bonds may be restricted due to the strong interaction between Mn and Ga.

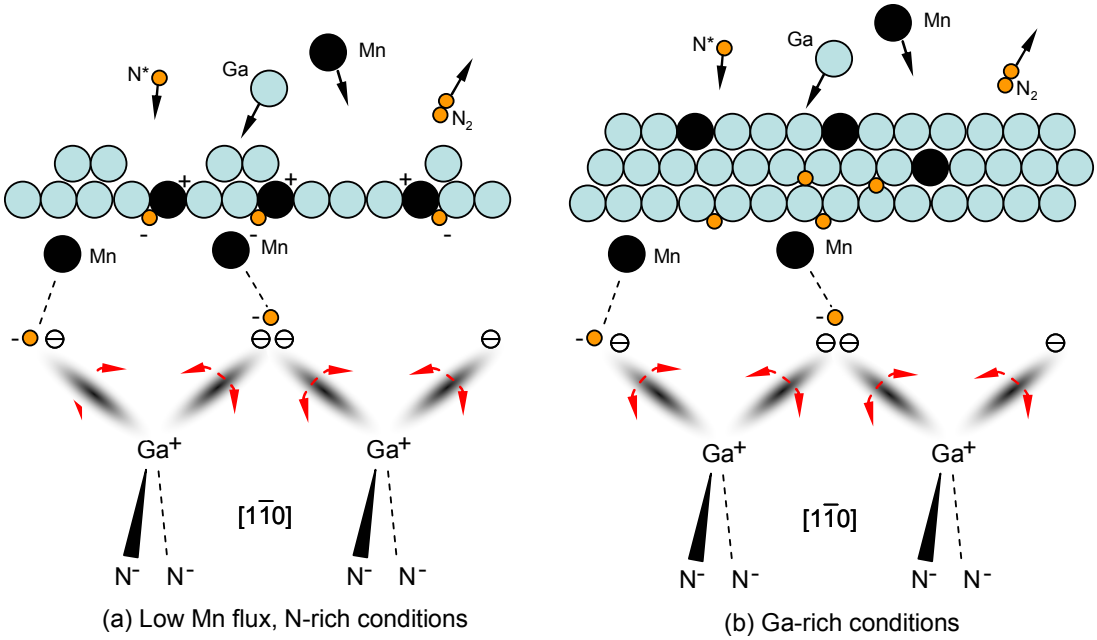

Figure 7.4 Schematic diagram showing the proposed growth mechanism for (a) N-rich and (b) Ga-rich growth conditions, respectively.

Under Ga-rich conditions, the growth surface is covered with the multiple layers of Ga adatoms, which still can maintain a high mobility with little interruption due to the presence of low density of N and Mn atoms, leading to an improved microstructure. However, under such growth conditions, the thick layer of Ga prevents Mn from migrating to the growth front (Figure 7.4b), resulting in a very low Mn incorporation rate as compared with growth under N-rich conditions. A supplementary evidence about the key role of fast moving Ga adatoms comes from the formation of hexagonal phase on the surface of samples grown under strongly N-rich conditions (e.g. Figure 4.11), being considered to be due to a reduced mobility of Ga adatoms with increasing level of N and a decrease in temperature during the initiation of cool down at the end of growth.

In summary, N-rich conditions are beneficial for the incorporation of Mn into GaN, with the presence of a high density of stacking faults predominantly on {111}A

planes attributed to the joint effect by the possible formation of Mn-N dimers on the growth front and the lattice bonding directionality of zinc-blende GaN. Ga-rich conditions are associated with the presence of a thick layer of Ga adatoms on the growth surface, acting as a barrier for Mn migration to the growth front, leading a very low Mn incorporation rate as compared with growth under N-rich conditions.

7.2.4 Growth of GaMnN/GaAs(001) under increasing Mn flux

Even though the Mn incorporation efficiency is comparatively low, being controlled by the Mn flux, an increasing level of Mn content with increasing Mn flux under N-rich conditions is evidenced by EDX. For sample M4 grown under the highest Mn flux, a discrepancy in the Mn concentration between the MBE estimation (15 at%) and the EDX measurement of the TEM sample foil (~5 at%) became apparent. Since the Mn-flux used during growth is far beyond the upper limit of Mn solid solubility, there must be an increasing amount of Mn atoms on the growth front which can not be incorporated effectively into the GaMnN lattice. Nevertheless, the accumulation of Mn atoms is considered to have a dominant impact during growth on the development of the GaMnN layer microstructure.

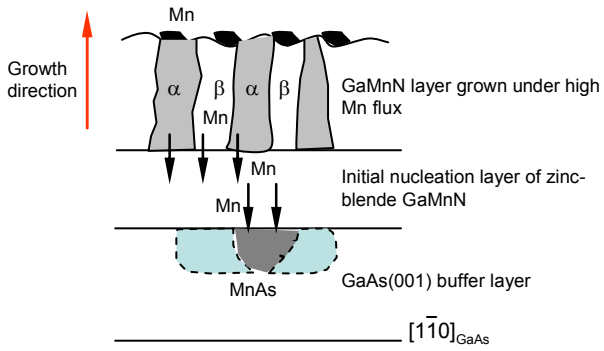

Figure 7.5 Schematic diagram showing columnar growth due to the accumulation of Mn on the growth surface

Direct evidence of the result of the Mn surfactant effect is the change in growth mode for the sample (M4) grown under conditions of the highest Mn flux, with a transition from cubic epitaxy at the initial nucleation layer stage to mixed phase growth of columnar grains at the GaMnN layer, as evidenced by SAED confirming the phase composition and by HREM showing grain boundaries of the two distinct α and β phases, as shown schematically in Figure 7.5. In addition, strong anisotropic growth was also confirmed by SAED, indicating that the hexagonal grains are also formed predominantly on the absolute {111}A planes. In this case, a high concentration of Mn on the growth front is considered to disrupt the surface migration of Ga in a manner analogous to growth under higher levels of N flux, as described in the previous section. In parallel with this, there is a complementary diffusion or segregation of Mn to the GaMnN growth front with the build up of a Mn surfactant layer that persists throughout the entire layer growth, becoming oxidised following exposure of the as-grown sample to atmosphere [149]. It is suggested therefore that purposely reducing the Mn flux to lessen the Mn accumulation on the growth surface after layer cubic initiation might be beneficial to maintain the cubic epitaxy of GaMnN at these higher levels of Mn flux.

Electrical measurements show that the hole concentrations of this sample set do not increase with increasing levels of Mn concentration, whilst a dramatic increase in mobility is apparent. Even though during the propagation of the film under high Mn flux, the excess Mn may diffuse down towards the GaMnN and GaAs interface to form MnAs inclusions and may also accumulate on the growing surface to promote the mixed phase columnar growth mode. In Chapter Five, even though the initial assessment using XRD and SAED showed no trace of additional phases within

sample M4, a Mn-rich region with distinct atomic arrangement as compared with the GaMnN matrix was highlighted using EFTEM and HREM (Figure 5.12). In fact, Mn-N compounds themselves may contain a considerable number of vacancies [150], acting as donors, compensating the increasing concentration of holes originating from the incorporation of Mn at Ga sites. It is also considered that the epilayer faulting, including high density of planar defects within cubic GaMnN and the formation of hexagonal GaMnN, the formation of Mn-rich precipitates and associated point defects, provides additional shifting channels for carriers, leading an increase in hole mobility with increasing Mn concentration.

Even though there are no magnetic data available for this sample set, the combination of the observed ferromagnetic signal retained up to 400 K in sample GN1 grown under a high N-rich condition and the identification of Mn-rich precipitates within sample M4 suggests that nano-size Mn-rich clusters may indeed play an important role within these GaMnN layers, from a magnetic point of view. Indeed, bulk Mn-N, Mn-Ga and Ga-Mn-N compounds are already known to have a variety of phases and interesting magnetic properties [109,150,151]. The theoretical work of Rao et al [114] suggested that the clustering of Mn and N may generate giant magnetic moments within GaMnN, which are responsible for the wide range of Curie temperatures reported. In particular, Huh et al [152] found that increasing levels of Mn concentration were associated with a degradation of sample surface morphology and electrical properties for single phase hexagonal GaMnN (confirmed by XRD) grown using plasma enhanced MBE, but with an improvement in magnetic properties, being quite similar to the results presented in this work. To date, a number of Mn-rich precipitates within either zinc-blende or wurtzite GaMnN with high Mn concentration

(sometimes following annealing process) have been identified by XRD or/and TEM. However, nano-size Mn-rich clusters with only short-range periodicity (or with structures of their corresponding bulk materials but highly distorted), may precipitate through atomic displacement during growth. This makes an absolute assessment of their lattice structures and elemental compositions rather difficult. It is noted that in parallel to this work, the local atomic structures around Mn for two cubic GaMnN samples with 2.5 and 10 at% Mn, respectively, have been investigated using the technique of Mn K-edge extended X-ray absorption fine structure (EXAFS), which provided direct evidence about the occupation of Mn on Ga sites for the low Mn concentration sample [153]. With regard to the high Mn concentration sample, associated simulations suggested that second phase Mn-rich clusters are more likely to be formed.

7.2.5 Growth of GaMnN/GaAs(001) at low temperatures

Regarding the low temperature growth of GaMnN under N-rich conditions, a transition from single crystal with well defined epitaxial relationship to mixed phase polycrystalline layers was apparent and always associated with increasing Mn incorporation into the GaN. In comparison, for low temperature grown GaMnN under Ga-rich conditions, a tilted growth mode was adopted with an angle of 15.9° between the close-packed planes of both zinc-blende and wurtzite GaMnN and the {001} planes of the GaAs substrate. Under such low temperature growth conditions, Mn is also successfully incorporated, which is not the case for samples grown under Ga-rich conditions at elevated temperatures [69,72]. As shown in Table 6.2, electrical measurements indicate that both sets of samples again exhibit p-type conductivity and

relatively high mobilities for these GaMnN layers, without obvious variation related to the decreasing growth temperature.

Typically, fast-moving liquid Ga during growth and Ga droplets after growth are characteristic for Ga-rich conditions. However, in this case, no Ga was observed at all at the lower growth temperatures, suggesting a change of the growth mode under such growth conditions. Currently, two possible interpretations can be suggested: First, the disappearance of Ga is associated with a large amount of N vacancies in these GaMnN layers. Normally low growth temperatures dramatically reduce the mobility of Ga atoms on the growth surface, providing opportunities for the excessive Ga atoms to be embedded quickly without the need of sufficient compensation from N atoms. Second, low growth temperatures result in a possible shift from slightly Ga-rich conditions to N-rich conditions. N adatoms at the surface can not overcome the desorption energy barrier for the formation of N_2 molecules, leading to an accumulation of N adatoms, and consequently a transition point from Ga-rich to N-rich growth is reached as the temperature is decreased to a certain level, thereby allowing the enhanced incorporation of Mn into the layer.

Indeed, it has been demonstrated that under Ga-rich conditions, a low growth temperature facilitates the incorporation of Mn into the GaN lattice. At 340°C, a Mn-rich layer is formed mid-way through the sample, although the overall Mn concentration is still very low. In particular, at 265°C, in connection with the tilted growth, instead of becoming polycrystalline, the layer again shows an improved incorporation of Mn as evidenced by EDX. It is therefore interesting to speculate that this is due to a reduced mobility of surface adadoms providing chance for Mn to

interact with the underlying N atoms, is associated with the transformation from Ga-rich to N-rich conditions as suggested.

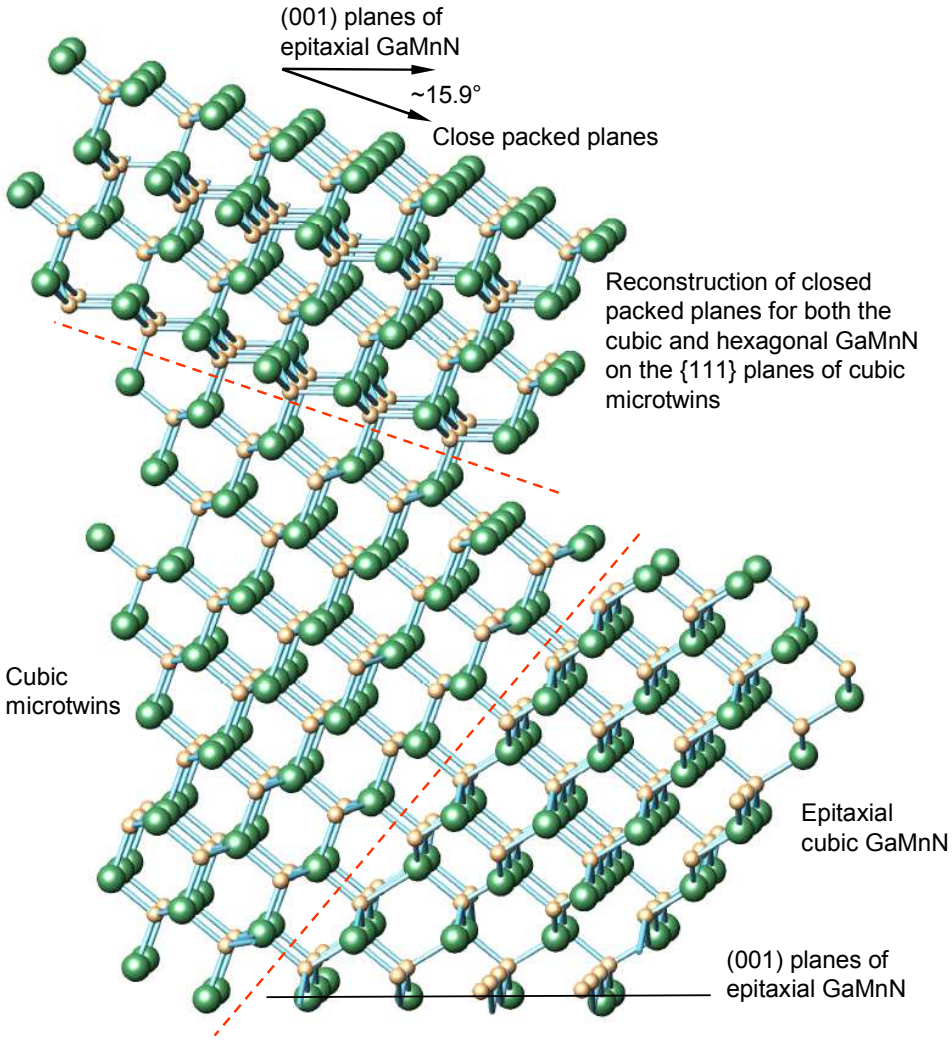

Figure 7.6 Schematic illustration of the tilted growth due to the formation of closed packed planes for both cubic (including cubic microtwins) and hexagonal GaMnN on cubic microtwins, after [68]

It is noted that the formation of hexagonal grains within cubic GaN with a tilted angle of 15.8~16° between $(0002)_\alpha$ and $(001)_\beta$ planes was previously reported by Balakrishnan et al [68], with two possible orientation relationships proposed based on RHEED observation and XRD pole figure analyses, i.e. $(0001)_\alpha$ formed on either $(115)_\beta$ or one of the {111} planes of microtwins within the epitaxial cubic

GaN/GaAs(001). Thermodynamically, it is more likely for the film to propagate on inclined close-packed planes without any continuity disruption even at low temperature, rather than using high index (115) planes. The random build up of atomic layers along close packed directions accompanied by an improved incorporation of Mn needs to be further investigated for the purpose of preparation of uniform GaMnN films with high concentration of Mn.

7.3 Summary

GaMnN thin films grown on GaAs(001) substrates by PAMBE have been investigated using a variety of analytical techniques. The stoichiometry of Ga, Mn and N species and the free migration of Ga on the growth front, controlled directly by the growth conditions, i.e. the Ga/N ratio, the Mn flux and the growth temperature, are considered to have a dominant effect on the incorporation of Mn and the development of the layer microstructure. By way of example, the mobility of Ga adatoms may be reduced by high N and Mn concentrations and lower growth temperatures, leading to the formation of hexagonal grains on the sample surface at the end of growth (strongly N-rich conditions, 680°C), mixed phase columnar growth (high Mn flux, 680°C) or tilted growth due to the formation of close packed planes on cubic microtwins (Ga-rich conditions, 265°C), respectively. In addition, a strong interaction between Mn and N atoms may exist, resulting in anisotropic nucleation and development of a high density of stacking faults under N-rich growth conditions (680°C).

CHAPTER EIGHT

Future work

It is believed that the widespread application of semiconductor spintronics may have a significant impact to the IC industry and the data storage industry, being subject to the availability of appropriate ferromagnetic semiconductors [1,7,10]. As a promising candidate for spintronic applications according to theoretical prediction [3], both cubic and hexagonal GaMnN have been investigated in an attempt to correlate the material transport and magnetic properties and the material microstructure. It seems that cubic GaMnN thin films are always p-type, whilst hexagonal GaMnN layers are only associated with n-type conductivity. Also, even though high temperature ferromagnetic signals have been detected for both cubic and hexagonal materials, they are mainly considered to be due to the formation of Mn-rich second phase precipitates rather than due to a uniform alloy. This complex situation frequently reminds us that we may be still at the beginning of the road of understanding and manipulating electron spins within GaMnN, or indeed within other candidate systems.

MBE have been widely used for investigations of the growth of GaMnN ferromagnetic semiconductors in order to demonstrate the viability of this material system. However, the basic growth mechanism for the incorporation of Mn is still not yet fully understood. It therefore becomes necessary to use in-situ RHEED, auger electron spectroscopy (AES) and modulated beam mass spectrometry (MBMS) to monitor the growth of both cubic and hexagonal GaMnN, for the purpose of

generating a growth model as guidance for improved control of the growth process. In this work, the incorporation of Mn together with a novel tilted growth mode under Ga-rich conditions at low temperatures was identified. It would be quite interesting to further investigate the growth under such reduced temperature conditions for the purpose of identifying conditions to retain only the cubic stacking sequence during the tilted growth mode.

In addition, in order to obtain a deeper understanding of the origin of ferromagnetism within GaMnN, it would be worth combining elemental and positional sensitive techniques, such as scanning transmission electron microscopy and scanning tunneling microscopy, with e.g. Lorentz microscopy.

References

[1] S.J. Pearton, C.R. Abernathy, D.P. Norton, A.F. Hebard, Y.D. Park, L.A. Boatner, J.D. Budai, Mat. Sci. Eng. R **40** (2003) 127.

[2] A.H. Macdonald, P. Schiffer, N. Samarth, Nature Mater. **4** (2005) 195.

[3] T. Dietl, H. Ohno, F. Matsukura, J. Cibert, D. Ferrand, Science **287** (2000) 1019.

[4] K.W. Edmonds, S.V. Novikov, M. Sawicki, R.P. Campion, C.R. Staddon, A.D. Giddings, L.X. Zhao, K.Y. Wang, T. Dietl, C.T. Foxon, B.L. Gallagher, Appl. Phys. Lett. **86** (2005) 152114.

[5] S.V. Novikov, K.W. Edmonds, A.D. Giddings, K.Y. Wang, C.R. Staddon, R.P. Campion, B.L. Gallagher, C.T. Foxon, Semicond. Sci. Technol. **19** (2004) L13.

[6] V.A. Chitta, J.A.H. Coaquira, J.R.L. Fernandez, C.A. Duarte, J.R. Leite, D. Schikora, D.J. As, K. Lischka, E. Abramof, Appl. Phys. Lett. **85** (2004) 3777.

[7] S.A. Wolf, D.D. Awschalom, R.A. Buhrman, J.M. Daughton, S. von Molnar, M.L. Roukes, A.Y. Chtchelkanova, D.M. Treger, Science **294** (2001) 1488.

[8] S.J. Pearton, Y.D. Park, C.R. Abernathy, M.E. Overberg, G.T. Thaler, J. Kim, F. Ren, J.M. Zavada, R.G. Wilson, Thin Solid Films **447-448** (2004) 493.

[9] T. Dietl, Nature Mater. **2** (2003) 646.

[10] H. Ohno, Science **281** (1998) 951.

[11] T. Dietl, Semicond. Sci. Technol. **17** (2002) 377.

[12] H. Munekata, H. Ohno, S.v. Molnar, A. Segmuller, L.L. Chang, L. Esaki, Phys. Rev. Lett. **63** (1989) 1849.

[13] H. Ohno, H. Munekata, S.v. Molnar, L.L. Chang, J. Appl. Phys. **69** (1991) 6103.

[14] F. Matsukura, H. Ohno, A. Shen, Y. Sugawara, Phys. Rev. B **57** (1998) R2037.

[15] T. Dietl, H. Ohno, MRS Bull. **28** (2003) 714.

[16] H. Ohno, A. Shen, F. Matsukura, A. Oiwa, A. Endo, S. Katsumoto, Y. Iye, Appl. Phys. Lett. **69** (1996) 363.

[17] M.E. Overberg, B.P. Gila, C.R. Abernathy, S.J. Pearton, N.A. Theodoropoulou, K.T. McCarthy, S.B. Arnason, A.F. Hebard, Appl. Phys. Lett. **79** (2001) 3128.

[18] X. Chen, M. Na, M. Cheon, S. Wang, H. Luo, B.D. McCombe, X. Liu, Y. Sasaki, T. Wojtowicz, J.K. Furdyna, S.J. Potashnik, P. Schiffer, Appl. Phys. Lett. **81** (2002) 511.

[19] J.M.D. Coey, C.L. Chien, MRS Bull. **28** (2003) 720.

[20] C. Palmstrøm, MRS Bull. **28** (2003) 725.

[21] S.A. Chambers, F.C. Farrow, MRS Bull. **28** (2003) 729.

[22] K.Y. Wang, R.P. Campion, K.W. Edmonds, M. Sawicki, T. Dietl, C.T. Foxon, B.L. Gallagher, *Magnetism in (Ga,Mn)As Thin Films With T_C Up To 173K*, PHYSICS OF SEMICONDUCTORS: 27th International Conference on the Physics of Semiconductors - ICPS-27, (2005), AIP **772** 333

[23] A.M. Nazmul, S. Sugahara, M. Tanaka, Phys. Rev. B **67** (2003) 241308.

[24] R.P. Campion, K.W. Edmonds, L.X. Zhao, K.Y. Wang, C.T. Foxon, B.L. Gallagher, C.R. Staddon, J. Cryst. Growth **247** (2003) 42.

[25] A. Shen, H. Ohno, F. Matsukura, Y. Sugawara, N. Akiba, T. Kuroiwa, A. Oiwa, A. Endo, S. Katsumoto, Y. Iye, J. Cryst. Growth **175-176** (1997) 1069.

[26] S. Das Sarma, E.H. Hwang, A. Kaminski, Solid State Commun. **127** (2003) 99.

[27] S.J. Potashnik, K.C. Ku, S.H. Chun, J.J. Berry, N. Samarth, P. Schiffer, Appl. Phys. Lett. **79** (2001) 1495.

[28] K.M. Yu, W. Walukiewicz, T. Wojtowicz, I. Kuryliszyn, X. Liu, Y. Sasaki, J.K. Furdyna, Phys. Rev. B **65** (2002) 201303.

[29] K.W. Edmonds, P. Boguslawski, K.Y. Wang, R.P. Campion, S.N. Novikov, N.R.S. Farley, B.L. Gallagher, C.T. Foxon, M. Sawicki, T. Dietl, M.B. Nardelli, J. Bernholc, Phys. Rev. Lett. **92** (2004) 037201.
[30] C.P. Bean, D.S. Rodbell, Phy. Rev. **126** (1962) 104.
[31] D.J. Boeck, R. Oesterholt, A. Van Esch, H. Bender, C. Bruynseraede, C. Van Hoof, G. Borghs, Appl. Phys. Lett. **68** (1996) 2744.
[32] M. Moreno, B. Jenichen, L. Daweritz, K.H. Ploog, Appl. Phys. Lett. **86** (2005) 161903.
[33] M. Moreno, A. Trampert, L. Däweritz, K.H. Ploog, Appl. Surf. Sci. **234** (2004) 16.
[34] F. Schippan, A. Trampert, L. Daweritz, K.H. Ploog, J. Vac. Sci Technol. B **17** (1999) 1716.
[35] M. Tanaka, J. Cryst. Growth **201-202** (1999) 660.
[36] M. Tanaka, Semicond. Sci. Technol. **17** (2002) 327.
[37] M. Tanaka, J.P. Harbison, M.C. Park, Y.S. Park, T. Shin, G.M. Rothberg, Appl. Phys. Lett. **65** (1994) 1964.
[38] D.B. Holt, J Mater Sci **23** (1988) 1131.
[39] S.J. Pearton, F. Ren, A.P. Zhang, K.P. Lee, Mat. Sci. Eng. R **30** (2000) 55.
[40] T. Miyajima, T. Tojyo, T. Asano, K. Yanashima, S. Kijima, T. Hino, M. Takeya, S. Uchida, S. Tomiya, K. Funato, T. Asatsuma, T. Kobayashi, M. Ikeda, J. Phys.: Condens. Matter. **13** (2001) 7099.
[41] M.E. Levinshtein, S.L. Rumyantsev, M.S. Shur, Properties of advanced semiconductor materials (GaN, AlN, InN, BN, SiC, SiGe), John Wiley & Sons, Inc., 2001.
[42] CRC handbook of chemistry and physics, 84th Edition, 2003-2004, 2003.
[43] G. Popovici, H. Morkoc, *Growth and doping of defects in III-nitrides*, in *GaN and related materials II*, S. Pearton, Editor. 2000, Gordon and Breach Science Publishers. p. 93.
[44] S. Strite, H. Morkoç, J. Vac. Sci. Technol. B **10** (1992) 1237.
[45] L. Liu, J.H. Edgar, Mat. Sci. Eng. R **37** (2002) 61.
[46] J.W. Orton, C.T. Foxon, Rep. Prog. Phys. **61** (1998) 1.
[47] A. Kikuchi, H. Hoshi, K. Kishino, Jpn. J. Appl. Phys. **33** (1994) 688.
[48] H. Okumura, S. Misawa, S. Yoshida, Appl. Phys. Lett. **59** (1991) 1058.
[49] O. Brandt, H. Yang, B. Jenichen, Y. Suzuki, L. Däweritz, K.H. Ploog, Phys. Rev. B **52** (1995) R2253.
[50] T.S. Cheng, L.C. Jenkins, S.E. Hooper, C.T. Foxon, J.W. Orton, D.E. Lacklison, Appl. Phys. Lett. **66** (1995) 1509.
[51] M. Giehler, M. Ramsteiner, O. Brandt, H. Yang, K.H. Ploog, Appl. Phys. Lett. **67** (1995) 733.
[52] S. Ruvimov, Z. Liliental-Weber, J. Washburn, T.J. Drummond, M. Hafich, S.R. Lee, Appl. Phys. Lett. **71** (1997) 2931.
[53] D. Schikora, M. Hankeln, D.J. As, K. Lischka, T. Litz, A. Waag, T. Buhrow, F. Henneberger, Phys. Rev. B **54** (1996) R8381.
[54] H. Yang, O. Brandt, M. Wassermeier, J. Behrend, H.P. Schonherr, K.H. Ploog, Appl. Phys. Lett. **68** (1996) 244.
[55] G. Feuillet, H. Hamaguchi, K. Ohta, P. Hacke, H. Okumura, S. Yoshida, Appl. Phys. Lett. **70** (1997) 1025.
[56] J. Neugebauer, T. Zywietz, M. Scheffler, J.E. Northrup, C.G. Walle, Phys. Rev. Lett. **80** (1998) 3097.
[57] T. Zywietz, J. Neugebauer, M. Scheffler, Appl. Phys. Lett. **73** (1998) 487.
[58] E.J. Tarsa, B. Heying, X.H. Wu, P. Fini, S.P. DenBaars, J.S. Speck, J. Appl. Phys. **82** (1997) 5472.
[59] S. Guha, N.A. Bojarczuk, D.W. Kisker, Appl. Phys. Lett. **69** (1996) 2879.
[60] T.E. Jenkins, *Semiconductor science*. 1994: Prentice Hall.
[61] A. Trampert, O. Brandt, H. Yang, K.H. Ploog, Appl. Phys. Lett. **70** (1997) 583.
[62] H. Yang, O. Brandt, A. Trampert, K.H. Ploog, Appl. Surf. Sci. **104-105** (1996) 461.
[63] D.M. Tricker, P.D. Brown, T.S. Cheng, C.T. Foxon, C.J. Humphreys, Appl. Surf. Sci. **123-124** (1998) 22.

[64] S. Strite, J. Ruan, Z. Li, A. Salvador, H. Chen, D.J. Smith, W.J. Choyke, H. Morkoc, J. Vac Sci. Technol. B **9** (1991) 1924.
[65] D. Chandrasekhar, D.J. Smith, S. Strite, M.E. Lin, H. Morkoc, J. Cryst. Growth **152** (1995) 135.
[66] B. Qu, X.H. Zheng, Y.T. Wang, Z.H. Feng, S.A. Liu, S.M. Lin, H. Yang, J.W. Liang, Thin Solid Films **392** (2001) 29.
[67] Z.X. Qin, H. Nagano, Y. Sugure, A.W. Jia, M. Kobayashi, Y. Kato, A. Yoshikawa, K. Takahashi, J. Cryst. Growth **189-190** (1998) 425.
[68] K. Balakrishnan, G. Feuillet, K. Ohta, H. Hamaguchi, H. Okumura, S. Yoshida, Jpn. J. Appl. Phys. **36** (1997) 6221.
[69] M.B. Haider, C. Constantin, H. Al-Brithen, H. Yang, E. Trifan, D. Ingram, A.R. Smith, C.V. Kelly, Y. Ijiri, J. Appl. Phys. **93** (2003) 5274.
[70] J.Y. Chang, G.H. Kim, J.M. Lee, S.H. Han, H.J. Kim, W.Y. Lee, M.H. Ham, K.S. Huh, J.M. Myoung, J. Appl. Phys. **93** (2003) 7858.
[71] G. Thaler, R. Frazier, B. Gila, J. Stapleton, M. Davidson, C.R. Abernathy, S.J. Pearton, C. Segre, Appl. Phys. Lett. **84** (2004) 2578.
[72] S. Kuroda, E. Bellet-Amalric, R. Giraud, S. Marcet, J. Cibert, H. Mariette, Appl. Phys. Lett. **83** (2003) 4580.
[73] T. Kondo, S. Kuwabara, H. Owa, H. Munekata, J. Cryst. Growth **237-239** (2002) 1353.
[74] Y. Cui, L. Li, Appl. Phys. Lett. **80** (2002) 4139.
[75] M. Hashimoto, Y.K. Zhou, H. Tampo, M. Kanamura, H. Asahi, J. Cryst. Growth **252** (2003) 499.
[76] S. Dhar, O. Brandt, A. Trampert, L. Daweritz, K.J. Friedland, K.H. Ploog, J. Keller, B. Beschoten, G. Guntherodt, Appl. Phys. Lett. **82** (2003) 2077.
[77] K.J. Lee, F.C. Yu, J.A. Kim, D.J. Kim, B.G. Kim, Y.H. Kang, H.J. Kim, Y. E. Ihm, Phys. Stat. Sol. B **241** (2004) 1525.
[78] K.H. Kim, K.J. Lee, H.S. Kang, F.C. Yu, J.A. Kim, D.J. Kim, K.H. Baik, S.H. Yoo, C.G. Kim, Y.S. Kim, C.S. Kim, H.J. Kim, Y. E. Ihm, Phys. Stat. Sol. B **241** (2004) 1458.
[79] K.H. Kim, K.J. Lee, J.B. Park, D.J. Kim, H. Kim, Y.E. Ihm, C.S. Kim, H.C. Lee, C.G. Kim, S.H. Yoo, D. Djayaprawira, M. Takahashi, J. Korean Phys. Soc. **42** (2003) S399.
[80] M.H. Kane, A. Asghar, A.M. Payne, C.R. Vestal, Z.J. Zhang, M. Strassburg, J. Senawirante, N. Dietz, C.J. Summers, I.T. Ferguson, Phys. Stat. Sol. C **2** (2005) 2441.
[81] J.M. Baik, H.S. Kim, C.G. Park, J.-L. Lee, Appl. Phys. Lett. **83** (2003) 2632.
[82] M.L. Reed, M.K. Ritums, H.H. Stadelmaier, M.J. Reed, C.A. Parker, S.M. Bedair, N.A. El-Masry, Mater. Lett. **51** (2001) 500.
[83] M.L. Reed, N.A. El-Masry, H.H. Stadelmaier, M.K. Ritums, M.J. Reed, C.A. Parker, J.C. Roberts, S.M. Bedair, Appl. Phys. Lett. **79** (2001) 3473.
[84] K. Sardar, A.R. Raju, B. Bansal, V. Venkataraman, C.N.R. Rao, Solid State Commun. **125** (2003) 55.
[85] M. Zajac, R. Doradzinski, J. Gosk, J. Szczytko, M. Lefeld-Sosnowska, M. Kaminska, A. Twardowski, M. Palczewska, E. Grzanka, W. Gebicki, Appl. Phys. Lett. **78** (2001) 1276.
[86] R. Dwilinski, R. Doradzinski, J. Garczynski, L. Sierzputowski, J.M. Baranowski, M. Kaminska, Diam. Relat. Mater. **7** (1998) 1348.
[87] S. Sonoda, S. Shimizu, T. Sasaki, Y. Yamamoto, H. Hori, J. Cryst. Growth **237-239** (2002) 1358.
[88] M.H. Kane, A. Asghar, C.R. Vestal, M. Strassburg, J. Senawiratne, Z.J. Zhang, N. Dietz, C.J. Summers, I.T. Ferguson, Semicond. Sci. Technol. **20** (2005) L5.
[89] M.J. Reed, F.E. Arkun, E.A. Berkman, N.A. Elmasry, J. Zavada, M.O. Luen, M.L. Reed, S.M. Bedair, Appl. Phys. Lett. **86** (2005) 102504.
[90] S. Dhar, O. Brandt, A. Trampert, K.J. Friedland, Y.J. Sun, K.H. Ploog, Phys. Rev. B **67** (2003) 165205.

[91] M.B. Haider, C. Constantin, H. Al-Brithen, G. Caruntu, C.J. O'Connor, Arthur R. Smith, Phys. Stat. Sol. A **202** (2005) 1135.
[92] M.H. Ham, M.C. Jeong, W.Y. Lee, J.M. Myoung, J.Y. Chang, S.H. Han, Jpn. J. Appl. Phys. **42** (2003) L1372.
[93] M.H. Ham, M.C. Jeong, W.Y. Lee, J.M. Myoung, J.M. Lee, J.Y. Chang, S.H. Han, J. Electron. Mater. **33** (2004) 114.
[94] K.S. Huh, M.H. Ham, J.M. Myoung, J.M. Lee, K.I. Lee, J.Y. Chang, S.H. Han, H.J. Kim, W.Y. Lee, Jpn. J. Appl. Phys. **41** (2002) L1069.
[95] S. Kuroda, E. Bellet-Amalric, X. Biquard, J. Cibert, R. Giraud, S. Marcet, H. Mariette, Phys. Stat. Sol. B **240** (2003) 443.
[96] Y.L. Soo, G. Kioseoglou, S. Kim, S. Huang, Y.H. Kao, S. Kuwabara, S. Owa, T. Kondo, H. Munekata, Appl. Phys. Lett. **79** (2001) 3926.
[97] P.P. Chen, H. Makino, J.J. Kim, T. Yao, J. Cryst. Growth **251** (2003) 331.
[98] M.E. Overberg, G. Thaler, C.R. Abernathy, N.A. Theodoropoulou, K.T. McCarthy, S.B. Arnason, J.M. Lee, J.D. Lim, S.B. Shim, K.S. Suh, Z.G. Khim, Y.D. Park, S.J. Pearton, A.F. Hebard, J. Electron. Mater. **32** (2003) 298.
[99] J. Neugebauer, T. Zywietz, M. Scheffler, J. Northrup, Appl. Surf. Sci. **159-160** (2000) 355.
[100] C.C. Muhammad B. Haider, Hamad Al-Brithen, Gabriel Caruntu, Charles J. O'Connor, Arthur R. Smith,, Phys. Stat. Sol. A **202** (2005) 1135.
[101] O. Ambacher, J. Phys. D: Appl. Phys. **31** (1998) 2653.
[102] J. Yang, N. Chen, Z. Liu, S. Yang, C. Chai, M. Liao, H. He, J. Cryst. Growth **234** (2002) 359.
[103] M. Tanaka, J.P. Harbison, J. DeBoeck, T. Sands, B. Philips, T.L. Cheeks, V.G. Keramidas, Appl. Phys. Lett. **62** (1993) 1565.
[104] M. Gouné, A. Redjaïmia, T. Belmonte, H. Michel, J. Appl. Cryst. **36** (2003) 103.
[105] A. Leineweber, R. Niewab, H. Jacobs, W. Kockelmannc, J. Mater. Chem. **10** (2000) 2827.
[106] A. Janotti, S.-H. Wei, L. Bellaiche, Appl. Phys. Lett. **82** (2003) 766.
[107] B.R. Sahu, L. Kleinman, Phys. Rev. B **68** (2003) 113101.
[108] H. Yang, H. Al-Brithen, E. Trifan, D.C. Ingram, A.R. Smith, J. Appl. Phys. **91** (2002) 1053.
[109] R. Giraud, S. Kuroda, S. Marcet, E. Bellet-Amalric, X. Biquard, B. Barbara, D. Fruchart, D. Ferrand, J. Cibert, H. Mariette, Europhys. Lett. **65** (2004) 553.
[110] X. Biquard, O. Proux, J. Cibert, D. Ferrand, H. Mariette, R. Giraud, B. Barbara, J. Supercond. **16** (2003) 127.
[111] G. Martinez-Criado, A. Somogyi, A. Homs, R. Tucoulou, J. Susini, Appl. Phys. Lett. **87** (2005) 061913.
[112] J.J. Rehr, J.M.d. Leon, S.I. Zabinsky, R.C. Albers, J. Am. Chem. Soc. **113** (1991) 5135
[113] S.K. Nayak, P. Jena, Chem. Phys. Lett. **289** (1998) 473.
[114] B.K. Rao, P. Jena, Phys. Rev. Lett. **89** (2002) 185504.
[115] J. Schliemann, Phys. Rev. B **67** (2003) 045202.
[116] V.K. Dugaev, V.I. Litvinov, J. Barnas, M. Vieira, Phys. Rev. B **67** (2003) 033201.
[117] M.v. Schilfgaarde, O.N. Mryasov, Phys. Rev. B **63** (2001) 233205.
[118] M.B. Kanoun, S. Goumri-Said, A.E. Merad, J. Cibert, J. Phys. D: Appl. Phys. **38** (2005) 1853.
[119] F. Glas, G. Patriarche, L. Largeau, A. Lemaitre, Phys. Rev. Lett. **93** (2004) 086107.
[120] D.J. As, D. Schikora, K. Lischka, Phys. Stat. Sol. C **0** (2003) 1607.
[121] H. Morkoç, *Nitride semiconductors and devices*. 1999, Berlin: Springer.
[122] B.D. Cullity, S.R. Stock, *Elements of X-ray Diffraction*. 2001, New Jersey: Prentice Hall.
[123] C. Hammond, *The basics of crystallography and diffraction*. 2 ed. 2001: Oxford Press.
[124] P.E. Champness, *Electron diffraction in the transmission electron microscope*. 2001, Oxford: BIOD Scientific Publishers Ltd.

[125] D.B. Williams, C.B. Carter, *Transmission electron microscopy - a textbook for materials science*. 1996: Plenum Press.
[126] R. Brydson, *Electron energy loss spectroscopy*. 2001: BIOS Scientific Publishers Limited.
[127] P.J. Goodhew, J. humphreys, R. Beanland, *Electron microscopy and analysis*, ed. T. edition. 2000, New York: Taylor & Francis.
[128] J. Taftø, J.C.H. Spence, J. Appl. Cryst. **15** (1982) 60.
[129] B.C. De Cooman, C.B. Carter, Appl. Phys. Lett. **50** (1987) 40.
[130] P.D. Brown, K. Durose, G.J. Russell, J. Woods, J. Cryst. Growth **101** (1990) 211.
[131] K. Ishizuka, J. Taftø, Acta Cryst. **B40** (1984) 332.
[132] J.H. Neave, B.A. Joyce, J. Cryst. Growth **44** (1978) 387.
[133] J.J. Friel, N.C. Barbi, *X-ray microanalysis and computer-aided imaging*: PGT.
[134] I.P. Jones, *Chemical microanalysis using electron beams*. 1992, London: Institute of Materials.
[135] J.M. Cowley, *Diffraction physics*. 3 ed. 1995, Amsterdam: Elsevier.
[136] H. Tsuchiya, T. Okahisa, F. Hasegawa, H. Okumura, S. Yoshida, Jpn. J. Appl. Phys. **33** (1994) 1747.
[137] Y. Han, M.W. Fay, P.D. Brown, S.V. Novikov, K.W. Edmonds, B.L. Gallagher, R.P. Campion, C.R. Staddon, C.T. Foxon, J. Cryst. Growth **284** (2005) 324.
[138] J.M. Cowley, Electron Diffraction Techniques, Electron Diffraction: An Introduction, Oxford University Press, Oxford, 1992.
[139] C.T. Foxon, S.V. Novikov, L.X. Zhao, K.W. Edmonds, A.D. Giddings, K.Y. Wang, R.P. Campion, C.R. Staddon, M.W. Fay, Y. Han, P.D. Brown, M. Sawicki, B.L. Gallagher, J. Cryst. Growth **278** (2005) 685.
[140] S.V. Novikov, K.W. Edmonds, L.X. Zhao, A.D. Giddings, K.Y. Wang, R.P. Campion, C.R. Staddon, M.W. Fay, Y. Han, P.D. Brown, M. Savicki, B.L. Gallagher, C.T. Foxon, J. Vac. Sci. Technol. B **23** (2005) 1294.
[141] H. Nakayama, H. Mashita, E. Kulatov, R. Funahashi, H. Ohta, J. Magn. Magn. Mater. **258-259** (2003) 323.
[142] Y. Seki, H. Wantanabe, J. Matsui, J. Appl. Phys. **49** (1978) 822.
[143] H.A.H. AL-Brithen, E.M. Trifan, D.C. Ingram, A.R. Smith, D. Gall, J. Cryst. Growth **242** (2002) 345.
[144] T. Hayashi, M. Tanaka, T. Nishinaga, H. Shimada, H. Tsuchiya, Y. Otuka, J. Cryst. Growth **175-176** (1997) 1063.
[145] A.J. Blattner, P.L. Prabhumirashi, V.P. Dravid, B.W. Wessels, J. Cryst. Growth **259** (2003) 8.
[146] S. Guha, H. Munekata, J. Appl. Phys. **74** (1993) 2974.
[147] Alloy phase diagrams, ASM handbook, ASM International Alloy Phase Diagram & Handbook Committees, Ohio, 1992.
[148] M.W. Fay, Y. Han, P.D. Brown, S.V. Novikov, K.W. Edmonds, R.P. Campion, B.L. Gallagher, C.T. Foxon, Appl. Phys. Lett. **87** (2005) 031902.
[149] M.W. Fay, Y. Han, S.V. Novikov, K.W. Edmonds, K. Wang, B.L. Gallagher, R.P. Campion, C.T. Foxon, P.D. Brown, *Structural characterisation of spintronic GaMnAs and GaMnN heterostructures grown by molecular beam epitaxy*, Microscopy of Semiconducting Materials IX, Oxford (2005), Springer Proceedings in Physics **107** 143
[150] W.R.L. Lambrecht, M. Prikhodko, M.S. Miao, Phys. Rev. B **68** (2003) 174411.
[151] S.J. Pearton, Y.D. Park, C.R. Abernathy, M.E. Overberg, G.T. Thaler, J. Kim, F. Ren, J. Electron. Mater. **32** (2003) 288.
[152] K.-S. Huh, M.-C. Jeong, M.-H. Ham, J.-M. Myoung, W.-Y. Lee, J.-M. Lee, S.-H. Han, Solid State Commun. **128** (2003) 119.
[153] B. He, X. Zhang, S. Wei, H. Oyanagi, S.V. Novikov, K.W. Edmonds, C.T. Foxon, G.e. Zhou, Y. Jia, Appl. Phys. Lett. **88** (2006) 051905.